Probing Chromospheric Magnetic Field Through Multi-Line Spectropolarimetry

A Thesis
Submitted for the Degree of
Doctor of Philosophy (Technology)

Submitted by
HARSH MATHUR

Department of Applied Optics & Photonics
University of Calcutta
2024

Dedicated to my dad, who instilled curiosity in me to pursue a career in science, and to my mom, who imparted the invaluable lesson of perseverance.

"There is a theory which states that if ever anyone discovers exactly what the Universe is for and why it is here, it will instantly disappear and be replaced by something even more bizarre and inexplicable. There is another theory which states that this has already happened." — Douglas Adams, The Restaurant at the End of the Universe

Abstract

The chromosphere, situated between the bright photosphere and the remarkably thin transition region that precedes the million-degrees hot corona, is a highly dynamic and intricate layer within the solar atmosphere. By unraveling the magnetic coupling between the chromosphere, photosphere, transition region, and corona, we may gain valuable insights into the mechanisms through which mass and energy are transferred to the corona as well as the generation of the solar wind that expands outward into the surrounding regions of the solar atmosphere. Hence, it is crucial to carry out simultaneous magnetic field measurements at various heights within the solar atmosphere. In this context, multiline spectropolarimetry is a powerful observational technique, allowing for simultaneous inference of magnetic fields at various heights in the solar atmosphere.

The most widely used lines to probe the magnetic field of the solar chromosphere are the Ca II 8542 Å and He I 10830 Å lines. However, these lines have their limitations. The formation of the He I 10830 Å line occurs within a limited range of heights in the upper chromosphere, and its formation relies on incoming EUV radiation from the coronal and transition region. In contrast, the Ca II 8542 Å line forms from the upper photosphere to the mid-chromosphere. However, in flaring active regions, the Ca II ion gets ionized to the Ca III ion, potentially causing the Ca II 8542 Å line to sample deeper layers of the solar atmosphere.

The Hα line could be an excellent chromospheric diagnostic. Using 3D radiative transfer modeling, theoretical investigations about the formation of the Hα line intensity profiles have shown that the line core images of the Hα line trace chromospheric magnetic features, and the line also retains opacity during heating events such as flares. However, the diagnostic potential of the Hα line to probe the chromospheric magnetic field from the polarization profiles of the Hα line has been investigated, neither theoretically nor observationally.

This thesis addresses this challenge through spectropolarimetric observations of the Hα line recorded simultaneously with other widely used chromospheric spectral lines, such as the Ca II IR triplet. In our first project, we utilized spectropolarimetric observations of a small pore recorded simultaneously in the Hα and Ca II 8542 Å lines from the Dunn Solar Telescope SPINOR instrument. We inferred the stratification of the line-of-sight magnetic field from the non-LTE inversions of the Ca II 8542 Å line and compared it with that inferred from the weak field approximation over the Hα line. The results of this study supported the conclusion that the Hα line probes the chromospheric magnetic field.

To carry out further simultaneous multiline spectropolarimetric observations, we have upgraded the Kodaikanal Tower Tunnel Telescope to record three spectral lines simultaneously. Additionally, we discuss the development and installation of an image stabilization system, incorporating a tip-tilt and autoguider system, designed to reduce seeing-induced cross-talk of the polarimetric signal. Our findings demonstrate the tip-tilt system operates with a cut-off frequency of 80 Hz and reduces the seeing-induced cross-talk in the polarization measurements at least by a factor of 2.

We used this enhanced setup to conduct simultaneous spectropolarimetric scans in the Hα and Ca II 8662 Å lines. We analyzed the stratification of the magnetic field inferred from a large sunspot, NOAA 13315, observed on 27th May 2023. We concluded that the line core of the Hα line consistently probes the chromospheric magnetic field at higher heights than that probed by the Ca II IR triplet lines, and in case of localized heating events, the full spectral range of the Hα line becomes sensitive to the chromospheric magnetic field instead of just the line core.

Contents

List of Publications

Refereed Journal Articles (related to this thesis)

1. *Do Hα Stokes V profiles probe the chromospheric magnetic field? An observational perspective*
   Harsh Mathur, K. Nagaraju, Jayant Joshi, and Jaime de la Cruz Rodríguez, March 2023, **The Astrophysical Journal**, Volume 946, Issue 1, id.38, 14 pp.

2. *An Image Auto Guider System for Kodaikanal Tower Tunnel Telescope*
   Harsh Mathur, K.C. Thulasidharen, Hemanth Pruthvi, K. Nagaraju, and M. Rajalingam, 2022, **Journal of Astronomical Instrumentation**, Volume 11, Issue 4, id. 2350003.

3. *Measurements of seeing-induced crosstalk in tip-tilt corrected solar polarimetry*
   Harsh Mathur, K. Nagaraju, Hemanth Pruthvi, and K. Sagaynathan, 2024, **Applied Optics**, 63, 4088-4094 (2024).

4. *Simultaneous spectropolarimetric observations in the Hα and* Ca II *8662 Å lines of an active region*
   Harsh Mathur, K. Nagaraju, Rahul Yadav, and Jayant Joshi, 2024, **The Astrophysical Journal**, accepted, June. 2024.

Refereed Journal Articles (not related to this thesis)

1. *Properties of shock waves in the quiet-Sun chromosphere*
   Harsh Mathur, Jayant Joshi, K. Nagaraju, Luc Rouppe van der Voort, Souvik Bose, December 2022, **Astronomy & Astrophysics**, Volume 668, id.A153, 21 pp.

2. *Solar mean magnetic field of the chromosphere*
   M. Vishnu, K. Nagaraju, and **Harsh Mathur**, December 2023, **Journal of Astrophysics and Astronomy**, Volume 44, Issue 2, article id.56.

Conference Presentations (Talks)

1. *Do Hα Stokes V profiles probe the chromospheric magnetic field? An observational perspective*
   Harsh Mathur, K. Nagaraju, Jayant Joshi, and Jaime de la Cruz Rodríguez, November 7-11, 2022, **Solar Polarization Workshop - 10**, Kyoto University, Kyoto, Japan

Posters

1. *Properties of shock waves in the quiet-Sun chromosphere* at Confronting numerical models of the solar chromosphere and corona with high-resolution observations - a RoCS/MUSE/IRIS workshop from 27th Feb to 2nd March 2023.
2. *Simultaneous spectropolarimetric observations in the Hα and* Ca II *8662 Å lines of an active region* - IIA in-house symposium from 26th March to 28th March 2024.
3. *Properties of shock waves in the quiet-Sun chromosphere* - IIA in-house symposium from 30th March to 31st March 2023.

List of Figures

List of Tables

Chapter 1
Introduction

> *"Things didn't go exactly as planned, but I'm not dead, so it's a win."* — Andy Weir, The Martian

The Sun, a G2V-type main-sequence star, plays a central role in sustaining life on Earth by providing essential light and energy. Boasting a mass of approximately 1.989 x 10^{30} kilograms, it commands over 99% of the total mass in our solar system, governing the orbits of planets and celestial bodies through its gravitational force. Emitting radiation that leads to a flux of about 1 kW per square meter as received at Earth, the Sun serves as the primary source of light and heat, enabling and driving the intricate climate dynamics within our planetary system. Its proximity, at just 149.6 million kilometers away, distinguishes it from other stars in our galaxy, allowing for comprehensive studies in unprecedented detail.

The Sun's magnetic field, which extends its influence into the space weather around Earth, adds to its intrigue. Notably, it plays a crucial role in phenomena such as the propulsion of the solar wind, a continuous stream of charged particles that shapes the heliosphere, our solar system's protective barrier against interstellar radiation. This magnetic field is also pivotal in facilitating the transfer of mass and energy to the Sun's corona, the outermost layer of its atmosphere, where temperatures rise to several million degrees, defying the laws of thermodynamics. Understanding the transfer of energy from the lower solar atmospheric layers to higher ones is a significant puzzle with far-reaching implications for our comprehension of the entire solar system. Solar flares, explosive releases of radiation, and charged particles from the Sun are another captivating phenomenon closely tied to the Sun's magnetic field. It acts as a conductor, directing the swift movement of charged particles during these dramatic solar outbursts. Unraveling this mechanism is not only scientifically intriguing but also of practical importance, as these charged particles can potentially impact astronaut safety, satellite integrity, and terrestrial power grids. One of the most immediate and tangible consequences of this magnetic influence is seen in space weather. The magnetic field is closely connected to Coronal Mass Ejections (CMEs), massive bursts of magnetic fields, and accompanying plasma mass from the Sun's corona into the heliosphere. Space weather encompasses the conditions on the Sun, in the solar wind, CMEs, magnetosphere, and ionosphere which can affect the performance of space-based and ground-based technology systems and pose risks to human life and health. The significance of studying and continuously monitoring the Sun, its atmosphere, and the transfer of energy from the solar interior to its outer atmospheric layers becomes evident when considering the potential consequences mentioned earlier. These consequences encompass the Sun's magnetic field's influence on space weather and how it affects technology systems both in space and on the ground, along with the potential risks to human life and health. In the following sections, we offer a concise overview of the various layers within the solar atmosphere, spanning from the solar interior to the corona while also delving into the various magnetic structures observed in the surface layers. We place particular emphasis on the magnetic interplay between these different atmospheric layers highlighting the significance of the chromospheric magnetism. Additionally, we delve into mechanisms such as the Zeeman and Hanle effects, through which the magnetic field gets imprinted on the polarization of the radiation coming from the Sun. We also explore the various methods employed to infer vector magnetic fields. Furthermore, this discussion includes an overview of the instrumentation used to measure polarization profiles by modulating the input intensity of sunlight in relation to the input polarization signals.

1.1 The Solar Structure

1.1.1 The Solar Interior

The solar interior consists of three zones, namely, the core, radiative, and convection zones, based on the physical processes dominant within them. These cannot be directly observed, only the surface layers of the Sun can be seen directly. Deep within the core, hydrogen undergoes a transformative process, converting into helium via nuclear fusion, primarily through the proton-proton (PP) chain and, to a lesser extent, the carbon-nitrogen-oxygen (CNO) cycle (Priest, 2014). This fusion process generates an immense amount of energy, which slowly seeps outward into both the radiative and convection zones. Spanning the region between 0.25 $R_\odot$ and 0.7 $R_\odot$ the radiative zone is incredibly opaque, where photons are continually absorbed and re-emitted as they journey outward. Based on a random walk analysis of a solar model conducted by Mitalas and Sills (1992), it is estimated that it takes nearly 170,000 years for a photon to traverse from the solar interior to its surface. Moving outward through the radiative zone, the temperature experiences a rapid decline, leading to heightened opacity due to the formation of neutral hydrogen and helium. At about 0.7 $R_\odot$, the temperature gradient becomes sufficiently steep, triggering convective instabilities and marking the onset of the convection zone (Priest, 2014). In this region, the opacity increases to a level where the majority of energy is transported through the movement of plasma blobs using the convection process.

1.1.2 The Photosphere

As hot plasma rises from the convection zone, it reaches a region where its opacity is too low to trap radiation effectively. The subsequent loss of radiation reduces internal pressure, causing the plasma to expand. This expansion leads to cooling and restoring convective stability. This layer is known as the "photosphere", named after the Greek word for "light", as it is where a significant portion of the Sun's visible light, around 5000 Å (green), is emitted. However, the photosphere doesn't exhibit uniform brightness; instead, it showcases convective motions in the form of solar granulation. These granules represent the summits of small convective cells, continually forming and vanishing in a turbulent fashion. The center of each granule appears bright because it consists of hot plasma rising at speeds of 0.5 to 1.5 km s^{-1} and horizontally flowing outward. In contrast, the 0.3 Mm-wide boundaries, also known as intergranular lanes, appear dark and contain cooler, descending material (Priest, 2014).

The photosphere's magnetic field displays a wide range of scales and strengths (Wiegelmann, Thalmann, and Solanki, 2014). Areas with strong magnetic fields that accompany sunspots are referred to as "active regions". Sunspots represent regions of reduced surface temperature caused by concentrations of magnetic flux that hinder convection. Typically, sunspots appear in pairs with opposite magnetic polarities, and their numbers fluctuate according to the 11-year solar cycle (Charbonneau, 2020). In contrast, the "quiet Sun" denotes the solar surface areas that lack sunspots and active regions. The quiet Sun displays a mesh-like pattern of strong kilogauss magnetic fields known as the magnetic network, along with numerous smaller-scale flux concentrations in the areas between them, referred to as the solar internetwork (Bellot Rubio and Orozco Suárez, 2019).

1.1.3 The Chromosphere

The term "chromosphere" has its roots in ancient Greek, with "$\chi\rho\omega\mu\alpha$" denoting color and "$\sigma\varphi\alpha\iota\sigma\alpha$" signifying sphere. This term was coined to describe the vibrant, delicate border visible above the lunar limb during a solar eclipse. The dominant hue is primarily the result of radiation around 656 nm, emitted by neutral hydrogen atoms undergoing a transition from energy level $n = 3$ to $n = 2$, corresponding to the Hα spectral line. In essence, the chromosphere can be defined as the Sun's region where Hα radiation originates. When an eclipse is not occurring, one can observe the chromosphere by imaging the Sun with the use of a narrow-band filter centered

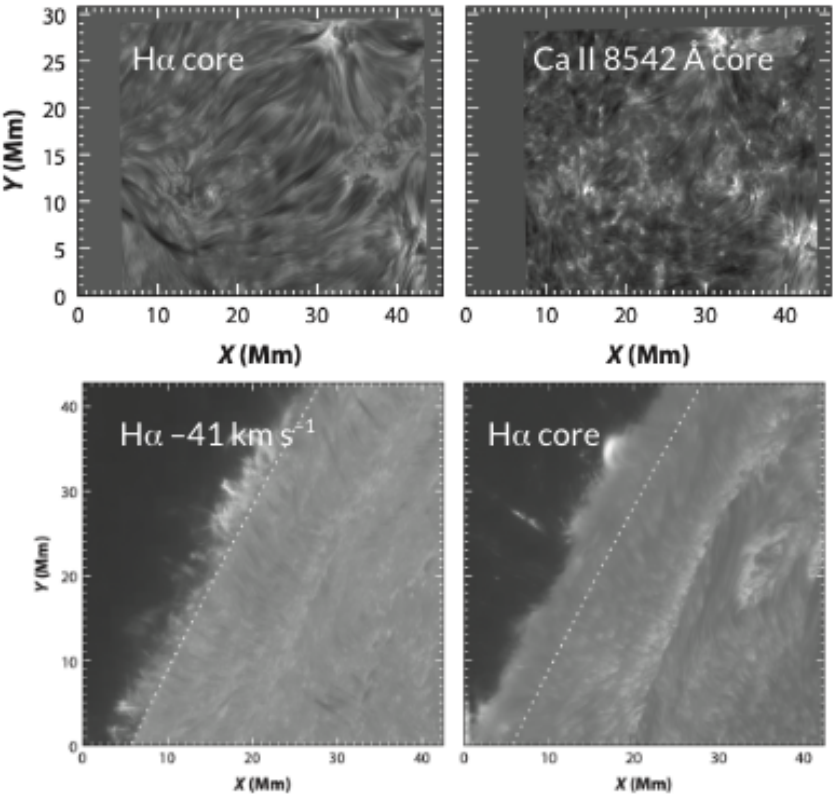

Figure 1.1: Observations from the CHROMIS instrument of the Swedish Solar Telescope. The top teo panels show the narrowband images near the core of the Hα and Ca II 8542 Å line. The bottom two panels show the images of the solar limb at -41 km s^{-1} from the core of the Hα line and at the core of the Hα line. Image credit: Carlsson, De Pontieu, and Hansteen (2019)

on the Hα wavelength (Carlsson, De Pontieu, and Hansteen, 2019). Figure 1.1 shows the chromosphere through the narrowband images of the Hα and Ca II 8542 Å lines. These observations reveal that the chromosphere is not in radiative equilibrium. This is because of the presence of significant opacity in the core of the Hα line which is evident by the extension of the chromospheric plasma up to 5 Mm above the solar limb. The opacity of the Hα line is proportional to the number density of $n = 2$ energy level. If the chromosphere would have been in radiative equilibrium, then the temperature at these higher atmospheric layers would have been about 4000 K. This temperature, owing to the excitation potential of 10 eV of $n = 2$ level, is not sufficient to populate the energy level significantly. In such an atmosphere, we would not see the material above the visual limb in contrast to what is shown in the observations. Historically, semi-empirical models were developed to elucidate observations of spectral lines such as Hα and Ca II 8542 Å as pioneered by Vernazza, Avrett, and Loeser (1981). Figure 1.2 presents the temperature profile of the VAL model, revealing a temperature decrease to a minimum of approximately 4000 K, occurring roughly 500 km above the solar surface. The temperature then experiences a subsequent increase to 8000 K at an altitude of about 2000 km, followed by a rapid rise to the million-degree corona. These models initially assumed the chromospheric atmosphere to be relatively homogeneous, plane-parallel, and static. However, in reality, the chromosphere is significantly non-uniform and dynamic, highly inhomogeneous, time-varying, non-equilibrium plasma in the solar atmosphere (Carlsson, De Pontieu, and Hansteen, 2019; Priest, 2014). In contrast to geometrical definitions, contemporary observational and numerical modeling define the chromosphere based on physics principles. Specifically, the chromosphere is defined as the region situated above the photosphere where radiative equilibrium breaks down, and hydrogen remains predominantly in a neutral state.

Both in active-region plage and in the network, the kilogauss magnetic field structures appear more diffuse in the chromosphere than in the photosphere (Wiegelmann, Thalmann, and Solanki, 2014). Historical studies have found that the plage regions have concentrated vertical fields in the solar photosphere and inclined, canopy, and volume-filling fields in the chromosphere (for eg. Narayan and Scharmer, 2010; Buehler et al., 2015). A sample observation and chromospheric magnetic field inferred in a plage region is shown in Fig. 1.3. These regions often are at the footpoints of coronal loops and serve as a crucial interface for the transfer of non-thermal energy responsible for heating the solar corona (Carlsson, De Pontieu, and Hansteen, 2019). High-resolution observations of the sunspots show sudden brightenings in the blue wing of the Ca II lines, called Umbral Flashes, which are linked to oscillations of the magnetic field due to propagation shock-waves (for eg. de la Cruz Rodríguez et al., 2013; Joshi and de la Cruz Rodríguez, 2018; Felipe et al., 2023). A sample observation and chromospheric magnetic field inferred in a sunspot chromosphere during an

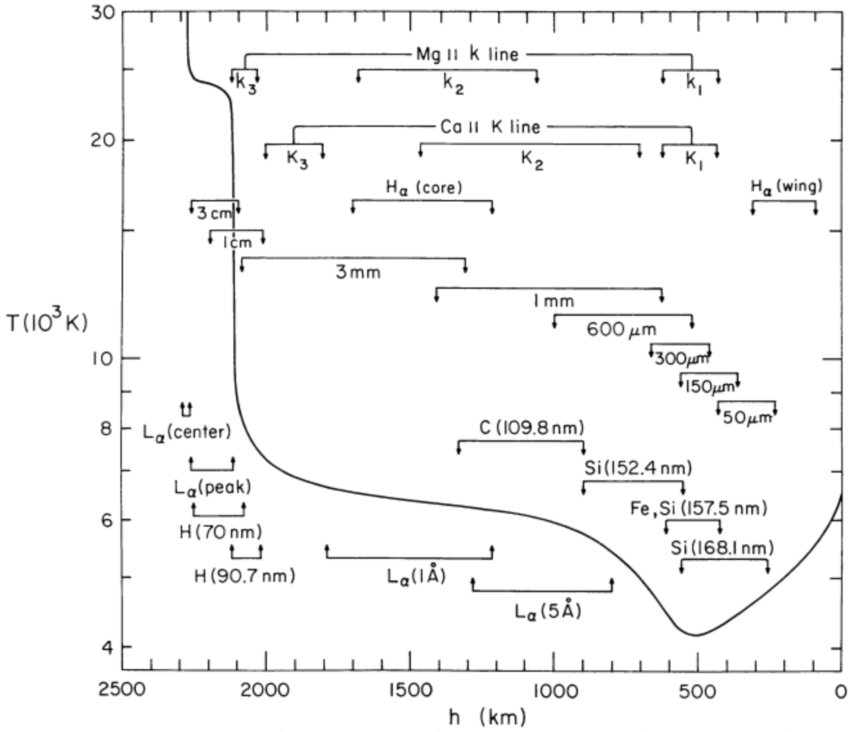

Figure 1.2: Variation of temperature with height in the VAL model. Image credit: Vernazza, Avrett, and Loeser (1981)

Umbral flash region is shown in Fig. 1.4. Sudden brightenings in the blue wing of the Ca II lines are also observed in the internetwork region of the quiet-Sun and are called calcium grains. The magnetic nature of these calcium grains has been refuted in the literature (Carlsson and Stein, 1992, 1997; Beck et al., 2008; Vecchio, Cauzzi, and Reardon, 2009; Mathur et al., 2022b), however, a recent study has reported evidence of magnetic nature of such events, suggesting these to be the same phenomenon as Umbral Flashes (Martínez González et al., 2023). The Hα chromosphere is also replete with ubiquitous small-scaled thread-like structures termed spicules. Spicules are dynamic jets of chromospheric plasma that reach the heights of 10 000 km or above the photosphere (Beckers, 1968, 1972; Sterling, 2000). Historically, they have been observed in off-limb observations as hair-like features protruding outwards from the limb (see Fig. 1.1).

Another interesting object are prominences, which is a plasma suspended in the corona but a hundred times cooler and denser. In eclipse or coronagraph images, they appear bright in emission at the limb, but in Hα images of the disc they show up in absorption as thin, dark, meandering ribbons called filaments. They are located in highly sheared, mainly horizontal, magnetic field above polarity-inversion lines, where the radial photospheric magnetic field component reverses (Priest, 2014).

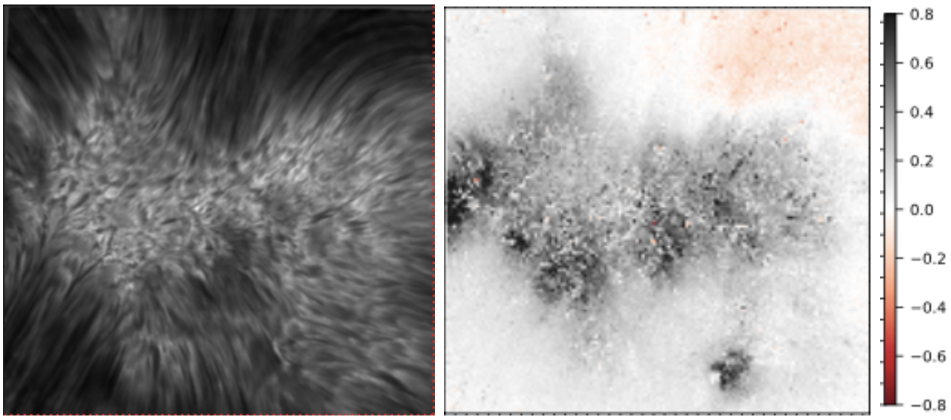

Figure 1.3: An observation of a Plage chromosphere. The left panel shows the intensity at an offset of $\Delta\lambda = 85$ mÅ from the core of the Ca II 8542 Å line. The right panel shows the inferred line-of-sight chromospheric magnetic field in kiloguass units. Image credit: Morosin et al. (2022)

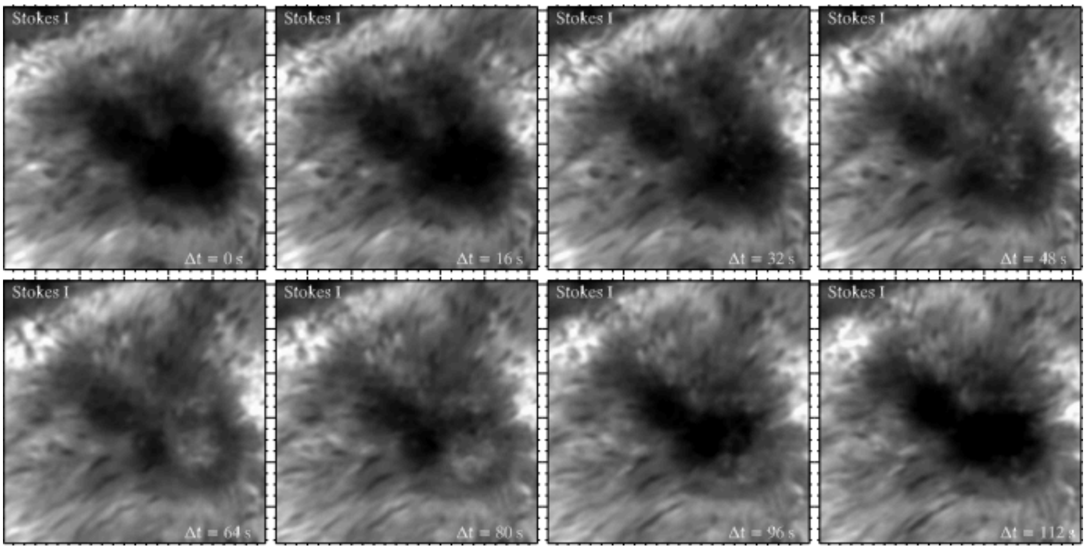

Figure 1.4: An observation of a sunspot chromosphere in the Ca II 8542 Å line with an umbral flash visible from Δt=48-80 s. Image credit: de la Cruz Rodríguez et al. (2013).

1.1.4 The Transition Region

According to the VAL model, at a height of about 2000 km, the temperature increases dramatically from 25000 K to 30000 K coronal temperatures over a relatively thin layer of only 100 km in thickness, which is commonly referred to as the transition region. Similar to the chromosphere, it is not a narrow static horizontal layer but represents all the plasma that happens to be at transition-region temperatures while heating up (in response to coronal heating) or cooling down (either by thermal instability or when the heating is switched off: Priest (2014)). Some of the strongest transitions to probe this layer are lines of ions of heavier atoms such as carbon, oxygen, silicon, and magnesium with ionization states between +1 and +8 forming between temperatures of about $10^{4.9}$-10^5 K which offer excellent diagnostics of plasma dynamics for a large variety of physical mechanisms, including spicules, jets, prominences, flares and UV bursts (De Pontieu et al., 2021). It is often assumed that the transition region spectral lines are formed under optically thin conditions because of steep temperature rise and at least two orders of magnitude decrease in density (Carlsson, De Pontieu, and Hansteen, 2019). However, Kerr et al. (2019) suggest that this might not always be the case, especially during highly energetic events such as flares.

1.1.5 The Corona

The corona (Latin for “crown”) is the topmost layer of the solar atmosphere with temperatures a few times of 10^5 K in open field regimes such as coronal holes (CH), 1-2 MK in closed field regimes in the quiet-Sun corona and up to 2 to 6 MK in the active region corona (chapter 1 of Aschwanden, 2005). The corona was first observed by Chinese and Egyptian astronomers at solar eclipses as a faint halo about as bright as the Moon. Studies in the 1930s found the coronal spectra are due to high ionization states (up to +15) of the known elements, for eg. Fe XV, which implies temperatures as high as 10^6 K. Due to such temperatures, the primary emission of the solar corona is in EUV and soft X-rays (Priest, 2014). Figure 1.5 shows images of the solar corona during an eclipse and a full disk soft X-ray image from the Yohkoh satellite.

The solar corona is characterized by a tripartite structural composition. This includes coronal holes, which are less luminous regions where plasma is expelled outward along open magnetic field lines, contributing to the generation of the fast solar wind. In contrast, the coronal loops, which are more radiant, represent magnetically closed structures that bridge areas of the photosphere with opposing magnetic polarities. Additionally, the corona is interspersed with small, intensely luminous entities known as X-ray bright points. These are dispersed across the entire solar disc and comprise miniature loop configurations (Priest, 2014). Streamers are huge, long-lived, radially oriented structures that extend from the base of the corona out to several solar radii. A subclass are helmet streamers, which are connected with active regions and are centered over prominences (above the limb) or filaments on the disk (chapter 1 of Aschwanden (2005)).

1.2 Magnetic coupling and importance of chromosphere

The solar atmosphere is composed of various layers that are interconnected through magnetic fields. The quiet Sun's atmosphere is primarily structured around magnetic network patches, which demarcate the boundaries of supergranulation cells. These large-scale convective currents transport magnetic fields to supergranular lanes, visually forming the magnetic network. Advanced high-resolution observations have revealed that these network patches are, in fact, clusters of smaller magnetic elements (Wiegelmann, Thalmann, and Solanki, 2014; Wedemeyer-Böhm, Lagg, and Nordlund, 2009, and references therein.). This structure is illustrated in Fig. 1.6, where long thick arrows represent the magnetic network. Sunspots, on the other hand, emerge when magnetic fields intensify to the point of suppressing convection. In higher atmospheric layers, these magnetic fields expand and either curve back towards the photosphere or intersect with adjacent flux tubes, forming a "magnetic canopy" — a structure almost parallel to the solar surface, laid over a nearly field-free atmosphere. The altitude at which photospheric flux tubes merge varies, ranging from approximately 100 km in active regions to around 1 Mm in quiet-Sun areas. In plage regions, the merging occurs in the mid to upper photosphere, resulting in a predominantly magnetic upper atmosphere (Narayan and Scharmer, 2010; Buehler et al., 2015). Models suggest that in quiet-Sun regions and coronal holes, where magnetic features are more dispersed, the canopy base lies in the lower chromosphere (Gabriel, 1976; Jones and Giovanelli, 1982; Solanki and Steiner, 1990; Solanki, Steiner, and Uitenbroeck, 1991). Beyond this canopy, the coronal space is uniformly infused with magnetic fields.

The role of magnetic fields in transporting energy and mass to the solar corona is significant (Reale, 2014) and in driving solar wind mechanisms (Cranmer and Winebarger, 2019). Current theories in solar physics bifurcate on this issue. One school of thought proposes that a continuous sequence of magnetic reconnection events at various scales contributes to the heating of the Sun's outer layers, possibly through numerous nanoflares as suggested by Parker (1988) and Priest, Heyvaerts, and Title (2002), or via photospheric movements leading to magnetic field line braiding (Cirtain et al., 2013; Hansteen et al., 2015; Parker, 1972). In contrast, there's an opposing viewpoint that this heating mainly arises from the damping or dissipation of magnetohydrodynamic (MHD) waves (Alfvén, 1947; Van Doorsselaere et al., 2020). Given the solar atmosphere's complex, dynamic nature, it is plausible that multiple heating mechanisms may simultaneously operate in the Sun's upper atmospheres (Parnell and De Moortel, 2012).

The chromosphere is a critical region, acting as a conduit for all the non-thermal

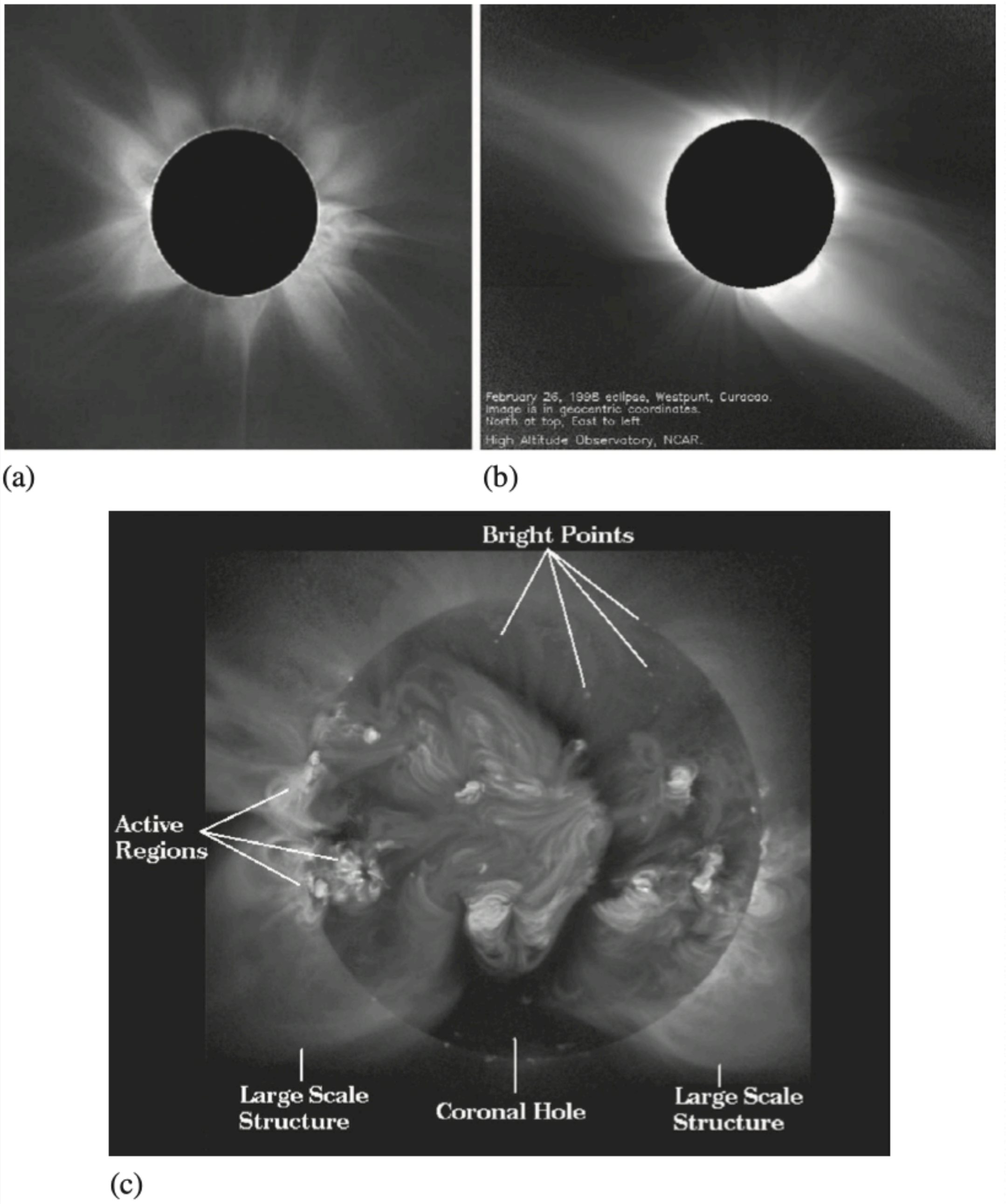

Figure 1.5: Two views of the solar corona: in white light during an eclipse near (a) solar maximum and (b) solar minimum. Panel (c) shows a soft X-ray image of the corona observed from the Yohkoh satellite, showing different coronal features. Image credit: Priest (2014).

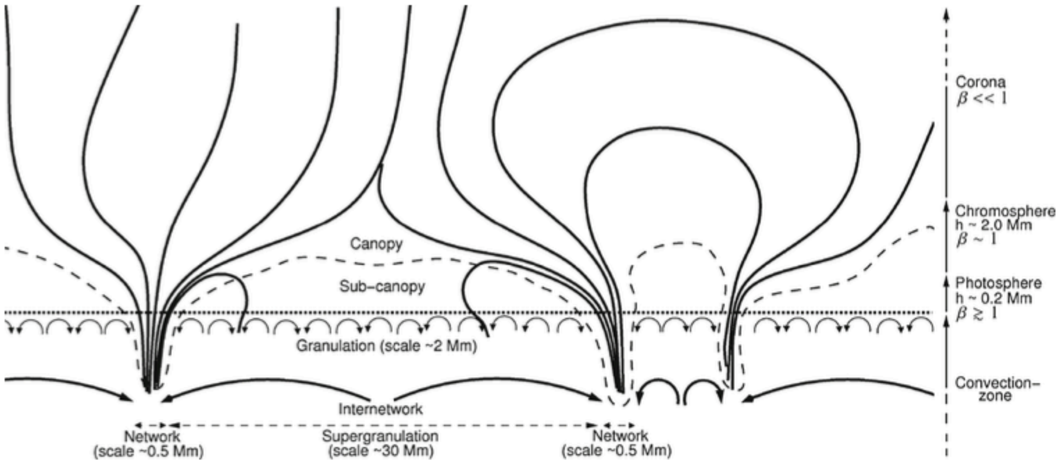

Figure 1.6: Illustration showing the magnetic field topology in the Sun's atmosphere, depicted in a vertical section. Large-scale convective currents (represented by thick, prominent arrows at the lower part) push the magnetic field to the periphery of supergranular cells, leading to the formation of strong magnetic elements or sunspots. Below the dotted line indicating the photosphere, smaller convective movements (indicated by thin, smaller arrows) create the granular pattern on the photosphere. The magnetic field lines (solid lines) widen at the height of the chromosphere, culminating in a nearly horizontal magnetic canopy (depicted as a dashed line). Image credit: Wiegelmann, Thalmann, and Solanki (2014).

energy, propagating from the lower to the higher atmosphere that heats the corona and powers the solar wind. However, a significant portion of this energy remains within the chromosphere itself. Although the chromosphere's temperature is only slightly higher than that of the photosphere, its many scale heights of dense plasma and radiative loss studies suggest that it requires far more nonthermal energy to maintain than the corona (Withbroe and Noyes, 1977; Vernazza, Avrett, and Loeser, 1981) Moreover, the mass present in both the corona and the solar wind originates from the chromosphere (Carlsson, De Pontieu, and Hansteen, 2019). Yet many questions remain about how the chromosphere is heated and how its coupling to the corona supplies mass and energy to the outer atmosphere. The role of the partially ionized chromosphere in processing magnetic flux, which is crucial for flares and eruptions, is not yet fully understood. Thus, comprehending the physical processes within the chromosphere is vital for understanding the mechanisms behind the chromospheric and coronal heating (Carlsson, De Pontieu, and Hansteen, 2019).

1.3 Polarization and Stokes formalism

Astrophysics, unlike many other branches of physics, faces a unique challenge in its reliance on the scientific method: the absence of direct experimentation. Unlike fields where controlled experiments are feasible, astrophysicists are constrained to observe celestial phenomena from vast distances, utilizing sophisticated observational tech-

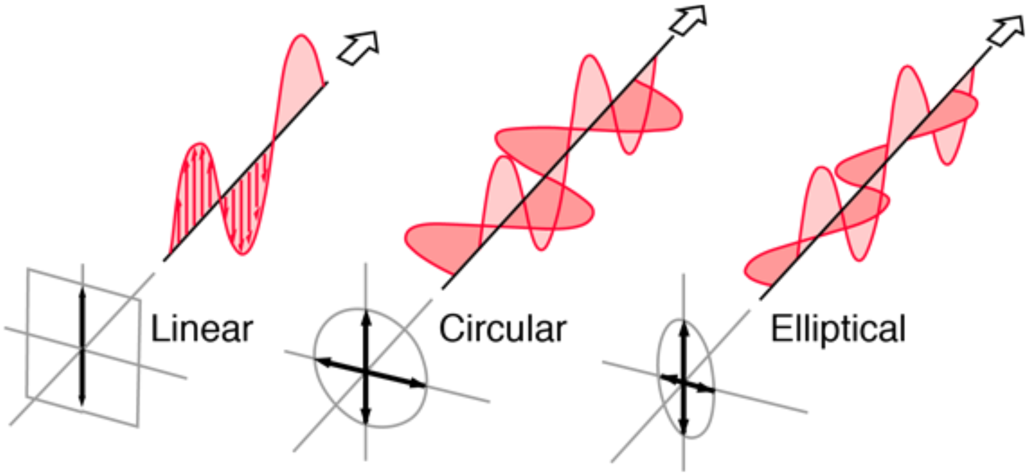

Figure 1.7: A figure showing the locus of the electric field in the different states of the polarization of light. The white arrows indicate the direction of propagation of the light. Image credit: Internet*

niques to unravel the mysteries of the cosmos. This is particularly evident in the study and inference of solar magnetic fields. Here, astrophysicists rely on interpreting the polarization profiles of incoming solar radiation. Polarization is a fundamental property of light that provides deep insights into the physical processes occurring in astrophysical environments, such as the Sun. It refers to the orientation and behavior of the oscillating electric field vector of an electromagnetic wave, like light. In more technical terms, when light is polarized, the electric field vector of the wave exhibits a specific orientation or pattern in the plane perpendicular to the direction of propagation of light. When the electric field vector of the light wave oscillates along a particular direction, then the light is said to be linearly polarized. If the tip of the electric field vector traces a circle, the light is said to be circularly polarized (see illustration in Fig. 1.7). In general, the light is a combination of both linear and circular polarization, termed elliptical polarization.

From a formal point of view, the x (and y) components of the electric field of a polychromatic beam propagating along the z-axis can always be put in the form (del Toro Iniesta, 2007)

$$E_x(t) = [\mathcal{E}_x(t)e^{i\phi_x(t)}]e^{-2\pi i v_0 t}, \tag{1.1}$$

where the polychromatic beam has a central frequency v_0 with width Δv, and

$$\mathcal{E}_x(t) = \sqrt{E_x(t)E_x^*(t)} = |E_x(t)|, \tag{1.2}$$

---

* `http://hyperphysics.phy-astr.gsu.edu/hbase/phyopt/polclas.html`

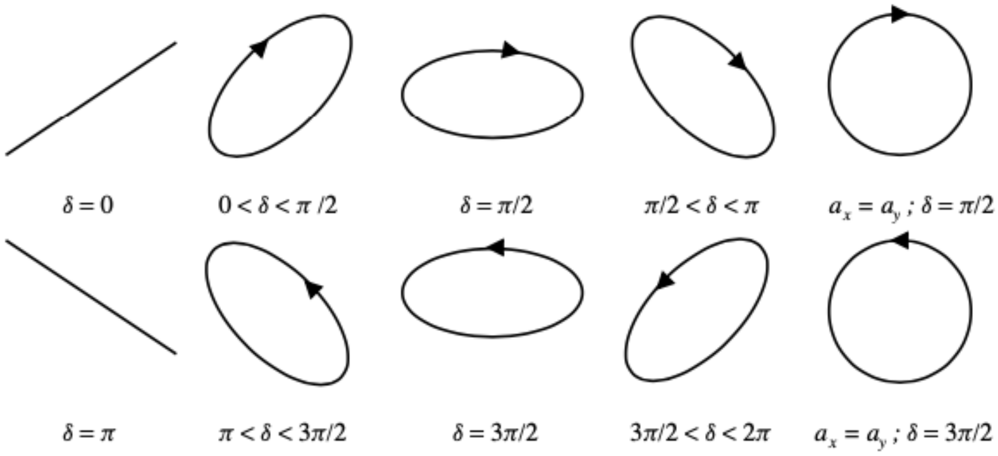

Figure 1.8: Depiction of various states of completely polarized light. The illustration shows that typically, a polychromatic wave exhibits elliptical polarization, with right-handed polarizations represented in the top row and left-handed polarizations in the bottom row. When one of the Cartesian components is zero or when both have different amplitudes but a phase difference equal to 0 or π, the ellipse becomes a straight line. Moreover, when the amplitudes of the Cartesian components are equal and $\delta(t) = \pi/2$ or $3\pi/2$, the ellipse becomes a circle. In this figure a_x and a_y are same as $\mathcal{E}_x$ and $\mathcal{E}_y$, respectively. Image credit: del Toro Iniesta (2007).

$$\phi_x(t) = 2\pi \upsilon_0 t + tan^{-1}\left\{\frac{Im[E_x(t)]}{Re[E_x(t)]}\right\} \tag{1.3}$$

where $*$ stands for complex conjugate.

However, detectors are not sensitive to the electric fields of electromagnetic radiation, but only to the electromagnetic energy or the intensity. Stokes parameters are, thus, a convenient alternative formalism to describe the polarization state in intensity units, as given here:

$$\begin{aligned} I =& \quad \kappa(\langle \mathcal{E}_x^2 \rangle + \langle \mathcal{E}_y^2 \rangle), \\ Q =& \quad \kappa(\langle \mathcal{E}_x^2 \rangle - \langle \mathcal{E}_y^2 \rangle), \\ U =& \; 2\kappa \langle \mathcal{E}_x \mathcal{E}_y \cos\delta(t) \rangle , \\ V =& \;\; 2\kappa \langle \mathcal{E}_x \mathcal{E}_y \sin\delta(t) \rangle , \end{aligned} \tag{1.4}$$

where $\delta(t) = \phi_x(t) - \phi_y(t)$ and κ is a dimensional constant that translates the Stokes parameters into intensity units. Figure 1.8 shows different states of totally polarized radiation for different values of $\delta(t)$.

Understanding the physical significance of the Stokes parameters necessitates a comprehension of their measurement methods. Figure 1.9 shows a simple polarimeter setup consisting of a retarder and an analyzer-polarizer to measure the Stokes parameters. A linear polarizer is an optical component that allows maximum transmission for the component of the electric field parallel to its optic axis while completely absorbing (or reflecting) the component of the electric field orthogonal to its optic axis.

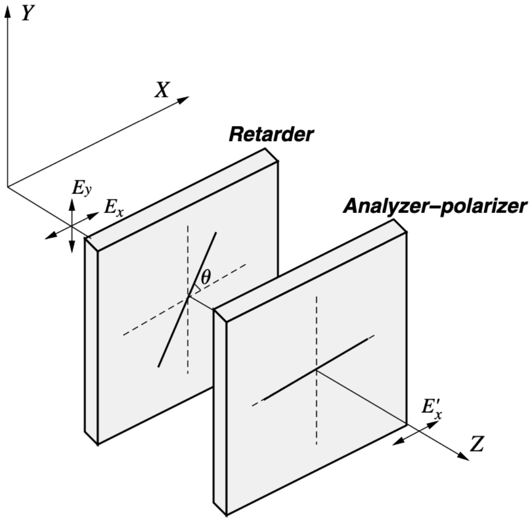

Figure 1.9: A basic polarimeter consisting of a linear retarder and an analyzer-polarizer. In this polarimeter illustration, the optic axis of the analyzer-polarizer is along the x-axis and the optic axis of the retarder is at angle θ counter-clockwise from the x-axis. Image credit: del Toro Iniesta (2007).

A linear retarder, on the other hand, imparts a retardance to one of the orthogonal components of the electric field with respect to the other. In the polarimeter shown in Fig. 1.9, the optic axis of the analyzer-polarizer is along the x-axis and the optic axis of the retarder is at angle θ counter-clockwise from the x-axis. Following del Toro Iniesta (2007), the measured intensity at the detectors after passing through the polarimeter shown in Fig. 1.9 is given by:

$$I_{meas}(\theta,\delta) = \frac{1}{2}(I + Q\cos 2\theta + U\cos\delta\sin 2\theta + V\sin\delta\sin 2\theta) \tag{1.5}$$

where $I_{meas}(\theta,\delta)$ is the measured intensity at the detector for a given θ and δ, θ is the angle between the optic axis between the analyzer and the retarder and δ is the retardance of the retarder.

By varying θ and δ, one can clearly show that,

$$\begin{aligned} I &= I_{meas}(0,0) + I_{meas}(\pi/2,0), \\ Q &= I_{meas}(0,0) - I_{meas}(\pi/2,0), \\ U &= I_{meas}(\pi/4,0) - I_{meas}(3\pi/4,0), \\ V &= I_{meas}(\pi/4,\pi/2) - I_{meas}(3\pi/4,\pi/2), \end{aligned} \tag{1.6}$$

Consequently, we can intuitively understand the Stokes parameters: I represents the total intensity of the beam, Q is the difference between the intensities of linear components oriented at 0° and 90°, U is the difference between the intensities of linear components oriented at 45° and 135°, and V is the difference between the intensities of the right-handed and left-handed circularly polarized components of the incoming quasi-monochromatic plane wave.

The measured Stokes parameters are used for further analysis to infer stratification of the atmospheric parameters of the stellar atmospheres.

1.4 Processes through which magnetic field information gets imprinted on the polarization of the incoming radiation

Polarization in spectral lines can arise from a variety of mechanisms, which are linked either to the influence of an external magnetic field or to the presence of anisotropy in the atomic system's excitation.

1.4.1 The Zeeman Effect

In the presence of the magnetic field, the modifications produced in the atomic spectra can be described by adding an additional term called the magnetic Hamiltonian (H_B) to the unperturbed Hamiltonian (H_0), (Landi Degl'Innocenti and Landolfi, 2004)

$$H_B = \frac{e_0 h}{4\pi mc}(\vec{L} + 2\vec{S}) \cdot B + \frac{e_0^2}{8mc^2}(\vec{B} \times \vec{r})^2, \tag{1.7}$$

where e_0 is the absolute value of the electron charge, m is the electron mass, h and c have their usual meaning of Planck constant and speed of light, $\vec{L}$ and $\vec{S}$ are the (dimensionless) total orbital angular momentum and total spin of the electronic cloud, $\vec{B}$ is the magnetic field vector, and $\vec{r}$ is the position operator defined by,

$$\vec{r} = \sum_i \vec{r}_i, \tag{1.8}$$

The second term in eq. 1.7 is the diamagnetic term. This term is negligible for the typical magnetic fields found in Sun and Sun type stars, thus eq. 1.7 can be re-written as,

$$H_B = \mu_0(\vec{L} + 2\vec{S}) \cdot B \tag{1.9}$$

where μ_0 is the Bohr magneton ($\mu_0 = 9.27 \times 10^{-21}$ erg G^{-1}).

If the magnetic field is weak enough that the magnetic Hamiltonian (H_B) can be treated as a small perturbation to the unperturbed Hamiltonian (H_0), then it is called the Zeeman Effect. In this case, the levels are described by the Russel-Saunders (or L-S) coupling scheme. Any level characterized by the quantum number J is split into $(2J + 1)$ equally spaced sublevels, the splitting being proportional to the Landé factor g and to the magnetic field. The magnetic Hamiltonian H_B removes the degeneracy between the $2J + 1$ magnetic sublevels. Formally, the eigenstates of

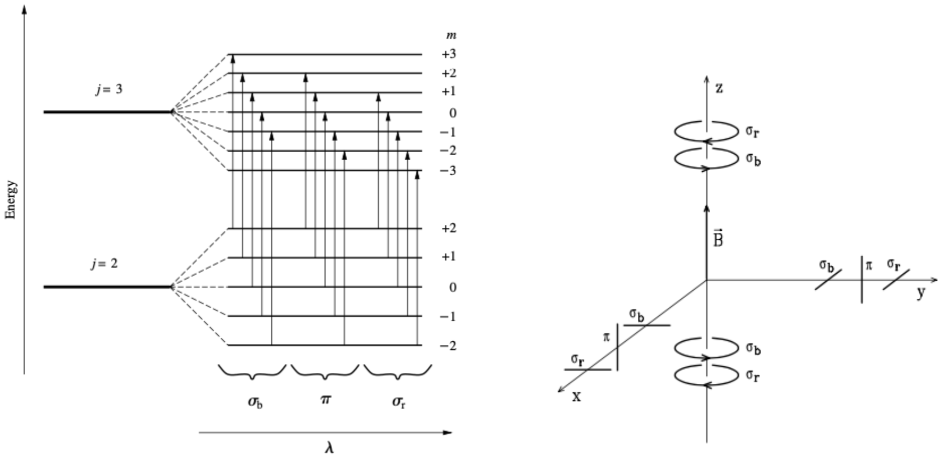

Figure 1.10: Illustration showing Zeeman Effect. The left panel shows the splitting of J levels into $2J+1$ sublevels. The allowed transitions are between $\Delta M = 0, \pm 1$. The components with $\Delta M = -1$ and $+1$ are called σ_r and σ_b, respectively. The components with $\Delta M = 0$ is called π component. The right panel shows the polarization properties of the radiation emitted by different Zeeman components depending on the type of component and on the angle between the observing direction and the magnetic field vector. Image credits: del Toro Iniesta (2007) and Landi Degl'Innocenti and Landolfi (2004).

the total Hamiltonian (H_0 + H_B) are of the form $|\alpha J M\rangle$, while the eigenvalues are given by

$$E_{\alpha J} + \mu_0 g B M \qquad (M = -J, -J+1, ..., J) \tag{1.10}$$

The Landé factor g for $L-S$ coupling is given by:

$$g_{LS} = 1 + \gamma(J, S, L) \tag{1.11}$$

where,

$$\gamma(A, B, C) = \frac{A(A+1) + B(B+1) - C(C+1)}{2A(A+1)} \tag{1.12}$$

Thus, in the presence of the magnetic field, instead of a single radiative transition between two J levels, owing to the splitting of the atomic levels, a collection of radiative transitions between different $|\alpha J M\rangle$ sublevels, limited by selection rules, will be observed. The selection rule for electric-dipole transitions is

$$\Delta M = 0, \pm 1 \tag{1.13}$$

Figure 1.10 illustrates the splitting of the atomic levels and polarization properties of different Zeeman components of spectral lines. The σ_r components (with $\Delta M = -1$) typically shift towards the longer wavelengths, or the red part of the spectrum, from the original line position. In emission, they give rise, in general, to elliptically polarized radiation. This elliptical polarization degenerates into circularly polarized radiation when viewed along the magnetic field direction, and becomes linearly polarized when observed perpendicularly to the field. Conversely, the σ_b components $\Delta M = +1$) shift towards shorter wavelengths, or the blue part of the spectrum, differing from the σ_r components mainly in the opposite circular polarization direction. The π components ($\Delta M = 0$) have wavelengths that lie between the σ_r and σ_b components. In emission, the π components result in linear polarization that is always aligned parallel to the magnetic field.

1.4.2 The Paschen-Beck Effect

In scenarios where the magnetic field's strength is sufficient to cause splitting at a J-level that is comparable with the energy differences between various J-levels, a different approach from the Zeeman effect is necessary. This scenario is identified as the Paschen-Back effect regime. Here, the energy levels are determined by diagonalizing the entire Hamiltonian H, rather than treating the magnetic Hamiltonian H_B as a minor perturbation. The magnetic Hamiltonian H_B connects only eigenstates having the same value of the magnetic quantum number M. This results in a block-diagonal structure where each block corresponds to a specific M-value. Consequently, the magnetic field induces a mixing of J-levels belonging to a particular term. However, the comprehensive task of computing the eigenvalues and eigenvectors of the H matrix in the presence of arbitrary magnetic fields can only be solved through numerical methods. This contrasts with the Zeeman effect regime, where J is a valid quantum number (Landi Degl'Innocenti and Landolfi, 2004). Figure 1.11 illustrates the effect of splitting and level-crossing of atomic levels with increasing magnetic field strength. At low normalized magnetic energies ($\frac{\mu_0 B}{\zeta} << 1$), the energy levels are well separated, indicating the Zeeman effect regime, here ζ, is the fine-structure energy. In the intermediate range, the eigenvalues begin to intersect, displaying a non-linear pattern characteristic of the incomplete Paschen-Back effect regime. At higher magnetic field strengths, the eigenvalues linearly correlate with the magnetic field strength, the complete Paschen-Back effect regime.

1.4.3 Resonance scattering and the Hanle Effect

As discussed before, the Zeeman effect can produce linear polarization through the transverse Zeeman effect in the presence of strong magnetic fields. However, even in the absence of strong magnetic fields, linear polarization is also generated by the coherent scattering of anisotropic radiation by atoms, known as scattering polarization. This anisotropy is primarily due to the vertical orientation of the radiation field, augmented by local inhomogeneities such as granulation. The degree of anisotropy increases with height, as the incoming radiation becomes increasingly unidirectional.

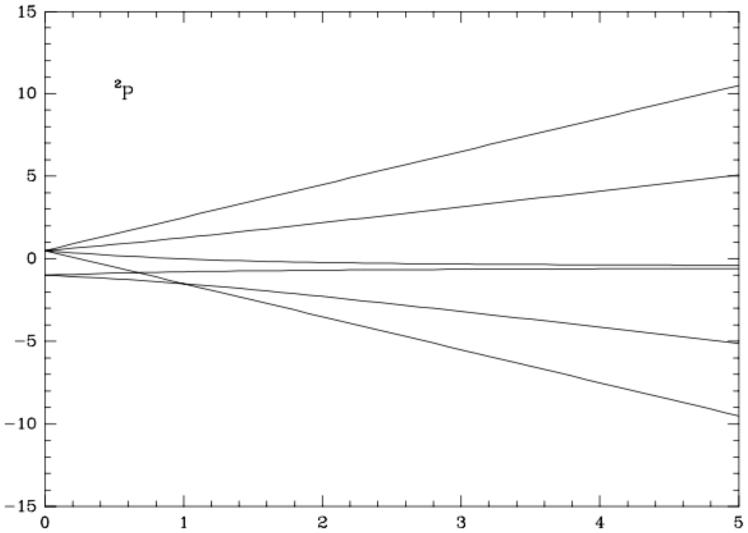

Figure 1.11: The energy levels of the term ^2P are plotted as functions of the magnetic field strength. The energy E (vertical scale) and the magnetic energy $\mu_0 B$ (horizontal scale) are both normalized to the fine-structure energy (ζ). Image credit: Landi Degl'Innocenti and Landolfi (2004).

In the absence of magnetic fields, the polarization of the scattered radiation is perpendicular to the plane of scattering. Therefore, at the solar limb, with a scattering angle of 90°, the resulting radiation exhibits linear polarization aligned parallel to the limb.

Hanle effect involves the modification of the scattering polarization of spectral lines under the influence of weak magnetic fields (Hanle, 1923; Stenflo, 1982). In this context, weak fields are those where the Zeeman splitting due to their presence is comparable to the natural width of the atomic levels. When observing the limb of the Sun in the presence of a weak magnetic field directed towards the observer, the Hanle effect induces depolarization and a counterclockwise rotation of the polarization plane. Conversely, if the field is horizontal and extends away from the observer, depolarization still occurs, but the polarization plane rotates in a clockwise direction. Notably, the Hanle effect is ineffective for magnetic fields that are either perpendicular to the line of sight or aligned with the radiation field's symmetry axis (Stenflo, 1982). Additionally, the Hanle effect is relevant in forward scattering scenarios (where the scattering angle is zero). While at the center of the solar disk, scattering typically does not produce polarization due to symmetry, the presence of weak, inclined magnetic fields can induce linear polarization through the Hanle effect (Trujillo Bueno et al., 2002).

1.5 Methods to infer the magnetic field

The propagation of electromagnetic energy through a stellar atmosphere is a complex, non-linear, three-dimensional, and time-dependent process involving the entire atmosphere's properties as a whole. This process includes non-local effects due to the coupling between the radiation field and atmospheric matter, implying the state of matter and radiation at a given depth may depend on that of at the other layers. Understanding this system requires solving coupled equations that describe both the physical state of atomic systems and the radiation field traversing them. Thus, for the purpose of inferring thermodynamic properties (including magnetic field) of stellar atmospheres, various simplifying assumptions, such as one-dimensional radiative transfer, are made. When the plasma is assumed in local thermodynamic equilibrium (LTE), the source function is assumed to vary linearly by the optical depth, and thermodynamic parameters are assumed constant with height; this assumption is called Milne-Eddington approximation (discussed in section 1.5.1). This assumption is very well suited for inference of the atmospheric parameters from spectral lines which are typically formed in the photosphere, such as the lines of Fe I atom. When the Zeeman splitting is much smaller than the Doppler width of the spectral lines, a perturbative approach can be applied to the polarized radiative transfer (RT) equations to get direct relations between the Stokes parameters and the magnetic fields. This approach, called weak field approximation, is discussed in section 1.5.2. Using this approach, magnetic fields of typically broad chromospheric lines (for example Ca II 8542 Å line) can be inferred. Non-local thermodynamic equilibrium (non-LTE) inversions, discussed in section 1.5.3, unlike the previous two methods, can be used to infer the height stratification of atmospheric parameters. This is achieved by solving the RT equations simultaneously with statistical equilibrium equations to get a consistent solution of the radiation field and the atom level populations. Compared to the above two methods, non-LTE inversions are significantly more computationally expensive.

1.5.1 The Milne-Eddington Inversion

The radiative transfer equation in 1D is given by:

$$\frac{\mathrm{d}\mathbf{I}}{\mathrm{d}\tau_c} = \mathbf{K}(\mathbf{I} - \mathbf{S}) \tag{1.14}$$

where τ_c is the continuum optical depth and $\mathbf{I} = (I, Q, U, V)^T$ is the light beam Stokes Vector. The source function vector ($\mathbf{S}$) and the propagation matrix ($\mathbf{K}$) are functions of τ_c. The matrix elements of $\mathbf{K}$ are made up of the various absorption and dispersion profiles which are characteristics of the medium and the relevant geometry. Detailed insights into the propagation matrix and the elements within can be found in del Toro Iniesta (2007). To solve equation 1.14, we need to know both $\mathbf{K}$ and $\mathbf{S}$, both of which are dependent on a height-dependent model atmosphere. Unfortunately, no analytical solution exists. Milne-Eddington (M-E) approximation allows for an analytical solution assuming a constant $\mathbf{K}$, i.e. a constant model atmosphere and linearly varying source function with optical depth. This solution, called the Unno–Rachkovsky solution (Unno, 1956; Rachkovsky, 1967) is expressed as,

$$\mathbf{I}(0) = \mathbf{S}_0 + \mathbf{K}_0^{-1}\mathbf{S}_1 \tag{1.15}$$

The solar atmosphere and the spectral line are described by 11 parameters. Five of these are thermodynamic parameters: the line-to-continuum absorption ratio (η_0), the Doppler width ($\Delta\lambda_D$), the damping parameter (a), source function at the observer (S_0), and the source function gradient (S_1). The magnetic field is represented by three parameters: magnetic field strength (B), field inclination (θ) with respect to the line-of-sight, and field azimuth (ϕ) in the plane perpendicular to the line-of-sight. The two kinematic parameters are: line-of-sight velocity (V_{LOS}) and macro-turbulent velocity ($\mathcal{E}_{mac}$). The V_{LOS} denotes the line-of-sight velocity of the magnetized plasma, whereas $\mathcal{E}_{mac}$ takes care of the unresolved velocity and instrumental smearing effect. The final parameter, the filling factor α, estimates the fraction of the area covered by the magnetic atmosphere in a pixel. In essence, a standard M-E model can be summarized by the vector M: [η_0, $\Delta\lambda_D$, a, S_0, S_1, B, θ, ϕ, V_{LOS}, $\mathcal{E}_{mac}$, α]. This approximation works very well for the photospheric lines such as lines of Fe I atom, which typically form deeper in the atmosphere where collision rates are high, and radiation is strongly coupled with the matter, due to the high density of the plasma. This thesis employs a spatially coupled and parallel implementation of the M-E inversion method, as outlined by de la Cruz Rodríguez (2019).

1.5.2 The Weak field approximation

When the magnetic field is weak, such that the Zeeman splitting ($\Delta\lambda_B$) is much smaller than the Doppler width ($\Delta\lambda_D$) of a spectral line, one can apply a perturbative scheme to radiative transfer equations to deduce simpler relations between the Stokes parameters and the magnetic field (Landi Degl'Innocenti and Landolfi, 2004). The weak field condition can be expressed as,

$$\bar{g}\,\frac{\Delta\lambda_B}{\Delta\lambda_D} << 1 \tag{1.16}$$

where $\bar{g}$ is the effective Landé factor.

Following the derivation given in Landi Degl'Innocenti and Landolfi (2004), the Stokes V is linearly related to the magnetic line-of-sight magnetic field and the derivative of the Stokes I, given by,

$$V(\lambda) = \Delta\lambda_B \; \bar{g} \; \cos\theta \; \frac{\partial I}{\partial \lambda} \tag{1.17}$$

and,

$$\Delta\lambda_B = 4.67 \times 10^{-13} \lambda_0^2 B \tag{1.18}$$

where $\Delta\lambda_B$ is expressed in Å, B in Gauss, $\bar{g}$ is effective Landé factor, θ is the inclination of B with respect to the line-of-sight (LOS), and λ_0 is the central wavelength of the spectral line (expressed in Å).

The Doppler width (in wavelength units),

$$\Delta\lambda_D = \frac{\lambda_0}{c}\sqrt{\frac{2K_B T}{m} + \xi^2} \tag{1.19}$$

increases with the temperature, T, and the microturbulent velocity, ξ, while it decreases with the mass of the atom, m. Here, K_B is the Boltzmann constant, and c is the speed of light.

The B_{LOS} can be derived from equation 1.17 using the linear regression formula (Martínez González and Bellot Rubio, 2009),

$$B_{\mathrm{LOS}} = -\frac{\Sigma_\lambda \frac{\partial I_{\smile}}{\partial \lambda} V(\lambda)}{C \Sigma_{\smile} (\frac{\partial I_{\smile}}{\partial \lambda})^2}, \tag{1.20}$$

where $C = 4.66 \times 10^{-13} \; \bar{g} \; \lambda_0^2$.

The linear polarization is related to the first and second derivatives of the Stokes I and the transverse component of the magnetic field $B_T = B \sin\theta$. If we choose the preferred reference frame (such that Stokes $U = 0$), then,

$$Q(\lambda_0) = -\frac{1}{4}\Delta\lambda_B^2 \bar{G} \sin^2\theta \frac{\partial^2 I}{\partial \lambda^2} \quad \text{for } \lambda = \lambda_0, \tag{1.21}$$

$$Q(\lambda_w) = \frac{3}{4}\Delta\lambda_B^2 \bar{G} \sin^2\theta \frac{1}{\lambda_w - \lambda_0} \frac{\partial I}{\partial \lambda} \quad \text{for } \lambda_w \text{ in the wing of the line}, \tag{1.22}$$

where $\bar{G}$ is the Landé factor for the transverse magnetic field.

This approximation is valid even when the plasma is no longer in LTE (non-LTE), and thus, can be used for broad chromospheric lines, for eg, Ca II 8542 Å line.

1.5.3 Non-LTE Inversions

In the chromosphere, where collisional rates are low, and radiation is not tightly coupled with physical conditions, the standard assumption of LTE becomes untenable. In the non-LTE regime, the role of scattering in the formation of spectral lines is significant. The atomic level populations are no longer constrained to conform to local Saha-Boltzmann equilibrium values, as statistical equilibrium (SE) is presumed. Statistical equilibrium suggests that radiation fields (across all directions and frequencies) and level populations remain constant over time (Rutten, 2003),

$$\frac{\mathrm{d}n_i(\vec{r})}{\mathrm{d}t} = \sum_{j\neq i}^{N} n_j(\vec{r})P_{ji}(\vec{r}) - n_i(\vec{r})\sum_{j\neq i}^{N} P_{ij}(\vec{r}) = 0 \tag{1.23}$$

Here, n_i denotes the population of a specific level, N represents the total number of levels influencing the population of n_i in any way, and j indexes all these levels. The transition rates P_{ij}, encompassing both radiative and collisional processes, are defined per particle in states i or j as

$$P_{ij} = R_{ij} + C_{ij} \tag{1.24}$$

where R_{ij}, and C_{ij} are radiative and collisional rates, respectively.

In a non-LTE regime, it is crucial to simultaneously solve the radiative transfer equation (RTE) and the statistical equilibrium equations (SEE) for a coherent solution. The non-LTE problem is inherently nonlinear and nonlocal. Nonlinearity arises because both the propagation matrix, which delineates the absorption and scattering of radiation, and the source function vector in the RTE are dependent on atomic-level populations. Simultaneously, the matrix elements of the SEE are influenced by the radiation field at each transition, derived from the RTE's solution. Nonlocality emerges due to the RTE-induced coupling between distant points in the computational grid. Given these nonlinear and nonlocal characteristics, iterative methods become essential to achieve a self-consistent solution of the RTE and SEE.

Figure 1.12 shows the block diagram of a typical non-LTE inversion process. The non-LTE inversions aim to infer a model atmosphere that produces synthetic observables that match the actual observations. By the model atmosphere, we understand the depth stratification of the thermodynamic quantities (temperature and pressure, T and P), the macroscopic, bulk line-of-sight velocity field, V_{LOS}, the magnetic field (represented by the B, the strength, γ, the inclination with respect to the LOS, and ϕ, the azimuth). The inversion codes, typically, also fit an ad-hoc parameter called microturbulence (ξ_{mic}) to fit the broadening of the spectral lines. Thus, there are, in total, $x = np + r$ model parameters, where n being the number of depth grid points throughout the atmosphere, p the number of physical quantities varying with depth, and r the number of quantities that are assumed constant throughout the LOS.

The inversions aim to find the values of x for which the mean squared error (χ^2) between the synthesized and observed Stokes profiles is minimum; χ^2 is given by,

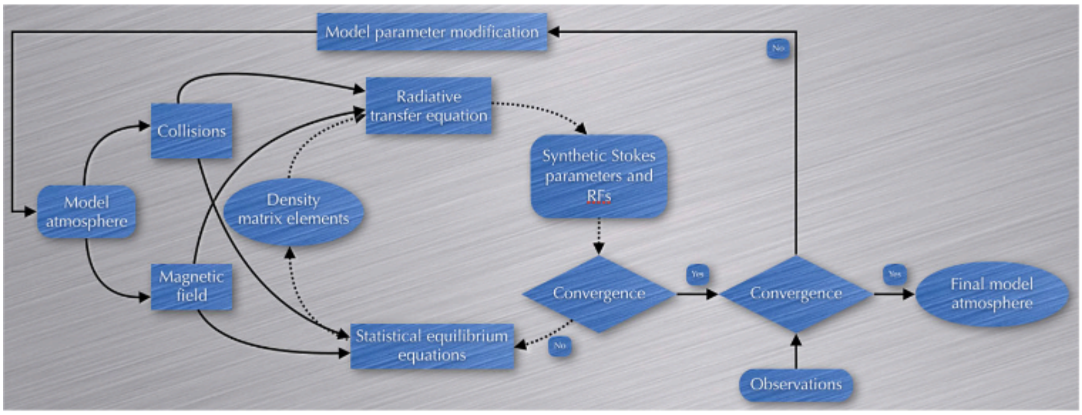

Figure 1.12: Block diagram of the inversion problem under non-LTE conditions. Image credit: (del Toro Iniesta and Ruiz Cobo, 2016)

$$\chi^2(x) = \frac{1}{N_f} \sum_{s=0}^{3} \sum_{i=1}^{q} [I_s^{obs}(\lambda_i) - I_s^{syn}(\lambda_i; x)]^2 w_{s,i}, \tag{1.25}$$

where index s runs for the four Stokes parameters, we assume q wavelength samples, and N_f stands for the number of degrees of freedom, that is, the difference between the number of observables ($4q$) and that of the free parameters (the number of elements in $x = np + r$). The weights $w_{s,i}$ can be used to favor some data more than others. For instance, one can set them to the inverse of the measurement errors, giving higher importance to more precise measurements and reducing the influence of noisier data.

Inversion codes begin with an initial guess model of the atmosphere, whose parameters are methodically adjusted in an effort to minimize the χ^2 distance between the synthesized and observed profiles. These atmospheric parameters are stratified based on optical depth. Within the inner, non-LTE loop, calculations for gas pressure and density stratification are performed under the assumption of hydrostatic equilibrium. Initially, the mean intensity of the radiation field is set to zero. Subsequently, using the stratifications for temperature and density, collisional rates are calculated and input into the RTE and SEE, along with the magnetic field. The atomic level populations are then determined by solving the SEE and are used in the RTE. The RTE, utilizing these computed atomic level populations, calculates the radiation field, which in turn is fed back into the SEE. This non-LTE loop continues until both the radiation field and atomic level populations converge below a predefined threshold (typically 10^{-4}). Post-convergence within the non-LTE loop, the synthesized Stokes parameters are matched against observational data. If the χ^2 distance is less than a set threshold (usually 10^{-6}), the iterative process, or inversions, conclude. Otherwise, the model parameters are modified based on response functions (RFs), prompting another iteration of the non-LTE loop. Response functions are partial derivatives of

Stokes parameters with respect to a physical parameter (X), given by (Beckers and Milkey, 1975),

$$RF_X(\tau, \lambda) = \frac{\partial I(\lambda)}{\partial X(\tau)} \tag{1.26}$$

Response functions contain information on how the Stokes parameters at different wavelength positions are sensitive to perturbations of a physical parameter at different optical depths. More details on the response functions and inversion methods are given in del Toro Iniesta and Ruiz Cobo (2016). In the work related to this thesis, the stratification of atmospheric parameters is retrieved using the MPI-parallel STockholm inversion Code (STiC de la Cruz Rodríguez et al., 2019; de la Cruz Rodríguez, Leenaarts, and Asensio Ramos, 2016).

1.6 Recent results on measurements of the magnetic field using simultaneous multiline spectropolarimetry and limitations

Magnetic field measurements within the photosphere are a standard practice, with significant advancements observed in techniques facilitating chromospheric magnetic field measurements. Among the most commonly employed lines for probing solar chromospheric magnetic fields are the Ca II 8542 Å and He I 10830 Å lines (Lagg et al., 2017). Noteworthy recent investigations include studies by Murabito et al. (2019), Joshi et al. (2017), Joshi et al. (2016), and Schad et al. (2015), which delve into the 3-D structure of magnetic fields of sunspots from photospheric to middle chromospheric regions. Additionally, numerous authors have explored magnetic field variations in umbral flashes (for example Felipe et al., 2023; French et al., 2023; Bose et al., 2019; Joshi and de la Cruz Rodríguez, 2018; Houston et al., 2018) and reported on the magnetic topologies of inverse Evershed flows (Prasad et al., 2022; Beck and Choudhary, 2019). Changes in the chromospheric field during flares have also garnered attention from researchers (Ferrente et al., 2023; Vissers et al., 2021; Yadav et al., 2021; Libbrecht et al., 2019; Kuridze et al., 2018; Kleint, 2017). For a detailed overview of advancements in measurement techniques and analysis methods, we refer the reader to Lagg et al. (2017).

Despite the benefits of employing these lines to investigate chromospheric magnetic fields, such as their well-understood line formation and the interpretability using non-local thermodynamic equilibrium (non-LTE) inversion codes (e.g. Socas-Navarro, Trujillo Bueno, and Ruiz Cobo, 2000b; Asensio Ramos, Trujillo Bueno, and Landi Degl'Innocenti, 2008; de la Cruz Rodríguez, Leenaarts, and Asensio Ramos, 2016; de la Cruz Rodríguez et al., 2019; Ruiz Cobo et al., 2022), they do present certain limitations. The formation of the He I 10830 Å line occurs within a limited range of heights in the upper chromosphere, and its formation relies on incoming EUV radiation from the coronal and transition region (Andretta and Jones, 1997; Leenaarts et al., 2016). This offers sensitivity to specific atmospheric layers but limits its applicability across different solar features, for example He I 10830 Å is only observed in and around active regions. In contrast, the Ca II 8542 Å line forms from the upper photosphere to the mid-chromosphere and sensitive to diverse solar features. However, in regions with heating such as flaring active regions, the Ca II ion gets ionized to the Ca III ion, potentially causing the Ca II 8542 Å line to sample deeper layers of the solar atmosphere (Kerr et al., 2016; Kuridze et al., 2018; Bjørgen et al., 2019). Thus, interpreting magnetic field measurements in dynamic environments using the Ca II 8542 Å line poses significant challenges.

1.7 Hα line as a potential chromospheric diagnostic

On the other hand, the Hα line appears to probe a relatively wider temperature range. Carlsson and Stein (2002) have demonstrated that the opacity of the Hα line in the upper chromosphere is determined by the ionization level and radiation field. Using 3-D radiative transfer calculations, Leenaarts, Carlsson, and Rouppe van der Voort (2012) have shown that the ionization level and radiation field remain insentitive to local temperature variations, as they are primarily influenced by mass density. More recently, Bjørgen et al. (2019) have further confirmed the opacity of the Hα line in flaring active regions through the synthesis of spectra using a 3D rMHD simulation. Consequently, the Hα line consistently maintains opacity within the chromosphere, making it a valuable diagnostic tool for studying the chromospheric magnetic field.

Despite the diagnostic potential of the Hα line, there have been limited reports of spectropolarimetric observations of the Hα line in the existing literature. For instance, Abdussamatov (1971) estimated the vertical magnetic field gradient by simultaneously observing the Fe 1 6302.5 Å and Hα lines. Comparisons between photospheric and chromospheric magnetic fields in sunspots have been documented in the literature through simultaneous spectropolarimetric observations of the Hα line and lines of the Fe I atom (Balasubramaniam, Christopoulou, and Uitenbroek, 2004; Hanaoka, 2005; Nagaraju, Sankarasubramanian, and Rangarajan, 2008). The radial variation of the line-of-sight magnetic field in the chromosphere and photosphere of a sunspot were discussed by Nagaraju, Sankarasubramanian, and Rangarajan (2020b). Spectropolarimetric observations of the Hα line have been utilized to diagnose magnetic fields in prominences (López Ariste et al., 2005). Jaume Bestard et al. (2022) recorded linear and circular polarization signals near the North and South Solar Limb and inferred the line-of-sight magnetic field using the weak-field approximation (WFA).

The limited number of reported spectropolarimetric observations of the Hα line can be attributed to the challenges associated with modeling this particular line. As a result, it has not been a preferred choice for chromospheric magnetometry. While the Stokes V signal is dominated by the Zeeman effect, both the intensity and polarization profiles of this line are highly sensitive to the three-dimensional (3-D) radiation field. In a study conducted by Socas-Navarro and Uitenbroek (2004), they performed calculations of one-dimensional (1-D) response functions for the Stokes parameters of the Hα line. Their findings revealed that the Hα line demonstrates significant sensitivity not only to chromospheric magnetic fields but also to photospheric magnetic fields. However, subsequent research by Leenaarts, Carlsson, and Rouppe van der Voort (2012) demonstrated that using 1-D radiative transfer is not a suitable approximation for accurately modeling the Hα line. Instead, the treatment of radiative transfer in 3-D is necessary. When the radiative transfer is properly handled in 3-D, the Hα line effectively traces chromospheric magnetic features such as fibrils, making it a valuable diagnostic tool for studying the chromosphere. This conclusion has been further supported by recent work conducted by Bjørgen et al. (2019). It is important to note, however, that the latter studies only focused on modeling the Stokes I and did not consider the polarization aspect.

1.8 Outline of the thesis

In this context, our initial project involved investigating the diagnostic capabilities of the Hα line for probing the chromospheric magnetic field using spectropolarimetric observations of a small pore recorded simultaneously in the Hα and Ca II 8542 Å lines. The contents of the study, Mathur et al. (2023), published in The Astrophysical Journal, are presented in its entirety as chapter 2. Motivated by the findings of the study, our primary focus was to simultaneously record spectropolarimetric observations of large sunspots using the Kodaikanal Tower Tunnel Telescope (KTT). More details about the KTT are provided in chapter 3. However, similar to other ground-based telescopes, KTT is susceptible to atmospheric turbulence or seeing, leading to random image aberrations that compromise spatial resolution and introduce spurious polarization (Lites, 1987; Judge et al., 2004; Krishnappa and Feller, 2012). To address this issue, it becomes imperative to employ systems such as tip-tilt and higher-order adaptive optics (Rimmele and Marino, 2011), which can correct for the seeing-induced motions. However, the KTT exhibits an inherent variable image drift that poses a limitation on the effectiveness of tip-tilt systems due to the limit of the actuator. Consequently, it becomes essential to incorporate an image autoguider system as a preliminary measure to counteract the effects of image drift before implementing systems like tip-tilt systems. Thus, we have developed, tested and installed an image autoguider system at the KTT to arrest the variable image drift (Mathur et al., 2022a). The contents of the above-mentioned study, Mathur et al. (2022a), are reproduced in its entirety as chapter 3. Furthermore, we have upgraded the KTT to allow for observing spectropolarimetric observations in three spectral lines simultaneously. This upgrade included the installation of a tip-tilt system which was integrated with the autoguider system. We present measurements of seeing-induced cross-talk using spectropolarimetric observations of sunspots recorded simultaneously in the Hα and Ca II 8662 Å lines with the Kodaikanal Tower Tunnel (KTT) telescope in chapter 4. The contents of the chapter 4 are accepted to be published in Applied Optics journal, Mathur et al. (2024a). Further, we present spectropolarimetric observations of an active region recorded simultaneously in the Hα and Ca II 8662 Å lines recorded while the tip-tilt and autoguider system were operational in chapter 5. The contents of the chapter 5 in its entirety are accepted to be published in The Astrophysical Journal, Mathur et al. (2024b). The chapter 6 summarizes the thesis and presents a chapter-wise summary. The novelty of this thesis and future work is also provided in chapter 6. Additionally, it should be noted that certain segments from chapters 2 to 5, including methods and introductory sections, are reiterated in this introductory chapter 1 to ensure coherence.

Chapter 2

Do Hα Stokes V profiles probe the chromospheric magnetic field? An observational perspective

Do Hα Stokes V profiles probe the chromospheric magnetic field? An observational perspective
Harsh Mathur, K. Nagaraju, Jayant Joshi, and Jaime de la Cruz Rodriguez, 2023,
The Astrophysical Journal, 946, 38.

In our first project, we explored the diagnostic potential of the Hα line to probe the chromospheric magnetic field using spectropolarimetric observations of a small pore simultaneously recorded in the Hα and Ca II 8542 Å lines. Towards this aim, we compared the stratification of the chromospheric magnetic field inferred from the non-LTE inversions of the Ca II 8542 Å line with that inferred from the WFA over the Hα line. We have used different wavelength ranges of the Hα line while performing WFA to infer the magnetic field's stratification. The contents of the study, Mathur et al. (2023), are reproduced in its entirety as this chapter. The following sections present a detailed introduction to the problem, followed by a description of the data and methodology. Further, we present the results and conclusions.

2.1 Introduction

Between the bright solar surface and million degrees hot corona, the chromosphere is one of the most dynamic and complex layers of the solar atmosphere. Understanding the magnetic coupling of the chromosphere with the photosphere, transition region and corona may reveal how mass and energy are supplied to the corona and heliosphere. Therefore, simultaneous magnetic field measurements at multiple heights of the solar atmosphere are important.

Magnetic field measurements in the photosphere are routinely made, and significant progress has been made in the techniques that allow for chromospheric magnetic field measurements. The most widely used lines to probe the magnetic field of the solar chromosphere are the Ca II 8542 Å and He I 10830 Å lines (Lagg et al., 2017). While using these lines to probe the chromospheric magnetic field has its advantages like the relatively well-understood line formation, and they can be interpreted utilizing non-local thermodynamic equilibrium (non-LTE) inversion codes (e.g. Socas-Navarro, Trujillo Bueno, and Ruiz Cobo, 2000b; Asensio Ramos, Trujillo Bueno, and Landi Degl'Innocenti, 2008; de la Cruz Rodríguez, Leenaarts, and Asensio Ramos, 2016; de la Cruz Rodríguez et al., 2019; Ruiz Cobo et al., 2022), they also have some limitations. The He I 10830 Å line forms in a narrow range of heights in the upper chromosphere, and line formation depends on coronal and transition region EUV radiation (Andretta and Jones, 1997; Leenaarts et al., 2016). The Ca II 8542 Å line forms from the upper photosphere to the mid-chromosphere, however, the Ca II ion gets ionized to the Ca III ion in flaring regions, and hence the Ca II 8542 Å line itself may sample deeper layers of the solar atmosphere (Kerr et al., 2016; Kuridze et al., 2018; Bjørgen et al., 2019).

On the other hand, the Hα line seems to probe a relatively wider temperature range. Carlsson and Stein (2002) have shown that the Hα opacity in the upper chromosphere is determined by the ionization degree and radiation field. Using 3-D radiative transfer calculations, Leenaarts, Carlsson, and Rouppe van der Voort (2012) have shown that ionization degree and the radiation field are insensitive to local temperature variations over time but determined by mass density. More recently, Bjørgen et al. (2019) have also confirmed that the Hα line retains opacity even in flaring active regions by synthesizing spectra using a 3D rMHD simulation. Therefore, the Hα line always retains opacity in the chromosphere.

In spite of the diagnostic capabilities of the Hα line, very few spectropolarimetric observations have been reported in the literature. For example, Abdussamatov (1971) estimated vertical magnetic field gradient using simultaneous measurements of the Fe I 6302.5 Å and Hα lines. Simultaneous spectropolarimetric observations from the Hα line and lines of Fe I atom have been reported in the literature to compare the photospheric and chromospheric magnetic fields in sunspots (Balasubramaniam, Christopoulou, and Uitenbroek, 2004; Hanaoka, 2005; Nagaraju, Sankarasubramanian, and Rangarajan, 2008). Radial variation of the line-of-sight magnetic field in the chromosphere and photosphere of a sunspot were discussed by Nagaraju, Sankarasubramanian, and Rangarajan (2020b). Magnetic fields in prominences were diagnosed using spectropolarimetric observations of the Hα line (López Ariste et al., 2005). Jaume Bestard et al. (2022) studied linear and circular polarization signals near the North and South Solar Limb and inferred the LOS magnetic field using the weak field approximation (WFA).

The reason for so few spectropolarimetric observations of the Hα line have been reported and why this has not been a preferred line for the chromospheric magnetometry is because it is challenging to model the Hα line. Though the Stokes V signal is dominated by the Zeeman effect, both the intensity and polarization profiles of this line are sensitive to the 3D radiation field. Furthermore, in case of weakly magnetized atmospheres, the Stokes Q & U signals are sensitive to atomic polarization (Štěpán and Trujillo Bueno, 2010, 2011), making this line difficult to model using the currently available inversion codes which adopt 1.5D plane-parallel geometry. It is also important to note that in the weak field regime (when Zeeman Splitting, $\Delta\lambda_{\rm B}$, is much smaller than the Doppler width, $\Delta\lambda_{\rm D}$), the amplitude of circular polarization is proportional to the ratio of $\Delta\lambda_{\rm B}$ to $\Delta\lambda_{\rm D}$, and the linear polarization is proportional to the square of that ratio (for more details see page 405 of Landi Degl'Innocenti and Landolfi, 2004)). This ratio, owing to the light weight of the Hydrogen atom-thus correspondingly large Doppler width, is typically small compared to that in the case of heavier atoms like Calcium.

In a study by Socas-Navarro and Uitenbroek (2004) who calculated 1-D response functions of Stokes parameters of the Hα line and showed that it exhibits significant sensitivity to the photospheric magnetic fields in addition to the chromospheric magnetic fields. However, it has been shown by Leenaarts, Carlsson, and Rouppe van der Voort (2012) that 1-D radiative transfer is not a good approximation to model the Hα line, treatment of radiative transfer in 3-D is necessary. When the radiative transfer is treated in 3-D, the Hα line traces the chromospheric magnetic features like fibrils, and it has been shown that it is a good chromospheric diagnostic. This finding is further supported by recent work by Bjørgen et al. (2019).

In this study, we explore the diagnostic potential of the Hα line to probe the chromospheric magnetic field using spectropolarimetric observations simultaneously recorded in the Hα and Ca II 8542 Å lines. We compare the magnetic field inferred using the WFA method on the Stokes I and V profiles of the Hα spectral line with the stratification (from the photosphere to the chromosphere) of line-of-sight (LOS) magnetic field inferred using the inversions of the Ca II 8542 Å line using a non-LTE inversion code.

2.2 Observations

The observations were made with the Spectro-Polarimeter for Infrared and Optical Regions (SPINOR: Socas-Navarro et al., 2006) instrument at the Dunn Solar Telescope (Dunn, 1969) at the Sacramento Peak Observatory in the Hα and Ca II 8542 Å lines simultaneously. The Fe I 6569 Å line was recorded in the Hα spectrum and the Si I 8536 Å and Fe I 8538 Å lines were recorded in the Ca II 8542 Å spectrum. The spectral sampling of the Hα and Ca II 8542 Å lines data are 22 mÅ and 33 mÅ, respectively. The pixel scale corresponds to $\sim 0\overset{''}{.}38$ on the solar surface along the slit.

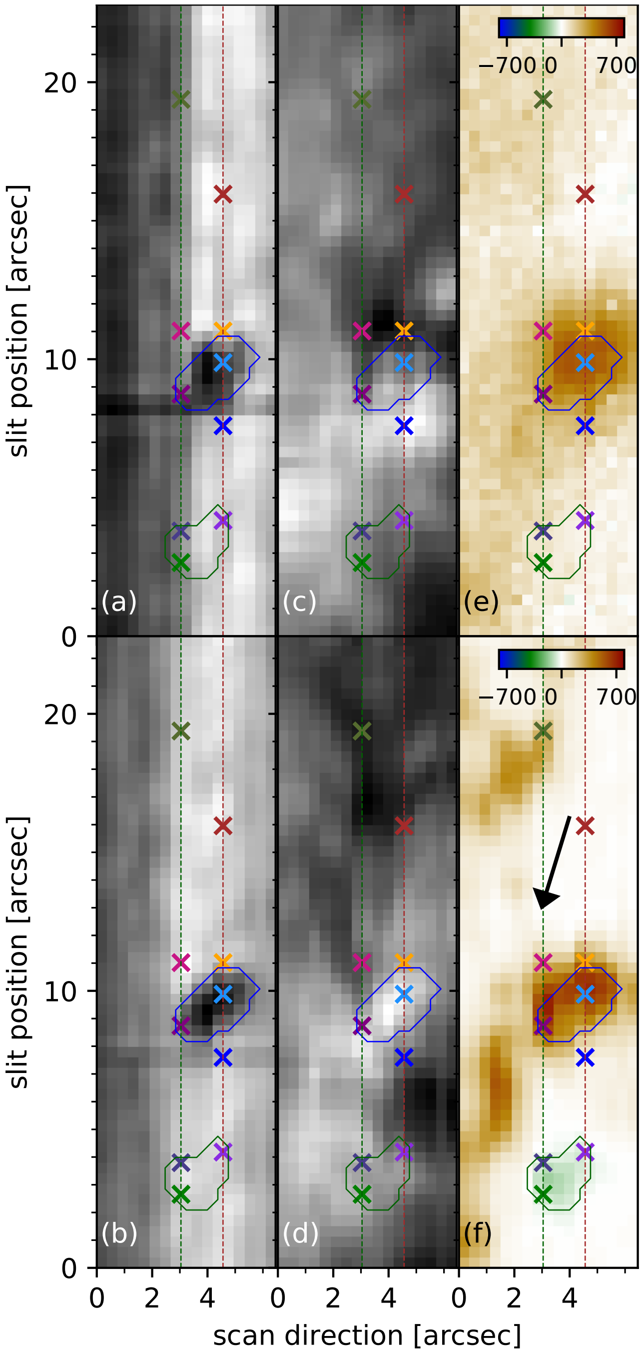

Figure 2.1: Field of view with a pore in the center as observed by the Dunn Solar Telescope on 4th December 2008: (a) Far wing image at an offset of −7 Å from the Ca II 8542 Å line, (b) Far wing image at an offset of +7 Å from the Hα line (c) Ca II 8542 Å line core image (d) Hα line core image. Panels (e) and (f) show LOS magnetic field maps derived under weak field approximation from the Ca II 8542 Å line within the spectral range of ±0.25 Å and Milne-Eddington inversions of the Fe I 6569 Å line, respectively. The blue contours show the location of the pore made using intensity thresholding on the far wing image of Hα line in panel (b). The green contours show the location of the region with the negative polarity of the magnetic field seen in panel (f). The arrow indicates the disc-center direction.

The observed field of view (FOV) consists of a pore centered at North $28^o.3$ and East $16^o.7$ in Stonyhurst Heliographic coordinates system on December 4, 2008, starting at 15:35 UT with a viewing angle $\cos\theta = \mu = 0.8$. Here, θ is the angle between the LOS direction and the local surface normal. Twenty spectropolarimetric raster scans of 20 slit positions with a step size of $0\overset{\prime\prime}{.}375$ were recorded; however, only four scans had good seeing conditions, and only the first scan is used in this study. Adaptive optics (AO; Rimmele, 2000) were used during the observations. The data were corrected for dark and flat field variations and instrumental polarization. The details are given in appendix A.1. In spite of strictly simultaneous observations, there was a spatial shift, due to atmospheric refraction, between the images at these two wavelengths, which were taken care of by co-aligning the Hα data with the Ca II 8542 Å data by cross-correlating the far wing images of the Hα and Ca II 8542 Å lines. The signal-to-noise ratio (SNR) in the Hα data is higher (5×10^3) than in the Ca II 8542 Å data (10^3).

An overview of observations is shown in Fig. 2.1. A pore almost centrally located in the FOV can be seen in the far wing images of the Ca II 8542 Å and Hα lines (see panels (a) and (b) of Fig. 2.1). The pore morphologically has a different shape in the Ca II 8542 Å and Hα lines and is brighter in the Hα line core image (see panels (c) and (d) of Fig. 2.1). Panels (e) and (f) show the LOS magnetic field (B_{LOS}) inferred from the Ca II 8542 Å and Fe I 6569 Å lines, respectively. More details on the methods to infer the B_{LOS} are discussed in section 2.2. There is an opposite polarity region near the pore visible in the photosphere that is absent in the WFA B_{LOS} map of the chromosphere.

The quiet-Sun profiles for the Hα and the Ca II 8542 Å lines were calculated by averaging profiles of a few pixels in a region away from the pore with negligible signal in the Stokes V profiles. As explained in appendix A.1, the wavelength calibration was done by comparing the quiet-Sun profile with the BASS 2000 atlas profile. The Ca II 8542 Å and Hα data were also corrected for spectral veil.

In the following paragraphs, we discuss a few selected profiles which are chosen such that they show distinct features from one another corresponding to various dynamics observed in the FOV. In the top two panels of Fig. 2.2 we present sample spectral images of Stokes I and V corresponding to a slit position marked by a brown line in Fig. 2.1. In the bottom two panels of Fig. 2.2, we show a few profiles from selected spatial locations marked using colored horizontal lines in the top two panels. The left and right columns of panels correspond to the Ca II 8542 Å and Hα spectrum, respectively.

There is a hint of enhancement in the intensity in the red wing of the Ca II 8542 Å line profile at 8542.38 Å ($\Delta v = +10.31$ km s^{-1}), at slit position near $\sim 4\overset{\prime\prime}{.}2$ with the line core position (8542.04 Å) slight blue-shifted ($\Delta v = -1.5$ km s^{-1}) compared to the quiet-Sun profile (see violet-colored profile). The corresponding Hα profile shows nominal absorption. The violet-colored profile lies in the opposite polarity region.

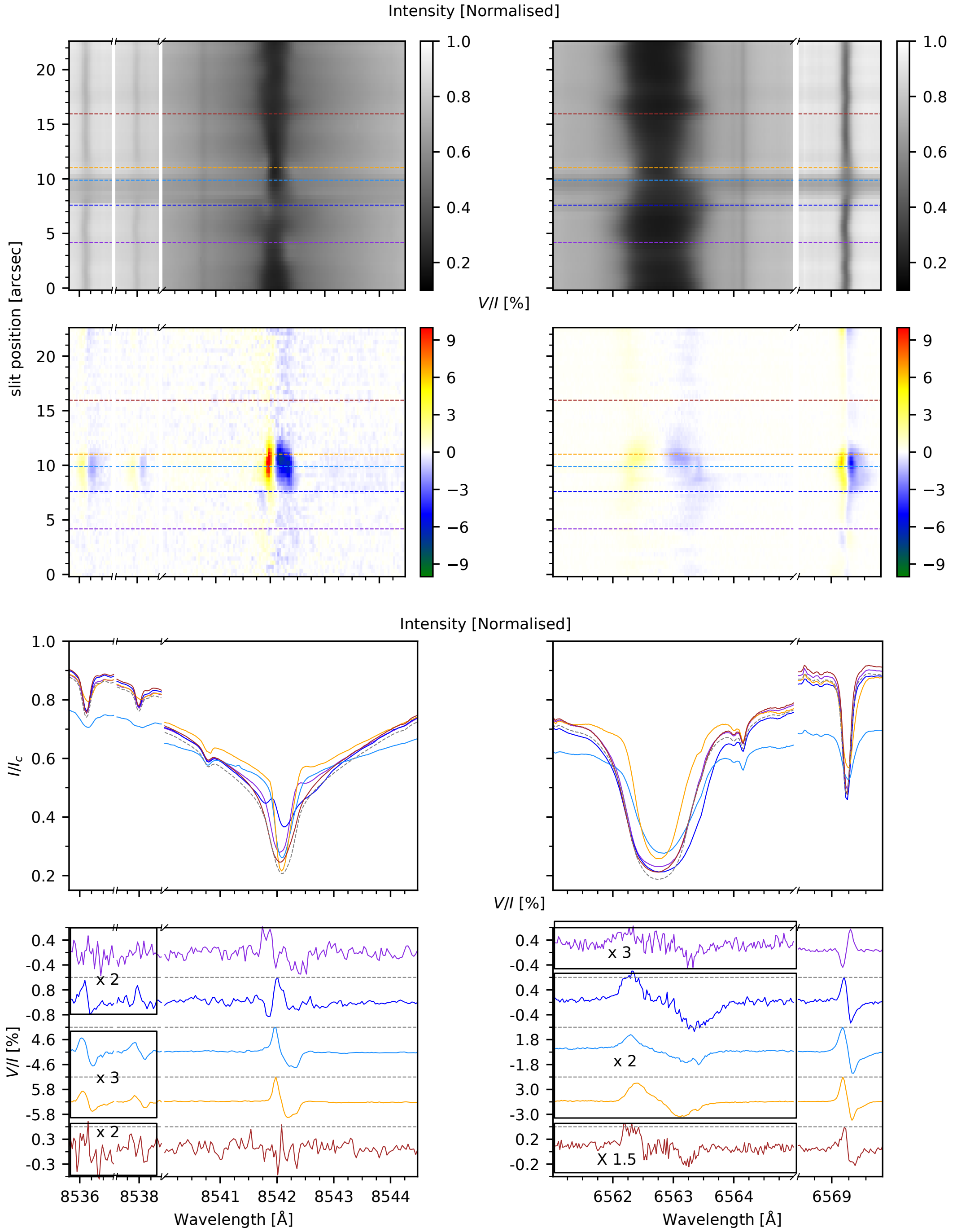

Figure 2.2: Sample Ca II 8542 Å and Hα line profiles over one slit position located over the pore and surrounding region (marked by the brown dashed line in Fig. 2.1). The top two panels show the spectral images of Stokes I and V, respectively. A few selected profiles marked by colored dashed lines are plotted in the bottom two panels. The quiet-Sun profile (gray dashed) is also shown in the intensity plots for comparison. For better visibility, the amplitudes of a few Stokes V profiles are artificially multiplied by the factors as indicated in the respective panels.

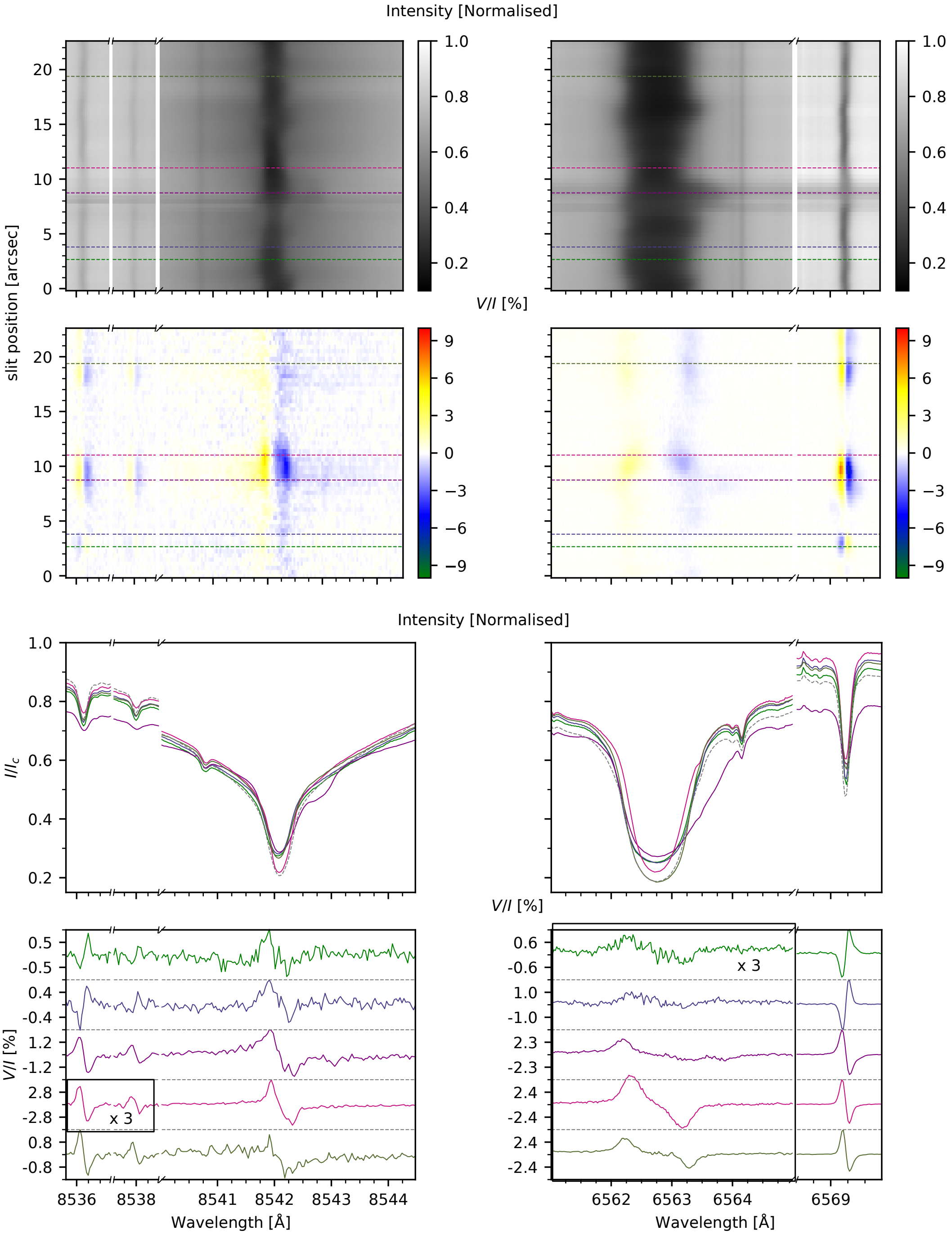

Figure 2.3: Same as Fig. 2.2 but for the slit passing through the region over negative polarity seen in B_{LOS} map inferred from ME inversions (see green line in Fig. 2.1).

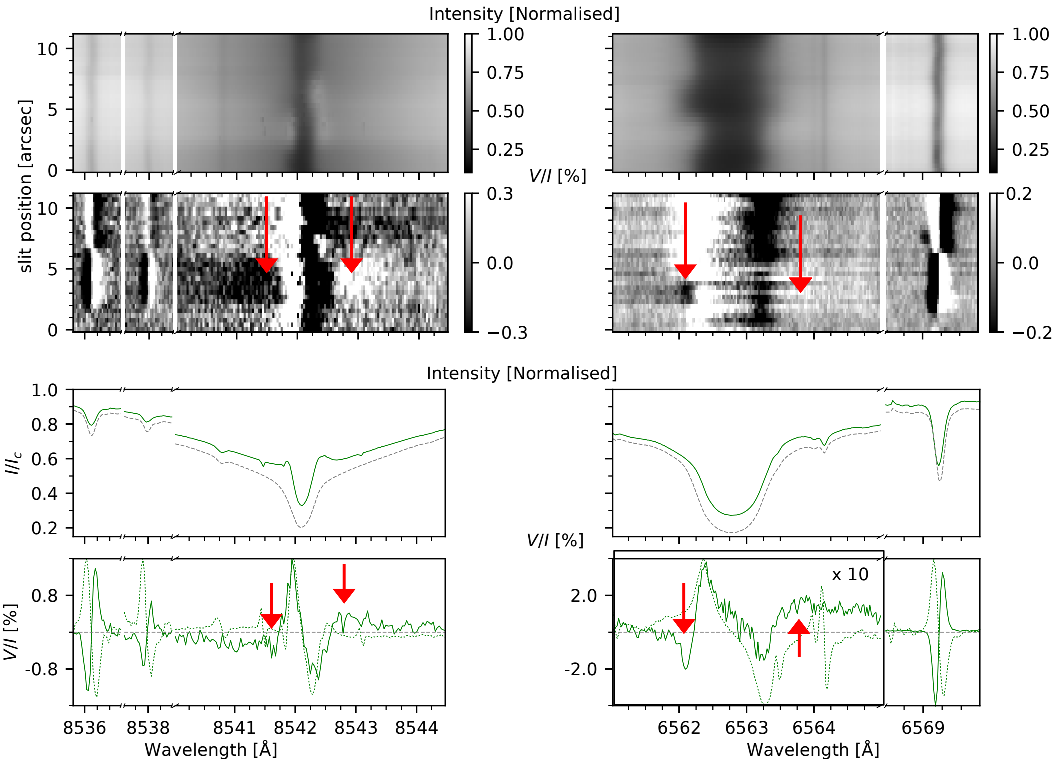

Figure 2.4: Sample Ca II 8542 Å and Hα line profiles over a region (in another raster scan map) with opposite polarity in the photospheric and chromospheric lines. The top two panels show the spectral images of Stokes I and V, respectively. An average Stokes I and V profile over the opposite polarity region is shown in the bottom two panels. The arrow indicates the wavelength position of the peak amplitude of the polarity reversal. The dotted green profile shows the derivative of Stokes I multiplied by -1. The quiet-Sun profile (gray dashed) is also shown in the intensity plots for comparison. For better visibility, the amplitudes of the Stokes V profile of the Hα line are artificially multiplied by the factors as indicated in the respective panel.

The Stokes V profiles of the Ca II 8542 Å and Hα lines have weak signal with sign opposite to that of the Stokes V profile of the Fe I 6569 Å. There is hardly any signal in the Stokes V profile of the Si I 8536 Å and Fe I 8538 Å lines that is above the noise level. This is because, as noted above, the SNR in Ca II 8542 Å spectrum is about 5 times lower compared to that of Hα spectrum.

The intensity profile of the Ca II 8542 Å line at slit position near $7''.8$ (blue-colored profile) shows emission in the blue wing at 8541.9 Å ($\Delta v = -6.56$ km s^{-1}) and line core (8542.12 Å) redshifted ($\Delta v = +1.4$ km s^{-1}), signature of surge flow (more details are discussed in Nagaraju et al. under prep.). The corresponding Hα and the wings of Ca II 8542 Å intensity profiles also show red excursion compared to the quiet-Sun profile. The Stokes V profile of the Ca II 8542 Å line shows a sign reversal compared to the Stokes V profile of the Fe I 6569 Å which is not due to change in the polarity of the magnetic field but due to emission in the blue wing (Sanchez Almeida, 1997). Such emission feature can only be caused by a change in the gradient of the source function, which also affects the sign of the Stokes V signal.

A sample profile over the pore is shown in cyan color. The Ca II 8542 Å and Hα lines show asymmetric Stokes V profiles with blue and red lobe amplitudes of (~9%, ~6%) and (~1.3%, ~0.9%), respectively. In contrast, the Si I 8536 Å, Fe I 8538 Å and Fe I 6569 Å lines show relatively symmetric Stokes V profiles of amplitudes ~1.6%, ~1% and ~3.5% respectively.

There is a hint of enhancement in the red wing of the Ca II 8542 Å line profile at the edge of the pore (yellow colored profile). The Stokes V profiles of the Ca II 8542 Å and Hα lines (similar to cyan-colored profile) show amplitude asymmetry. This could be because of the presence of multiple Stokes components within one resolution element (Socas-Navarro, Trujillo Bueno, and Ruiz Cobo, 2000a) or gradients in LOS velocity and magnetic field (Sankarasubramanian and Rimmele, 2002).

The brown-colored profile is an example of a quiescent profile away from the pore region. The Stokes V amplitudes of the Ca II 8542 Å and Hα line profiles are similar (0.2%).

Fig. 2.3 shows spectropolarimetric images and spectral profiles for the slit position shown in green color in Fig. 2.1 which passes over a location with stronger field within the negative polarity region and the pore edge. The profiles over the negative polarity region are shown in green and purple colors. The Stokes V amplitudes of the Si I 8536 Å and Ca II 8542 Å lines are ~0.7%. The green and purple colored intensity profiles of the Ca II 8542 Å line are blueshifted by about $\Delta\lambda = -0.04$ and -0.02 Å ($\Delta v = -1.4$ and 0.7 km s^{-1}), respectively, whereas there is no Doppler shift seen in the Si I 8536 Å and Fe I 8538 Å lines. The sign of the Stokes V profiles of the Si I 8536 Å, Fe I 8538 Å and Fe I 6569 Å lines is opposite to that of the sign of the Stokes V profiles of the Ca II 8542 Å and Hα lines which suggest that the Stokes V profile of the Hα line probes the chromospheric magnetic field. This most probably is because the Hα and Ca II 8542 Å line cores are sampling the canopy fields extending from a nearby region and overlying the opposite polarity region. To further demonstrate the existence of such field configuration, we show in Fig. 2.4 sample spectral images and profiles of the same region but from a raster scan recorded at a later time (16:08 UT). As clearly seen in this figure that the sign of the Stokes V profiles corresponding to the core of Ca II 8542 Å and Hα lines are opposite to that of Stokes V profiles of the photospheric lines viz., Si I 8536 Å, Fe I 8538 Å, and Fe I 6569 Å (see spectral images from $2''$ to $6''$). On the other hand, the Stokes profiles in the wings of the Ca II 8542 Å and Hα lines show the polarity the same as that of the photospheric lines. This is consistent with the canopy field scenario as explained above since the line wings of Hα and Ca II 8542 Å lines form deeper in the solar atmosphere, and hence the Stokes V profiles have the same sign as that of the photospheric lines. However, as noted before, under weak field conditions, the Stokes V profiles change sign when the spectral features change from absorption to emission or vice-versa. In order to make sure that the change in sign of Stokes V profiles from core to wing of the chromospheric lines is actually because of the change in polarity of the magnetic field but not due to change in spectral features, we have over-plotted the first derivative of Stokes I ($\frac{dI}{d\lambda}$: the dotted green curves in the bottom panel of Fig. 2.4 with the sign changed) over the Stokes V profiles. The reason for doing this is that under weak field conditions, Stokes V profile resembles $\frac{dI}{d\lambda}$ profile (see section 2.3.1). The comparison between the Stokes V and $\frac{dI}{d\lambda}$ profiles clearly demonstrate that the Stokes V sign change from core to wings of the chromospheric lines is due to the change in the polarity of the magnetic field but not due to change in the emission or absorption features of Stokes I.

The profile shown in maroon color (Fig. 2.3) is another example of a profile in pore region. There is a red excursion in the Ca II 8542 Å line wings and Hα line core profile corresponding to a surge flow. The Stokes V profiles of the Ca II 8542 Å, Hα, and Fe I 6569 Å lines show amplitude asymmetry, and the blue lobe show a positive sign suggesting positive polarity of the B_{LOS}.

The pink and khaki-colored profiles show profiles away from the pore region. The intensity profiles of the Ca II 8542 Å and Hα lines are similar to that of the quiet-Sun profile. Amplitude asymmetry is present in the Stokes V profiles of the Ca II 8542 Å and Hα lines.

2.3 Methods

2.3.1 Weak field approximation

The magnetic field from the Hα spectral line was inferred using the WFA. Under WFA the Stokes V is linearly related to B_{LOS} and $(\partial I/\partial \lambda)$ through (Landi Degl'Innocenti and Landolfi, 2004)

$$V(\lambda) = -\Delta\lambda_{\mathrm{B}}\, \bar{g} \cos\theta\, \frac{\partial I}{\partial \lambda}, \tag{2.1}$$

and

$$\Delta\lambda_{\mathrm{B}} = 4.67 \times 10^{-13} \lambda_0^2 B, \tag{2.2}$$

where $\Delta\lambda_{\mathrm{B}}$ is expressed in Å, B in Gauss, $\bar{g}$ is effective Landé factor, θ is the inclination of B with respect to the LOS, and λ_0 is the central wavelength of the spectral line (expressed in Å).

The B_{LOS} can be derived from Eq.2.1 using the linear regression formula (e.g., Martínez González and Bellot Rubio, 2009),

$$B_{\mathrm{LOS}} = -\frac{\Sigma_{\lambda} \frac{\partial I_{\smile}}{\partial \lambda} V(\lambda)}{C \Sigma_{\smile} (\frac{\partial I_{\smile}}{\partial \lambda})^2}, \tag{2.3}$$

where $C = 4.66 \times 10^{-13}\, \bar{g}\, \lambda_0^2$.

We have used $\bar{g} = 1.048$ following the investigation done by Casini and Landi Degl'Innocenti (1994). We derived three values of B_{LOS}, one from the line core (Hα ± 0.35 Å), the line wings ($[-1.5, -0.6]$ and $[+0.6, +1.5]$ Å), and over the full Hα spectral line (Hα ± 1.5 Å). The spectral blends listed in Table 2.1 were excluded while calculating B_{LOS} using the WFA, as have done by Jaume Bestard et al. (2022) and Nagaraju, Sankarasubramanian, and Rangarajan (2020b). The WFA is applied on the Ca II 8542 Å line within the wavelength range $\lambda_0 \pm 0.25$ Å and the inferred B_{LOS} map is shown in panel (e) of Fig. 2.1. The uncertainties in the values of B_{LOS} inferred from applying the WFA to the Ca II 8542 Å and Hα data were estimated to be 23 and 18 G, respectively.

λ_0 [Å]	$\Delta\lambda_0$ [Å]	Line
6562.44	0.05	V 2
6563.51	0.15	Co 1
6564.15	0.35	Unknown

Table 2.1: The first and second column define the spectral blends removed before applying the WFA: $\lambda_0 \pm \Delta\lambda$. The third column indicates the element of the transition in case it is known.

2.3.2 Milne-Eddington inversion

We performed Milne-Eddington (ME) inversions (see chapter 11 of del Toro Iniesta, 2007) of the Fe I 6569 Å data to infer the B_{LOS} (panel (f) of Fig. 2.1) utilizing pyMilne code, a parallel C++/Python implementation* (de la Cruz Rodríguez, 2019). The B_{LOS} from the Hα line is inferred from the WFA as explained in section 2.3.1. The

---

*https://github.com/jaimedelacruz/pyMilne stratification of the B_{LOS} from the photosphere to the chromosphere is inferred using simultaneous multi-line non-LTE inversions explained in section 2.3.3.

2.3.3 Non-LTE inversion

Table 2.2: Node positions ($\log \tau_{500}$ scale) used for inversions of different categories of profiles in T, V_{LOS}, V_{turb}, and B_{LOS}

Parameters	Category	Cycle 1	Cycle 2
T	Quiescent	−5.5, −4,5, −3.5, −2.5, −1.5, 0	−5.5, −4.5, −3.5, −2.5, −1.5, 0
	Emission	−4.8, −3.8, −2.9, −1.8, −0.9, 0	−4.8, −3.8, −2.9, −1.8, −0.9, 0
V_{LOS}	Quiescent	−4.5, −1	−4.5, −1
	Emission	−6, −4.5, −3, −1	−6, −4.5, −3, −1
V_{turb}	All	−5,−4, −3, −1	−5,−4, −3, −1
B_{LOS}	All	–	−4.5, −1

The MPI-parallel STockholm inversion Code (de la Cruz Rodríguez et al., 2019; de la Cruz Rodríguez, Leenaarts, and Asensio Ramos, 2016) is used to retrieve the stratification of atmospheric parameters. STiC is based on a modified version of the RH radiative transfer code (Uitenbroek, 2001) and solves the polarised radiative transfer equation using cubic Bezier solvers (de la Cruz Rodríguez and Piskunov, 2013). In non-LTE, assuming statistical equilibrium, it can fit multiple spectral lines simultaneously. It employs the fast approximation to account for partial re-distribution effects (PRD) (for more details Leenaarts, Pereira, and Uitenbroek, 2012). STiC assumes plane-parallel geometry to fit the intensity in each pixel (also called the 1.5D approximation). STiC uses an LTE equation-of-state obtained from the library functions in the Spectroscopy Made Easy (SME) package code (Piskunov and Valenti, 2017). The optical depth scale at 5000 Å (500 nm), abbreviated $\log \tau_{500}$, is used to stratify atmospheric parameters.

We have inverted the Stokes I and V profiles of the Ca II 8542 Å, Si I 8536 Å and Fe I 8538 Å lines simultaneously to infer the stratification of temperature (T), LOS velocity (V_{LOS}), microturbulence (V_{turb}) and LOS magnetic field (B_{LOS}). We used a 6-level Ca II atom. The Ca II H&K profiles were modeled in PRD (Milkey and Mihalas, 1974; Uitenbroek, 1989), and Ca II IR lines were synthesized in complete re-distribution (CRD) approximation. The atomic parameters of the Si I 8536 Å and Fe I 8538 Å lines were obtained from the Vienna Atomic Line Database (VALD3) (Ryabchikova et al., 2015), and Kurucz's line lists (Kurucz, 2011), respectively and synthesized under LTE approximation. The upper level of the Si I 8536 Å transition was treated with J_1-l (JK) coupling scheme as described in appendix A.2. The latest version of the STiC inversion code has been upgraded to allow for the treatment of atomic levels of Kurucz's lines in JK coupling. An empirical log gf value of -1.4 was used for the Fe I 8538 Å transition (Socas-Navarro, 2007).

We used the k-means clustering to group the Stokes I profiles in different clusters such that similar-shaped profiles were grouped in one cluster. We then inverted the mean profile of each of those clusters to derive the stratification of T, V_{LOS}, and V_{turb}. Finally, the inferred stratification was used as the initial guess atmosphere to infer the stratification of the atmospheric parameters of the FOV, similar to the approach used by Nóbrega-Siverio, Guglielmino, and Sainz Dalda (2021) and Mathur et al. (2022b). In the second cycle, we used the values of B_{LOS} derived from the ME inversions from the Fe I 6569 Å line and WFA of the Ca II 8542 Å line as the guess values of the B_{LOS} at $\log \tau_{500} = -1$ and -4.5, respectively. Earlier studies have found that the Stokes V profiles of the Ca II 8542 Å line have maximum response to the perturbations in the B_{LOS} between $\log \tau_{500} = -4$ and -5 (Quintero Noda et al., 2016b; Joshi and de la Cruz Rodríguez, 2018; Murabito et al., 2019). Table 2.2 describes the node positions used for different categories of profiles. Quiescent profiles are nominal absorption profiles (910 profiles), and emission profiles are profiles that have an emission (or a hint of emission) in either blue or red or both the wings of the Ca II 8542 Å line (110 profiles). The quality of inversion fits are discussed in appendix A.3.

We set the average velocity in the pore region in the photosphere ($\log \tau_{500}$ range of $[-1, 0]$) to rest for the absolute velocity calibration. With respect to the average profile in the pore, the quiet-Sun profile is blue-shifted, that is, after velocity calibration, the V_{LOS} stratification inferred from the quiet-Sun profile shows an upflow of about -3 km s^{-1}.

2.4 Results and discussion

2.4.1 Results from the WFA and ME inversions

The B_{LOS} map inferred from the ME inversion of Stokes I and V profiles of Fe I 6569 Å line is shown in panel (f) of Fig. 2.1. The maximum B_{LOS} strength found is +800 G. The panel (e) of Fig. 2.1 shows the B_{LOS} map inferred from WFA applied on the Ca II 8542 Å within the wavelength range of $\lambda_0 \pm 0.25$ Å and the maximum B_{LOS} field strength found is +600 G. The region in the photosphere with opposite polarity of the B_{LOS} with respect to the pore has a field strength of about -200 G which is absent in the chromospheric B_{LOS} map.

2.4.2 Non-LTE inversion results

In this section we discuss about the results from the inversion of Stokes I and V profiles of the Ca II 8542 Å, Si I 8536 Å and Fe I 8538 Å lines using the STiC inversion code.

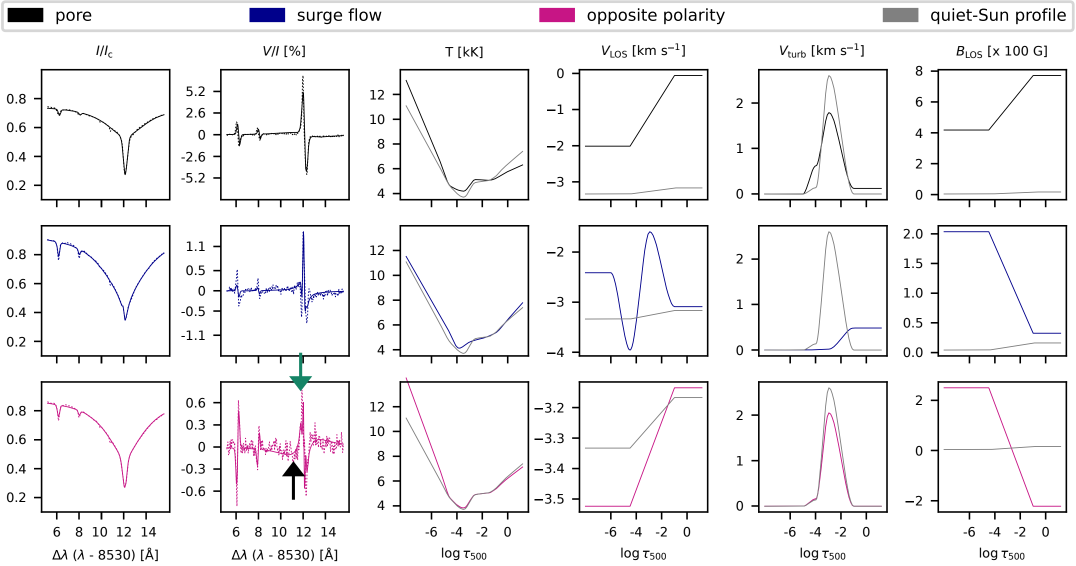

Figure 2.5: Inversion results of a few average profiles from different regions of the FOV. The dotted and dashed curves in the first two columns show the observed and fitted Stokes I and V profiles, respectively. The next three columns show the stratification of the T, $V_{\rm LOS}$, $V_{\rm turb}$ and $B_{\rm LOS}$ inferred from the inversions. The gray-colored curve shows the stratification of atmospheric parameters inferred from the inversions of an average quiet-Sun profile. The black and green arrows indicate the wavelength position in the wing and near the core of the Ca II 8542 Å line, respectively.

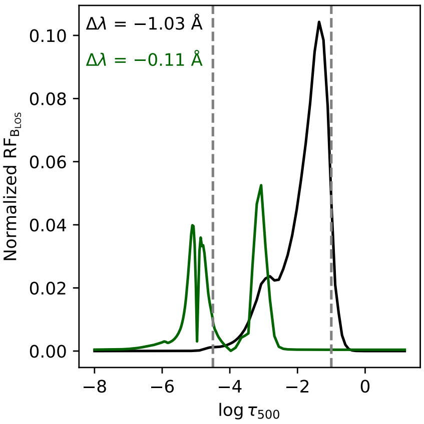

Figure 2.6: Normalized response function to the perturbations in the $B_{\rm LOS}$ at the wavelength positions $\Delta\lambda = -1.03$ and -0.11 Å (marked by black and green arrows in Fig. 2.5) from the Ca II 8542 Å line core. The node positions for the $B_{\rm LOS}$ used in the inversions are represented by the vertical dashed gray lines.

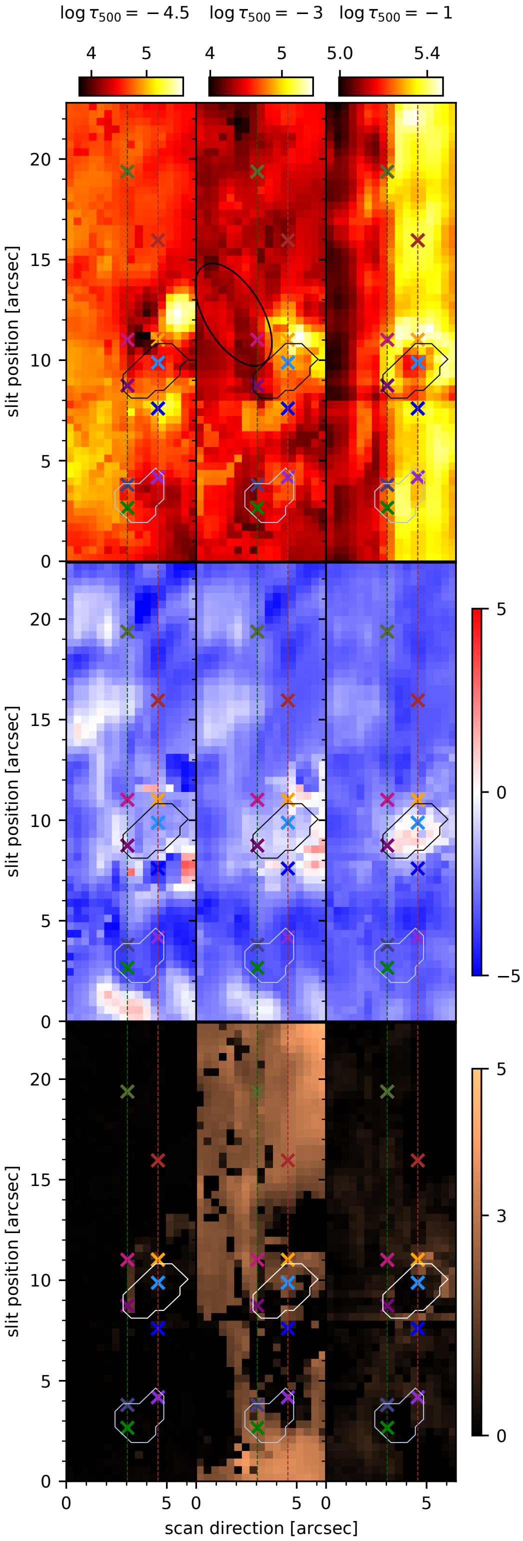

Figure 2.7: Maps of T, V_{LOS} and V_{turb} (row-wise) at $\log\tau_{500} = -4.5, -3, -1$ (column-wise) inferred from the inversions of the FOV. The contours, similar to Fig. 2.1, show the location of the pore and the opposite polarity region. The slanted elliptical contour in the middle panel of the T maps show the location of the dark fibrillar region seen in the panel (d) of Fig. 2.1.

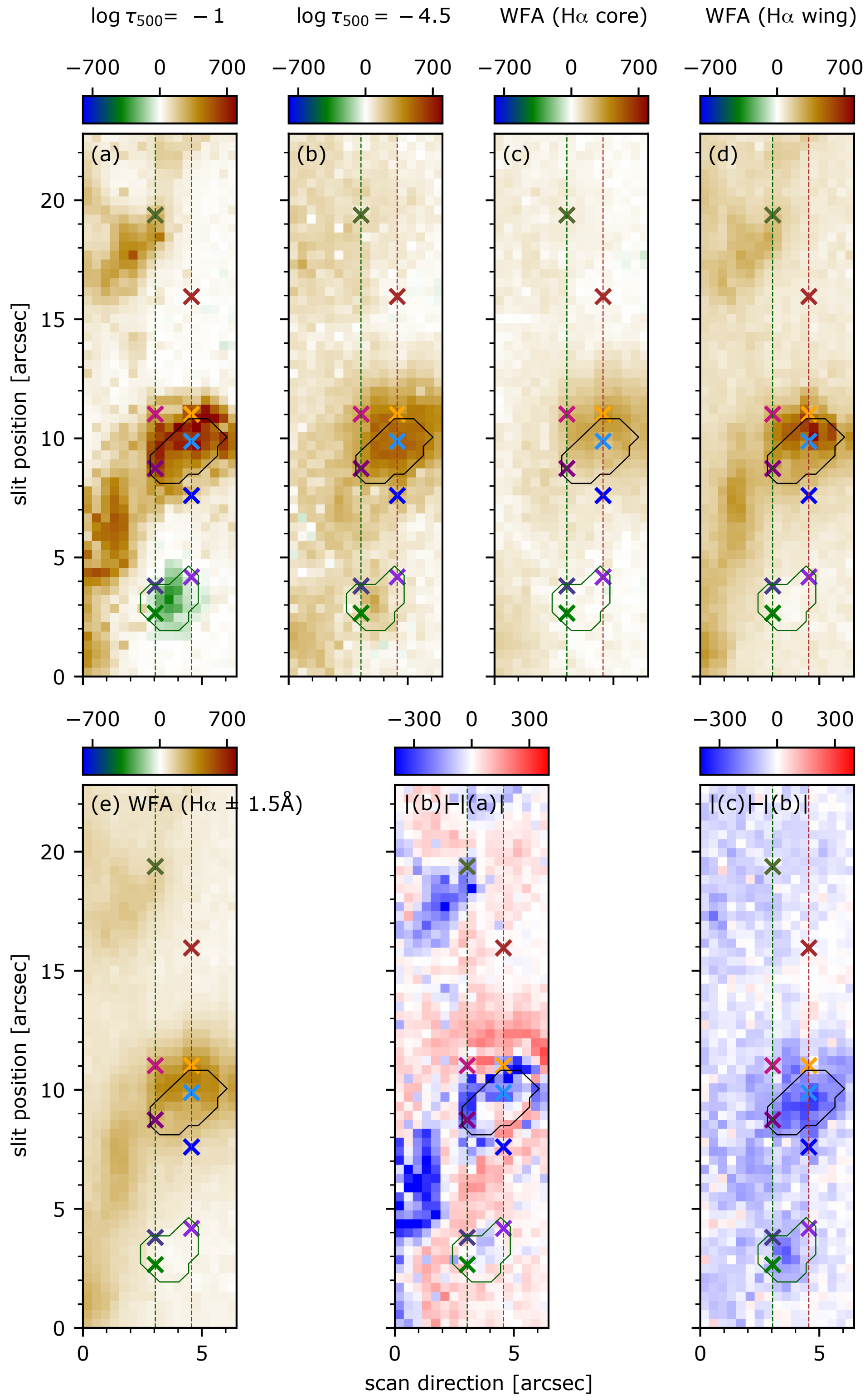

Figure 2.8: Maps of the B_{LOS} inferred from the inversions and the WFA. Panels (a) and (b) show the maps of B_{LOS} at $\log\tau_{500} = -1$ and -4.5, respectively. Panel (c) show the B_{LOS} inferred from the WFA of Hα spectral line in the spectral range ± 0.35 Å, panel (d) show the WFA inferred from the wings of Hα spectral line in the range $[-1.5, -0.6]$ and $[+0.6, +1.5]$ Å, and panel (e) show the map of B_{LOS} from WFA inferred from H$\alpha \pm 1.5$ Å. Change in the stratification of $|B_{\mathrm{LOS}}|$ is shown in the rightmost two panels of the bottom row as indicated on each panel. The black and green contours show the location of the pore and opposite polarity region, respectively.

In Fig. 2.5 we show inversion results of profiles averaged (to increase SNR) from a 3×3 box about the selected regions of the FOV, viz., pore, surge flow, and region with opposite polarity of the magnetic field. The average profile for the pore is calculated by averaging the pixels about the darkest pixel in the pore, for the surge flow profile by averaging about the blue-colored profile in Fig. 2.2 and for the opposite polarity profile by averaging about the green colored profile in Fig. 2.3.

The T stratification inferred from the pore profile has lower value of T at the photospheric layers ($\log\tau_{500}\sim-1$) and higher values at the chromospheric layers ($\log\tau_{500}\leq-4$) compared to that inferred from the inversion of the quiet-Sun profile. The V_{LOS} at photospheric layers ($\log\tau_{500}\sim-1$) is zero (calibrated) and at the chromospheric layers ($\log\tau_{500}=-4.5$) show upflow of about -2 km s^{-1}. The V_{turb} is non-zero between $\log\tau_{500}=-1$ and -4. The value of B_{LOS} at the photospheric and chromospheric layers is about +800 G and +400 G, respectively.

The reversal of the sign of the Stokes V profile of the Ca II 8542 Å line shown in Fig. 2.5 corresponding to surge flow region is a result of emission feature in the blue wing of the Ca II 8542 Å line and is not an indication of any change in polarity of the B_{LOS}. Accordingly the T show enhancement of about 600 K compared to T inferred from the quiet-Sun profile at $\log\tau_{500}=-4.5$ simultaneous with an upflow of about -4 km s^{-1}. For the pixels having spectral profiles similar to the surge flow, i.e., an emission feature in the blue wing and a red excursion in the Stokes I, the V_{turb} is small at all depth positions of $\log\tau_{500}$. It may be possible that such low values of V_{turb} may have some contribution in the higher temperature values inferred for the pixels in the surge flow region. Díaz Baso, Asensio Ramos, and de la Cruz Rodríguez (2022) have shown that there is a degeneracy between the T and the V_{turb}. When the spectral profiles are in emission, the T and V_{turb} are anti-correlated; that is, an increase in T broadens the spectral line, and thus to maintain the same width, the V_{turb} must be decreased. However, the enhancement in T and minimal values of V_{turb} are necessary to achieve a satisfactory fit of the emission feature (for more discussion see Mathur et al., 2022b). The value of B_{LOS} at the photospheric and chromospheric layers is about +50 G and +200 G, respectively. The reason for the increased value of the magnetic field in the chromosphere compared to the photosphere is because the line core of the Ca II 8542 Å line is sampling the canopy fields overlying the pore and the nearby opposite polarity region.

The T, V_{LOS} and V_{turb} stratification inferred from the opposite polarity profile is similar to that inferred from the quiet-Sun profile. The value of B_{LOS} at the photospheric and chromospheric layers is about -220 G and +250 G, respectively, again suggesting a canopy structure.

As described in section 2.2, above the positive polarity region, the sign of the Stokes V profile in the wings of the Ca II 8542 Å and Hα lines is opposite to that of in the core. This is probably because the line cores of the Hα and Ca II 8542 Å lines are sampling the canopy fields overlying the opposite polarity region. To verify that the wings and the core of the Ca II 8542 Å line are indeed sampling different layers of the atmosphere, in Fig. 2.6 we show the response to perturbations of the B_{LOS} at one wavelength position in the wing ($\Delta\lambda = -1.03$ Å) and another one in the core ($\Delta\lambda = -0.11$ Å) of the line where the sign of the Stokes V is opposite. Beckers and Milkey (1975) define the response function (RF) for a physical parameter X as $RF_X(\tau, \lambda) = \delta I(\lambda)/\delta X(\tau)$. Response functions contain information on how the Stokes parameters at different wavelength positions are sensitive to perturbations of a physical parameter at different $\log \tau_{500}$. The response function in the line wing of the Ca II 8542 Å line shows a dominant contribution of the photospheric fields ($\log \tau_{500} \simeq -1.5$), in contrast, the response function near the line core shows a dominant contribution of the chromospheric fields ($\log \tau_{500} \leq -3$).

The maps of T, V_{LOS} and V_{turb} inferred from the inversions of the FOV at $\log \tau_{500} = -4.5$, -3 and -1 are presented in Fig. 2.7. The morphological structure of the T map at $\log \tau_{500} = -1$ is similar to the far wing image of the Ca II 8542 Å line (see panel (a) of Fig. 2.1) with a decrease in T of about 300 K in the pore compared to surrounding background. There is a weak downflowing (+2 km s^{-1}) region near (x, y) = ($3''.5$, $8''.8$) while the rest of the pore does not show any signature of plasma flows. The value of V_{turb} is about 0–1 km s^{-1} in the V_{turb} maps at $\log \tau_{500} = -1$ except at a few regions where the V_{turb} is about 2–3 km s^{-1} such as the pore boundary ($6''$, $10''.8$).

The T at $\log \tau_{500} = -3$ ranges from 4–5.5 kK with a region of higher temperature ($T \sim$5.4 kK) seen near the pore boundary ($6''$, $10''.8$). The temperature near the negative polarity region (in ME B_{LOS} map) is about 4.2 kK. The dark fibril-like lanes starting at ($2''$, $8''.8$), indicated by the ellipse-shaped contour in Fig. 2.7, can also be seen in the Hα line core image (see panel (d) of Fig. 2.1). The majority of the pore region show upflows of up to -3 km s^{-1}. The V_{turb} inside the pore is about 0–3 km s^{-1} and outside the pore is about 3–5 km s^{-1}.

The morphological structure of the T map at $\log \tau_{500} = -4.5$ looks similar to the Ca II 8542 Å line core image (see panel (c) of Fig. 2.1). The brightest and darkest pixels in panel(c) of Fig. 2.1 correspond to T of about 5.7 kK and 3.8 kK, respectively. In general, the FOV show upflows of up to -3 km s^{-1} with two small regions showing downflows of about +2 km s^{-1}. The strong upflows up to -5 km s^{-1} are located in regions of higher temperature. There is almost zero V_{turb} in the V_{turb} map in all regions of the FOV.

The panels (a) and (b) of Fig. 2.8 show maps of the magnetic field at $\log \tau_{500} = -1$ and -4.5. The change in the stratification of $|B_{\mathrm{LOS}}|$ inferred from inversions is shown in the middle panel of the bottom row of Fig. 2.8. The morphological structure of the B_{LOS} map at the photospheric layers (at $\log \tau_{500} = -1$, panel (a) of Fig. 2.8) is similar to panel (e) of Fig. 2.1 with strong positive polarity in the pore ($\sim$ +800 G) and nearby regions ($\sim +350$ G). An opposite polarity with a magnitude of ~ -200 G is seen in the $B_{\rm LOS}$ map. The field at $\log\tau_{500} = -4.5$ has positive polarity with a maximum $B_{\rm LOS}$ of $\sim +600$ G in the pore and about $\sim +300$ G in the opposite polarity region. In general, the structure of the $B_{\rm LOS}$ at $\log\tau_{500} = -4.5$ is more spread out compared to that of at $\log\tau_{500} = -1$ (see panel (b) of Fig. 2.8). In addition, in the regions outside of the pore the $B_{\rm LOS}$ strength at $\log\tau_{500} = -4.5$ has increased compared to that at $\log\tau_{500} = -1$, suggesting a magnetic canopy-like structure (see middle panel in the bottom row of Fig. 2.8). Using multiple spectral lines, the magnetic canopies around pores have also been reported by many authors in the recent literature (for eg. Stauffer, Reardon, and Penn, 2022; Tapia and Bellot Rubio, 2022; Buehler et al., 2019; Murabito et al., 2016; Shimizu, Ichimoto, and Suematsu, 2012; Keppens and Martinez Pillet, 1996). The magnetic field strengths inferred at $\log\tau_{500} = -1$ (the photosphere) and $\log\tau_{500} = -4.5$ (the chromosphere) are comparable with the values reported by many authors in recent literature, who studied the stratification of $B_{\rm LOS}$ in pore using spectral lines of the Fe I atom, and Ca II 8542 Å and He I 10830 Å lines (Sowmya et al., 2022; Nagaraju, Sankarasubramanian, and Rangarajan, 2020a; Yadav et al., 2019; Quintero Noda et al., 2016a; Jurčák et al., 2015; Sobotka et al., 2013; Criscuoli et al., 2012).

2.4.3 Comparison of $B_{\rm LOS}$ inferred from the Ca ii 8542 Å and Hα lines

The panels (c), (d) and (e) of Fig. 2.8 show maps of the magnetic field inferred from the WFA method applied to the Stokes I and V profiles of the Hα line. The difference in amplitude of the $|B_{\rm LOS}|$ inferred from the Hα line with that of inferred from the inversions is shown in the two rightmost panels of the bottom row of Fig. 2.8. Figure 2.9 shows the scatter plots between the $|B_{\rm LOS}|$ inferred from inversions and the WFA.

The field strengths inferred from inversions of the Ca II 8542 Å line at $\log\tau_{500} = -4.5$ are comparable to those of inferred from the WFA of the Ca II 8542 Å line (see panel (a) of Fig. 2.9), suggesting consistency between the two methods in inferring the $B_{\rm LOS}$. The magnetic field map inferred from the WFA of the Hα line core (Hα ±0.35 Å) has a similar morphological structure to the map inferred from inversions of Ca II 8542 Å line at $\log\tau_{500} = -4.5$ (see panels (b) and (c) of Fig. 2.8) suggesting the Hα line core probes the chromospheric magnetic field. The $B_{\rm LOS}$ field strength inferred from WFA of Hα line core is almost half (0.53 times) of that of inferred from inversions at $\log\tau_{500} = -4.5$ and the WFA of the Ca II 8542 Å line (see the rightmost panel in the bottom row of Fig. 2.8 and panel (b) and (c) of Fig. 2.9). This could be due to sensitivity of the core of the Hα line to the magnetic field in the higher atmospheric layers than that of Ca II 8542 Å line. Or due to systematic underestimation of $B_{\rm LOS}$ using the WFA from the Hα line. A detailed analysis of the Hα

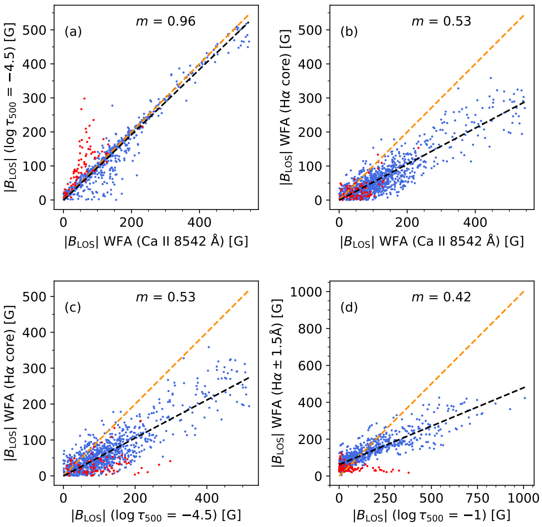

Figure 2.9: Comparison of the magnitude of B_{LOS} inferred from inversions and the WFA. The red and blue colors represent the pixels at photospheric layers with negative and positive polarity of the B_{LOS}, respectively. Panel (a) shows the comparison between the B_{LOS} inferred at $\log\tau_{500} = -4.5$ with that inferred from WFA on the Ca II 8542 Å line. Panels (b) and (c) show the comparison between the B_{LOS} inferred by applying the WFA on the Hα line core with the B_{LOS} inferred from the WFA on Ca II 8542 Å line and at $\log\tau_{500} = -4.5$, respectively. Panel (d) show comparison between the B_{LOS} inferred by applying the WFA on the Hα ±1.5 Å with B_{LOS} at $\log\tau_{500} = -1$. The black colored line shows the linear fit whose slope is indicated by m. The fiducial line is shown in yellow color for comparison.

Stokes I and V profiles synthesized using current state-of-the-art model atmospheres of active regions and quiet Sun, taking into account the fine-structure sub-levels (nlj) of the atomic levels (n), 3D radiative transfer and the Zeeman effect, is required.

The maps of B_{LOS} inferred from the WFA method on the wings and the full spectral range of the Hα line show a morphological structure similar to that of $\log\tau_{500} = -1$ (see panel (d) and (e) of Fig. 2.8), suggesting a significant contribution from the photospheric fields. However, the negative polarity region is not clearly seen. This is because, as explained in section 2.2, there are very few spectral pixels with a clear signal of opposite sign in Stokes V profile in the line core and wings of the Hα line. The negative polarity region is very well reproduced through inversions because of good signal in Stokes V profiles of the Si I 8536 Å and Fe I 8538 Å lines. The $|B_{\text{LOS}}|$ inferred from the full spectral range of the Hα line is weaker by a factor of 0.42 than that of B_{LOS} at $\log\tau_{500} = -1$, which is consistent with previous studies (see panel (d) of the Fig. 2.9) (Abdussamatov, 1971; Balasubramaniam, Christopoulou, and Uitenbroek, 2004; Hanaoka, 2005; Nagaraju, Sankarasubramanian, and Rangarajan, 2008).

The above comparison of B_{LOS} inferred from the Hα and the Ca II 8542 Å lines suggest that the line core of the Hα line is sensitive to the chromospheric magnetic fields while the wings and the full Hα line exhibit significant sensitivity to the photospheric magnetic fields.

2.5 Conclusions

In this paper, we presented an analysis of spectropolarimetric observations recorded simultaneously in the Hα and Ca II 8542 Å lines of a pore with positive magnetic polarity, as well as the surrounding region that covers also a negative polarity magnetic field region. This is towards the goal of exploring the diagnostic potential of the Hα line to probe the chromospheric magnetic field. To estimate $B_{\rm LOS}$ field from the Hα line we have used the WFA, and from Ca II 8542 Å line we have used both the WFA and inversion methods. The similarity between the magnetic field morphology inferred by applying the WFA on the core of the Hα and Ca II 8542 Å lines and inferred from inversions at $\log \tau_{500} = -4.5$ is a clear evidence that the Hα line core probes the chromospheric magnetic field. This evidence is even more striking in the region above the negative polarity region in which the Hα and Ca II 8542 Å line cores exhibit positive polarity where as the line wings exhibit negative polarity. This is because of the canopy fields from the dominant positive polarity region extended at the chromospheric heights overlying above the negative polarity region, which is mostly confined to photospheric heights. It is found from the quantitative comparison that $B_{\rm LOS}$ fields estimated from the Hα line core are about ≈ 0.53 times that of estimated from the Ca II 8542 Å line core. This may suggest that the magnetic sensitivity of the Hα line core is located in the higher layers in the solar atmosphere than that of the Ca II 8542 Å line core. However, there is a possibility that $B_{\rm LOS}$ values are systematically underestimated from the Hα line under WFA. Further investigation through multi-line spectropolarimetric observations and 3D radiative transfer calculations are required to fully understand the diagnostic potential of the Hα line to probe the chromospheric magnetic field.

Chapter 3

An image autoguider system for the Kodaikanal Tower Tunnel Telescope

An image autoguider system for the Kodaikanal Tower Tunnel Telescope
Harsh Mathur, K. C. Thulasidharen, Hemanth Pruthvi, K. Nagaraju, and M. Rajalingam, 2023, **Journal of Astronomical Instrumentation**, Volume 12, Issue 2, id. 2350003-222.

In the previous chapter, we presented a comparison of the stratification of line-of-sight magnetic field values inferred from the non-LTE inversions of the Ca II 8542 Å line with that of inferred from the WFA over the Hα line. This was done to explore whether the Stokes V profiles of the Hα line probe the chromospheric magnetic field. Our analysis suggested that the line core of the Hα line indeed probes the chromospheric magnetic field. However, either the Hα line probes higher heights of the solar atmosphere compared to the Ca II 8542 Å line or the field strengths from the Hα line are underestimated. Thus, further simultaneous spectropolarimetric observations of the Hα and Ca II 8542 Å lines are necessary to investigate the diagnostic potential of the Hα line. In this context, we planned to upgrade the Kodaikanal Tower Tunnel Telescope to allow for recording of simultaneous spectropolarimetric observations with an operational tip-tilt system. However, before a tip-tilt system can be operational, an image autoguider system that tracks the Sun's image is necessary as a precursor. This is because there is an inherent image drift is present in the KTT, due to which potential tip-tilt systems can only work for a limited time. The image drift causes the tip-tilt mirror to move outside of nominal angles and thus halting the tip-tilt correction system. The contents of the study, Mathur et al. (2022a), describing the development, testing, and installation of an image autoguider system for the KTT, are reproduced in its entirety in this chapter.

3.1 Introduction

The Kodaikanal Tower Tunnel Telescope (Bappu, 1967) system has a 3-mirror (60 cm aperture) Coelostat placed in the tower as a light feeding system. The primary mirror (M1) of the Coelostat tracks the Sun at a constant speed (15 degree hour^{-1}) with the help of an Alternating Current (AC) motor running at a nominal frequency of 47.25 Hz, and the secondary mirror (M2) guides the light vertically down. This beam is fed into the horizontal tunnel by a fold mirror (M3) with 45° orientation. M3 directs the beam onto an air-spaced doublet lens (L1, 38 cm aperture, f/96) which focuses the Sun's image at a distance of 36 m with an image plate scale of 5.5 arcsec mm^{-1}. A Littrow-mount slit-spectrograph is the main instrument of the telescope installed at the telescope focal plane with a 20 cm diameter and 18 m focal length achromat with a 600 lines mm^{-1} grating with the theoretical resolving power of $\sim$ 240000 in the second-order diffraction spectrum.

The KTT spectrograph has been used for recording Ca II K spectra (Bagare, 1985; Sivaraman et al., 1993; Sivaraman, Gupta, and Kariyappa, 1993, 1996), the Zeeman spectra in Fe I 6302.5 Å, and line of sight velocity in opposite polarity sunspots (Bagare and Gupta, 1998; Sundara Raman, Aleem, and Thiagarajan, 1999). The telescope has also been used to measure vector magnetic field of sunspots and active regions using a Stokes polarimeter (Sankarasubramanian, Rangarajan, and Ramesh, 2002; Nagaraju, Sankarasubramanian, and Rangarajan, 2008, 2020b). Recently, a dual beam polarimeter with an integrated scanning unit is installed at KTT (Pruthvi et al., 2018) which can be used to scan over a field-of-view by moving image over the spectrograph slit. The polarimeter can also work in sit and stare mode. There are also plans to upgrade the telescope with an additional camera to make simultaneous multi-line spectropolarimetric observaions. However, like any other ground based telescope, KTT is also affected by the atmospheric turbulence or seeing, which causes random image aberrations that affect the spatial resolution and induce spurious polarization, thus rendering high-precision polarimetry with high spatial resolution difficult (Lites, 1987; Judge et al., 2004; Krishnappa and Feller, 2012). Hence, it is essential to employ systems like tip-tilt and higher-order adaptive optics (Rimmele and Marino, 2011) to correct for seeing induced motions.

The Coelostat is an equatorial mount which must be aligned such that the polar axis has altitude equal to latitude of the place and must be parallel to the local longitude. However, a few arcsecond misalignments will cause an image drift in East-West (E-W) and North-South (N-S) axes. The image drifts measured at KTT are variable with time with maximum recorded value of about $\sim$ 7 arcsec minute^{-1} close to noon (see appendix B.1). Due to this drift, potential tip-tilt systems can only work for a limited time due to the limit of the stroke of the actuator. The image drift causes the tip-tilt mirror to move outside of nominal angles and thus halting the tip-tilt correction system. Hence, as a precursor to arrest seeing induced motions through systems like tip-tilt systems, an image Auto Guider system is necessary.

Different telescopes arrest image drifts in different ways. For example a Guider Telescope and quad-cell is used to arrest image drift in the Big Bear Telescope (Varsik and Yang, 2006). The guider operates by focusing a small filtered white light image on the quad cell mounted on an X-Y stage with axes oriented parallel to East-West (E-W) and North-South (N-S) directions. The solar image generates an X and Y error signal based on the difference in brightness in E-W and N-S directions, which depends on the offset of the solar image in the guider from the center of the cell. The Multi-Application Solar Telescope (MAST) uses a Guider Telescope and a charge coupled device (CCD) to arrest the image drift (Denis et al., 2008) in the image plane. The guider telescope focuses the full disk image of the Sun on the CCD and tracks the centroid of the solar image. The Swedish Solar Telescope and the Gregor Telescope use tip-tilt mirror and a correlation tracker CCD (Scharmer et al., 2003; Kleint, Lucia et al., 2020) for pointing and tracking. The correlation CCD operates at typically high frequencies (>900 Hz) with a fast piezo-controlled tip-tilt mirror to compensate for any seeing related image motions. The computer controlling the tip-tilt mirror calculates averages of the voltages applied to the piezo over a few second intervals (10–15 s) and sends correction to telescope pointing system to ensure tip-tilt mirror operates close to nominal angles.

This paper presents development, installation and testing of Auto Guider System at the KTT. The instrumentation, working principle, operation and calibration procedures are discussed in section 3.2, the testing and characterization are presented in section 3.3, and finally, the conclusions are presented in section 3.4.

3.2 Auto Guider System at KTT

3.2.1 Working Principle

Image movement along the E-W and N-S directions on the image plane at KTT is mainly achieved by tilting the second mirror M2 of the Coelostat. M2 is attached with a Direct Current (DC) stepper motor in each direction (E-W and N-S) that tilts the mirror while the motor is rotated. We make use of this system to correct for image drift. We track image motion by sensing the position of the image's limb using a sensor (which is composed of two segment photodiode) in each direction. The photodiode in each direction is positioned such that the image's limb falls approximately on the middle of the outer segment (see panel (b) of Fig. 3.1). We take a differential voltage output from the two sensor segments in a single measurement, which reduces the effect of any intensity variations that are not due to image shift. Differential output also minimizes electrical signal readout noise while analog to digital voltage conversion.

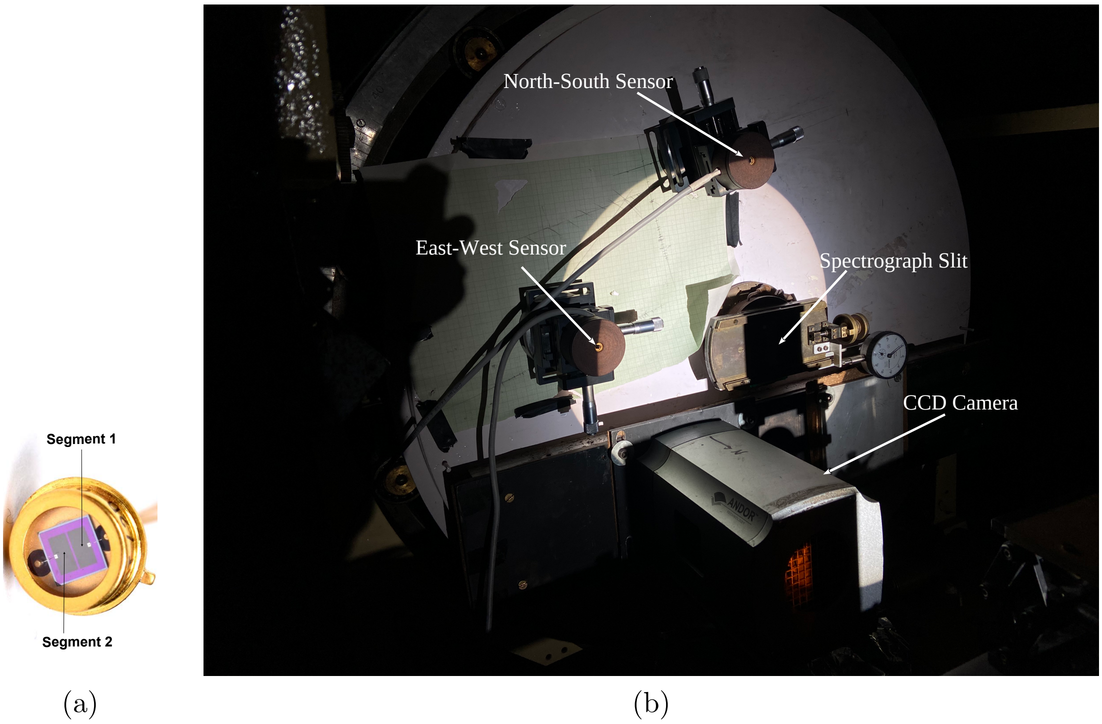

(a) (b)

Figure 3.1: The Auto Guider System installed at the KTT. Panel (a) shows a photodiode image showing the two segments. Panel (b) shows the Sun's image on the focal plane. Two SPOT-2D sensors are positioned at the north and east limb, respectively. The image motion on the image plane is tracked by the sensors by sensing the position of the image limb. The image drift is arrested in real-time by tilting the mirror M2 through real-time feedback to the motors of the mirror M2 (not shown in the figure). The CCD camera is not a part of the Auto Guider system.

The difference signal (voltage) represents the degree of illumination of the outer segment with respect to inner segment of a sensor which is proportional to the position of image limb on the outer segment of the sensor and hence on the image plane. This difference signal (voltage) is calibrated against the image shift, which in turn is calibrated against the electrical voltage pulses to drive the DC stepper motors of the second mirror M2. The DC motors receive real-time feedback according to the differential voltage measured by each photodiode and correct the image position by tilting the second mirror in E-W and N-S direction, thus arresting image drift. A schematic of the Auto Guider system is shown in Fig. 3.2.

3.2.2 Instrumental Setup

We sense Solar East and North limb using a Segmented Photodiode (SPOT-2D*) sensor in each direction (E-W and N-S) (shown in panel (a) of Fig. 3.1). Each SPOT-

---

*http://www.osioptoelectronics.com/Libraries/Datasheets/Segmented-Photodiodes.sflb.ashx

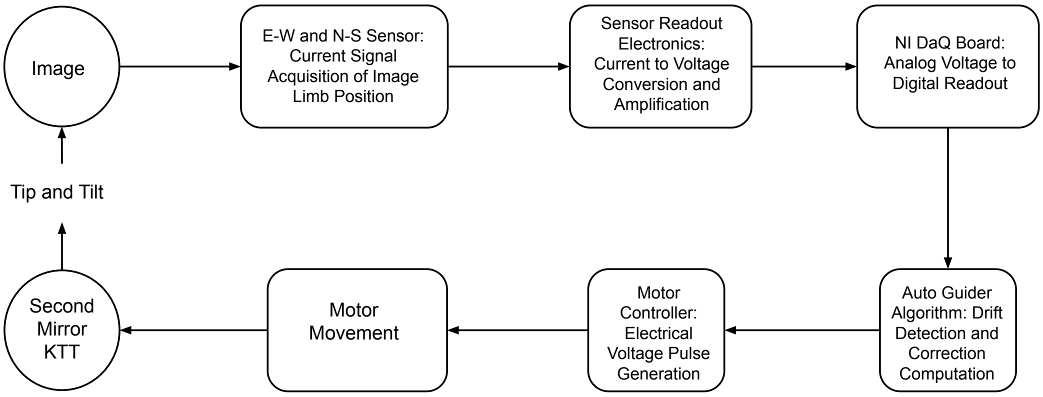

Figure 3.2: A Schematic of the Auto Guider System. The position of the image's limb is sensed using the orthogonally placed SPOT-2D sensors which provide a current signal, the readout electronics convert the current to voltage and amplify the signal. The computer reads the voltages, converted to digital by the NI DaQ board, and gives the motor controller appropriate feedback (counts). The motor controller generates electrical voltage pulses, which drive the E-W, and the N-S motors, which move the second mirror of the KTT, thus, moving the image on the image plane.

2D sensor is soldered on a printed circuit board (PCB) and then it is enclosed in a holder made of mica to prevent electronic interference. The mica holder is mounted on a linear X-Y stage which is attached to the image plane using a magnet as shown in panel (b) of Fig. 3.1. Each SPOT-2D sensor is composed of two segments, each with an area of 3.3 mm^2, dimensions 1.3 mm $\times$ 2.5 mm and gap between two segments 0.127 mm.

Each segment is a photodiode, that generates a current signal when they are illuminated by the light. The current signal from each segment of a sensor is given to readout electronics which converts it to voltage, then, amplifies the signal. The readout electronics consists of circuit made from LF 356[†] and OP27[‡] operational amplifiers from Texas Instruments, which converts the current signal to a voltage signal, an amplifier and a low pass filter (f_c < 10 Hz). The output from readout electronics for both segments of a sensor is connected to single channel analog input ('+' and '−') of a data acquisition card (NI USB-6351[§] board from National Instruments) to be converted to digital and a differential voltage is read by the computer for a sensor in each direction.

The second mirror M2 of the Coelostat of the KTT is installed with a DC stepper motor (model HS50 from Superior Electric) in each direction (E-W and N-S) controlled through a SLO-SYN stepper motor drive model SS2000D6 from Superior Electric. The motor controller is connected to a computer using a serial connection, and given text

---

[†] https://www.ti.com/product/LF356#product-details

[‡] https://www.ti.com/product/OP27

[§] https://www.ni.com/docs/en-US/bundle/pcie-usb-6351-specs/page/specs.html commands about the total number of electrical voltage pulses, hereafter referred to as counts, to generate. The motor controller then generates electrical voltage pulses that drive the motors of M2, which tilts the mirror, causing the image to move on the image plane.

3.2.3 Operation Procedure

We take 20 readings from each sensor in one second with a 50 ms cadence and average them to get one voltage sample per second. Each of the 20 readings is acquired in 0.16 ms and composed of 200 voltages sampled using the NI-USB 6351 analog input channel. Once voltages are sensed and averaged, correction voltage for each sensor is calculated through Proportional-Integral-Derivative (PID) control.

Let $E_\mathrm{x}(t)$ be the measured minus the reference voltage at time t for east sensor, then correction voltage $V_\mathrm{x}(t)$ is given by the equation 3.1 and similar equation follows for $E_\mathrm{y}(t)$ and $V_\mathrm{y}(t)$.

$$V_\mathrm{x}(t) = K_\mathrm{p} * E_\mathrm{x}(t) + K_\mathrm{i} * \int_0^t E_\mathrm{x}(t')\,dt' + K_\mathrm{d} * \frac{dE_\mathrm{x}}{dt} \tag{3.1}$$

where K_p, K_i and K_d are proportional, integral and derivative constants, respectively.

The correction voltages (V_x and V_y) are translated to the motor counts (C_x and C_y) following a linear relation given by equation 3.2, where A is the control matrix (derived from calibration procedure).

$$\begin{bmatrix} C_\mathrm{x} \\ C_\mathrm{y} \end{bmatrix} = \begin{bmatrix} A_{00} & A_{01} \\ A_{10} & A_{11} \end{bmatrix} * \begin{bmatrix} V_\mathrm{x} \\ V_\mathrm{y} \end{bmatrix} \tag{3.2}$$

3.2.4 Calibration Procedure

The image shift in voltages is related to the counts given to the motor following a linear relation given by equation 3.3, where S indicates calibration matrix (that is nothing but the inverse of control matrix).

$$\begin{bmatrix} V_\mathrm{x} \\ V_\mathrm{y} \end{bmatrix} = \begin{bmatrix} S_{00} & S_{01} \\ S_{10} & S_{11} \end{bmatrix} * \begin{bmatrix} C_\mathrm{x} \\ C_\mathrm{y} \end{bmatrix} \tag{3.3}$$

S is calculated by applying known counts to motors and measuring resulting voltages in sensors. This procedure is calibration and described in the following steps:

1. The image limb is positioned in the outer segment of each sensor.
2. Only C_x is applied and V_x and V_y are measured
3. Only C_y is applied and V_x and V_y are measured.

4. Four plots (V_{x} vs C_{x}, V_{y} vs C_{x}, V_{x} vs C_{y}, and V_{y} vs C_{y}) are obtained, and four lines are fitted to them. Slopes of these lines are elements of S.

Further, the calibration matrix S is inverted to get control matrix A that converts voltages to motor counts.

We carried out the calibration procedure by moving the image from left to right by giving counts to motor in E-W direction of M2 of Coelostat and recorded voltages in sensors in both directions (E-W and N-S) to estimate the relationship of V_{x} and V_{y} with C_{x}, and similarly moved image up to down to estimate the relationship of V_{x} and V_{y} with C_{y}. The relationship of applied counts vs voltages measured is presented in Fig. 3.3. From these measurements we calculated,

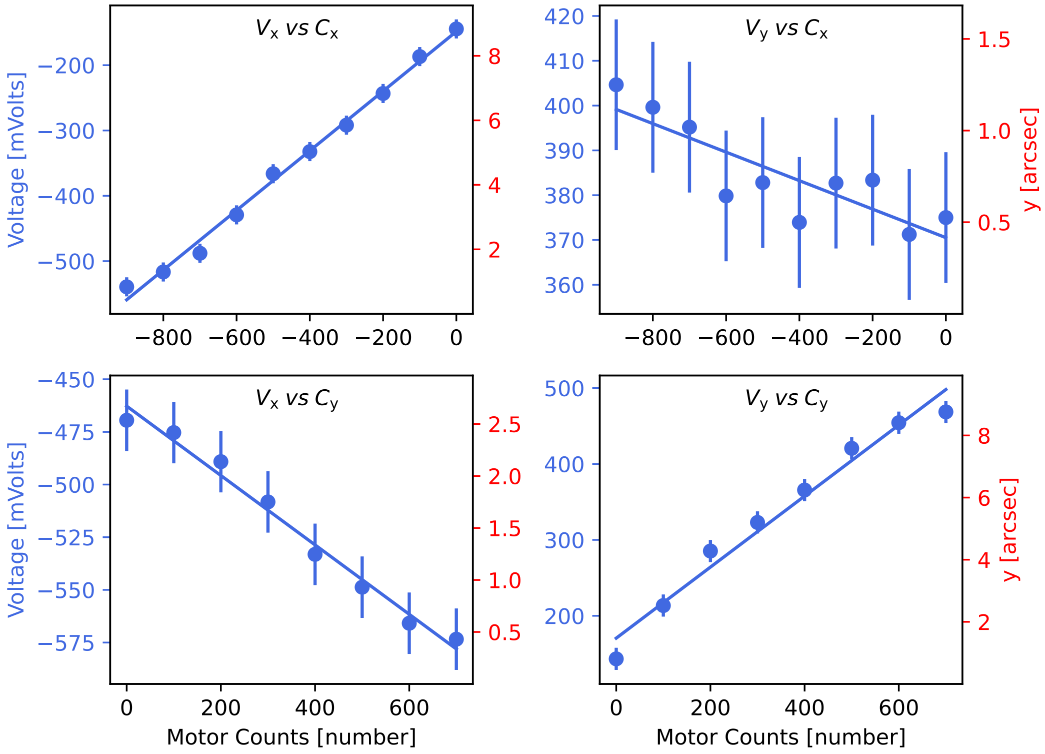

Figure 3.3: Plots of image shift in voltages versus motor counts, the slope of which are elements of calibration matrix. The sign of the x-axis indicates the direction of image motion while calibration. The image is moved from left to right while estimating the relationship of V_{x} and V_{y} with C_{x} and up to down for V_{x} and V_{y} with C_{y}.

$$S = \begin{bmatrix} 0.45 & -0.03 \\ -0.16 & 0.47 \end{bmatrix} \pm \begin{bmatrix} 0.015 & 0.015 \\ 0.018 & 0.018 \end{bmatrix} \tag{3.4}$$

$$A = \begin{bmatrix} 2.25 & 0.15 \\ 0.79 & 2.19 \end{bmatrix} \pm \begin{bmatrix} 0.101 & 0.078 \\ 0.141 & 0.110 \end{bmatrix} \tag{3.5}$$

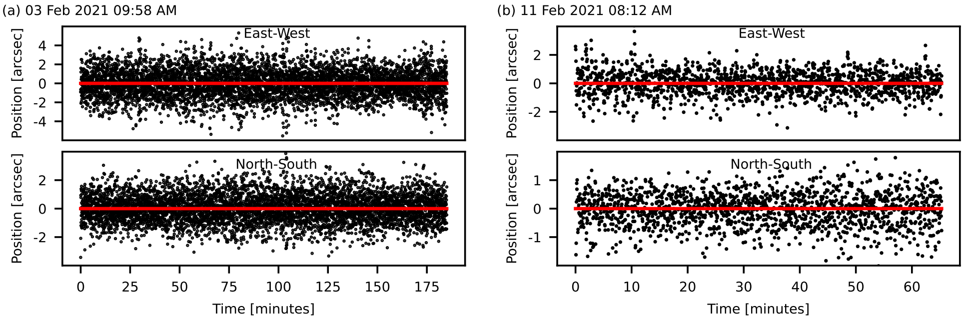

Figure 3.4: Image Limb position measured using photodiodes when Auto Guider was running in closed-loop with proportional controller.

The plots show linear relationship between counts to the motor and image motion (in voltage units). The non-zero off-diagonal elements of calibration and control matrix are because the movement of a circular Solar image in east-west direction shows movement in north-south direction and vice-versa. There is little movement in N-S direction when the image is moved in E-W direction and thus signal to noise ratio is low in V_{y} vs C_{x} relation. The maximum error in S is estimated by dividing measurement uncertainty (see appendix B.1) by total number of motor counts in x-axis. The error propagated in A through S (while calculating the inverse) is computed following the Monte-Carlo method. Using the distribution of values for the matrix elements of S inferred from the errors estimated, 10,000 matrices are chosen randomly. The inverse is computed for each of the 10,000 S matrices in order to compute the corresponding matrices A. The error propagated in A is the maximum value of the difference between each matrix element of A and the original values.

3.3 Testing of Auto Guider System

3.3.1 Observations

We used the control matrix derived from calibration to run the Auto Guider in closed-loop using proportional controller for long duration and present the image position measured using photodiodes in Fig. 3.4. The sky conditions were good and Auto Guider successfully arrested image drift and kept image position within $\pm \sim 1.5\,''$ (root mean squared value) from reference position This suggests that Auto Guider system is stable and can work for long duration to keep image positioned about a reference point.

3.3.2 Limit Tests

We attempted to test the capability of the system to derive the maximum value of image drift the system can correct for in closed-loop operation. We introduced artificial drifts in E-W direction by changing the tracking speed of the first mirror M1 of the Coelostat system of KTT which tracks the Sun from the default value of 15 degree hour^{-1}. This is achieved by changing the frequency of the motor of M1 from the default value of 47.25 Hz. If the frequency is greater than default, the M1 rotates faster than 15 degree hour^{-1} and image will appear to move towards left on image plane and vice-versa. We changed the frequency to the values listed in Table 3.1 and measured the image drift. These drifts were measured manually by marking image limb position on paper after every 1 minute for 5 minute duration. The maximum uncertainty in the drift measurement is estimated to be 0.100 mm minute^{-1} (0.550 arcsec minute^{-1}).

Table 3.1: Drift measurements in E-W direction at different tracking frequencies of motor of primary mirror M1 (manual measurements).

Frequency (Hz)	East-West Drift (arcsec minute^{-1})
46	22.88
49	26.13
44	55.00
48	10.45

Finally, we ran the Auto Guider in close-loop to arrest the resultant drifts and present the image position data (measured using photodiodes) in Fig. 3.5. At 46 Hz, the drift measured in E-W direction is 22.88 arcsec minute^{-1} and the scatter plot of image position seems fluctuating at an offset of about $\sim -1\,''$ from the reference position (see panel (a)). The image position data while arresting the drifts measured at frequencies 49 and 44 Hz shown in panels (b) and (c), respectively, show similar behaviour to panel (a) with offset in panel (b) ($\sim +1\,''$) in opposite direction to that of in panel (a) while panel (c) has a larger offset of $\sim -2\,''$ in the same direction from reference position. This can be explained by the fact that the direction of image drift at 49 Hz is opposite to that of at 44 and 46 Hz, because 49 Hz is higher than the nominal frequency of motor of M1 while 44 and 46 Hz are lower, and image drifts were fast enough that image drifted significantly before Auto Guider could lock the position, thus shifting the reference position at which Auto Guider kept image stable. For frequencies with higher drifts than 55 arcsec minute^{-1} (not shown), the Auto Guider system could not arrest the drift because the image quickly went out of the sensor before the system could lock the position. Hence, we suggest that the maximum image drift the Auto Guider system can arrest is 55 arcsec minute^{-1} . Panel (d) of Fig. 3.5 shows the image arrest data for frequency 48 Hz when the drift was 10.45 arcsec minute^{-1} in E-W direction which is comparable to maximum drift observed (7 arcsec minute^{-1} , see appendix B.1 for more details on drifts measurements) at nominal tracking speed of M1, and we found image drift was successfully arrested with a precision of $\sim 1.8\,''$ (root mean squared value).

Since the maximum drifts we encountered at nominal tracking speed of the first mirror M1 (15 degree hour^{-1}) are of the order of $\sim$ 7 arcsec minute^{-1} , the limit tests give us confidence on the image drift arrest capability of the Auto Guider system.

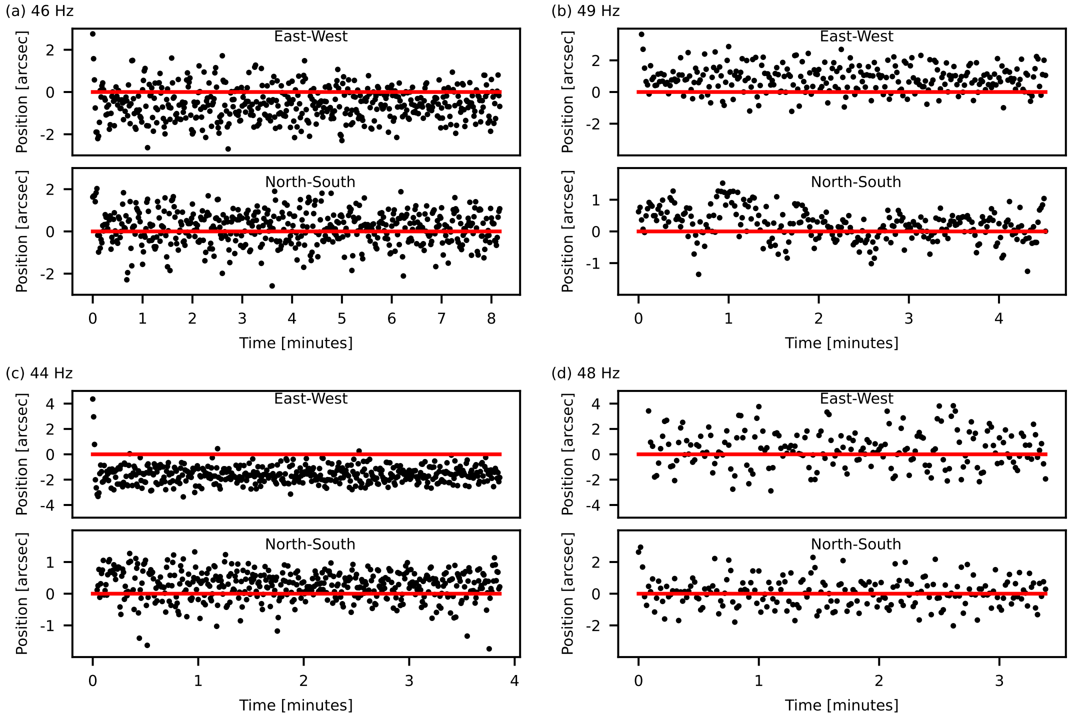

Figure 3.5: Image position measured using photodiodes when the Auto Guider System is running in closed-loop while arresting the drifts mentioned in Table 3.1

3.3.3 Characterization of Auto Guider System using a Fast sCMOS Camera

We have used the optical setup of the polarimeter (Pruthvi et al., 2018) at KTT to characterize the performance of the Auto Guider system using a scientific Complementary Metal–Oxide–Semiconductor (sCMOS) camera (C-Blue One from First Light Imaging) with a pixel size 9 μm. The light beam from the Coelostat after passing through the air-spaced doublet lens L1 (with f-number f/96) falls on a fold mirror to pass through a dichroic beam splitter (λ_c = 600 nm). The blue beam after passing through a polarising filter (to attenuate the intensity) and a visible filter centered about 500 nm (FWHM=50 nm) formed image on the detector as shown in panel (a) of Fig. 3.6.

We recorded short-exposure (maximum 5 ms) images of a sunspot present between 29th March to 3rd April 2022 and on 20th April 2022 with 0.5 second cadence. We estimated the image drift and the closed-loop system accuracy by measuring the

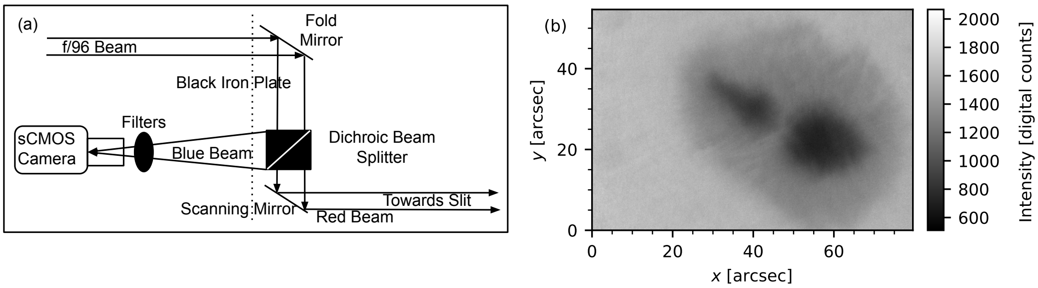

Figure 3.6: Experimental setup to record images of a Sunspot using a sCMOS camera. Panel (a): The f/96 beam falls on the fold mirror, then passes through a dichroic beam splitter ($\lambda_c = 600$ nm). The blue beam after passing through a polarising filter and a narrowband filter gets imaged at the detector. The red beam after passing through the scanning mirror, enters the slit of the spectrograph. The dotted vertical line shows the position of black iron plate which acts as light blocker. The X-Y linear stages holding the mica mount containing the photodiode sensor gets attached to the iron plate using a magnet. Panel (b): An image of a sunspot recorded using the setup.

image shift with the reference image (the first image of a given sequence). Panel (b) of Fig. 3.6 shows one snapshot of a sunspot image from the sCMOS camera setup.

We note that while the Auto Guider system is running in closed loop, random image fluctuations are seen about reference position (see panel (a) of Fig. 3.5). In addition, sometimes image oscillations are also seen (see image position in N-S direction in panel (b) of Fig. 3.5). These fluctuations can be as large as $\sim 4\,''$. Interestingly, random fluctuations of image position and oscillations about reference position are also observed when the Auto Guider System is not running, implying that random fluctuations and / or oscillations are present in addition to image drift. Figure 3.7 shows one such example with Auto Guider System off while image is drifting with image position measured using sCMOS camera setup. The maximum image drift measured between 08:15 AM and 08:52 AM on 20th April 2022 is $\sim 1.66 \pm 0.0003$ arcsec minute^{-1} and $\sim 0.50 \pm 0.0003$ arcsec minute^{-1} in E-W and N-S directions, respectively. Panel (a) of figure show clear oscillations about the image drift (red curve) in E-W direction while panel (b) shows random fluctuations about the drift in N-S direction. The Fourier spectrum shows significant power around periods of 40 and 70 s in E-W direction and 50, 65 and 80 s in N-S direction with relatively less power in N-S direction. These periods are much higher than seeing induced oscillations (Lites, 1987) (typically $\sim$ 2–3 ms). Thus, we suggest these fluctuations and oscillations of image position could be due to Coleostat system of the KTT and use of non-optimum PID control parameters.

Further, we proceeded to derive optimum PID control parameters to minimize image fluctuations and amplitude of image oscillations about reference position while using the Auto Guider System in closed-loop as described in following section 3.3.3.1.

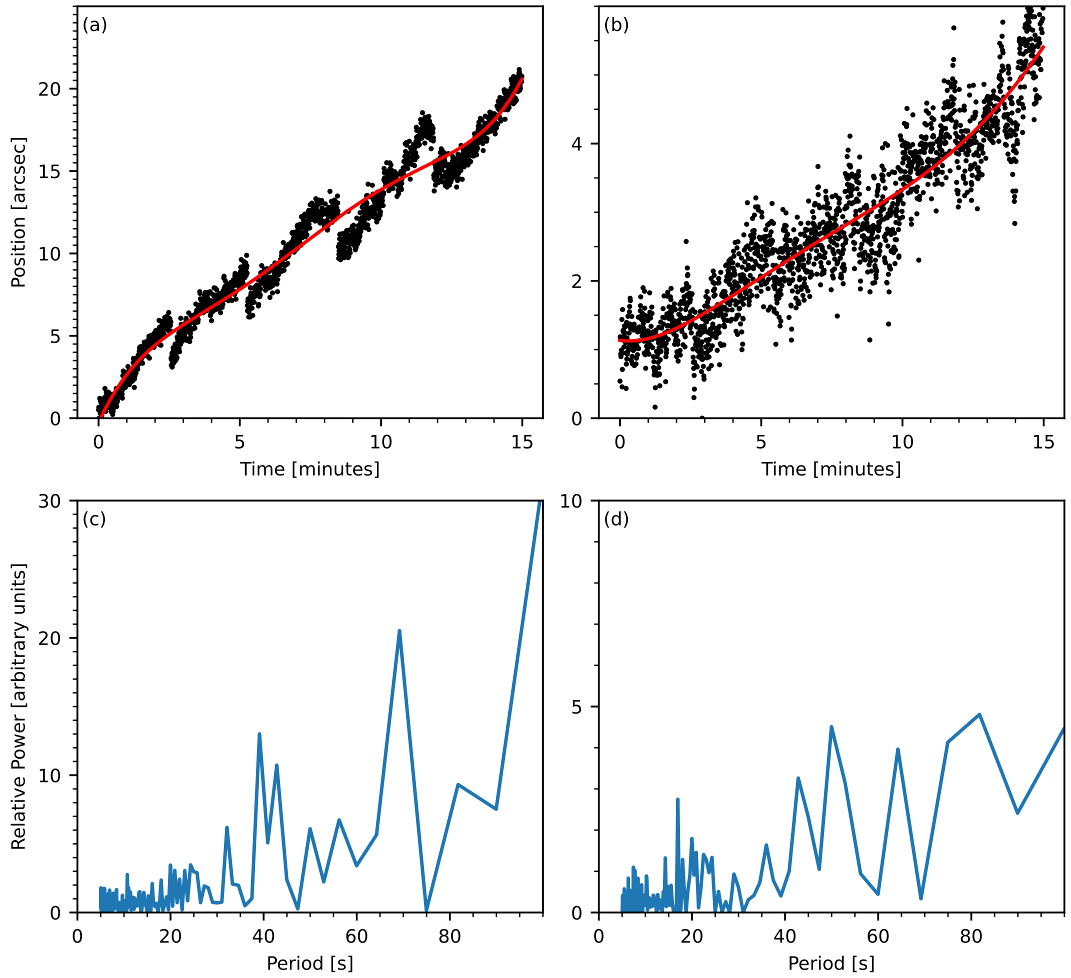

Figure 3.7: Image Drift measured using the sCMOS camera setup shown in Fig. 3.6 on 20th April 2022 08:15 AM IST. Panels (a) and (b) show the image drift measured for E-W and N-S directions, respectively, the black points show the actual image position with respect to reference and the red curve is a 5th order polynomial fit. Panels (c) and (d) show the Fourier power spectrum of the drift signals in panels (a) and (b) minus the polynomial fit.

Configuration Name	K_p	K_i	K_d
P	0.5 K_u	–	–
PI	0.45 K_u	0.54 K_u / T_u	–
PD	0.8 K_u	–	0.1 $K_\mathrm{u} T_\mathrm{u}$
Classic PID	0.6 K_u	1.2 K_u / T_u	0.075 $K_\mathrm{u} T_\mathrm{u}$
Pessen Integral Rule	0.7 K_u	1.75 K_u / T_u	0.0105 $K_\mathrm{u} T_\mathrm{u}$
some overshoot	0.33 K_u	0.66 K_u / T_u	0.11 $K_\mathrm{u} T_\mathrm{u}$
no overshoot	0.2 K_u	0.4 K_u / T_u	0.066 1.2 $K_\mathrm{u} T_\mathrm{u}$

Table 3.2: Different PID configurations in Ziegler-Nichols method

3.3.3.1 Deriving the optimum PID parameters

We followed the Ziegler-Nichols (Ziegler and Nichols, 1993) method to tune the PID parameters to reduce the amplitude of the image oscillations seen in the closed loop.

The Ziegler-Nichols (ZN) method is an heuristic method to derive the PID control parameters. The first step is to set the integral (K_{i}) and derivative (K_{d}) gain parameters to zero and keep increasing the proportional (K_{p}) gain until the system is unstable. The different PID configurations using ZN method (shown in Table 3.2) are then functions of the ultimate proportional gain (K_{u}) at which system was stable and had consistent oscillations and the period of the oscillations (T_{u}).

We found the value of K_{u} and T_{u} to be 1.7 and 21 s, respectively and used them to derive 7 different PID configurations (using Table 3.2) where were tested with the Auto Guider system. We found that the PD and no overshoot PID configuration showed significant improvement in the Fourier power spectrum (see Fig. 3.8 and 3.9), with maximum relative power of ~ 10 and ~ 15, respectively, compared to that of the power spectrum of image drift (~ 30; see Fig. 3.7). No oscillations of image position are found in image position data using PD controller (see panel (a) and (b) of Fig. 3.8) whereas image oscillations are seen in no overshoot PID controller image position data (see panels (a) and (b) of Fig. 3.9). In both the cases, image position is restricted to $\pm 2\,''$ about reference position and precision improved to $\sim 0.9\,''$ (root mean squared value). Therefore, we found PD controller works best followed by no overshoot PID controller. The precision of Auto Guider system improved to $\sim 0.9\,''$.

3.4 Conclusion

An Auto Guider System is installed and tested successfully at the Kodaikanal Tower Tunnel Telescope to arrest the image drift inherent in the telescope system. The image drift arrest capability of the system is much higher than the maximum drifts observed at the KTT and the system can keep the image stationary for long duration (tested up to ~ 180 minute and within the limits of the precision of the system $\sim 1.8\,''$). We showed that the fluctuations of image position and amplitude of oscillations about reference position can be minimized thereby improving precision to $\sim 0.9\,''$ by optimizing the PID control parameters. We expect this system to help in the operation of the low-order Adaptive Optics system planned to be installed at KTT.

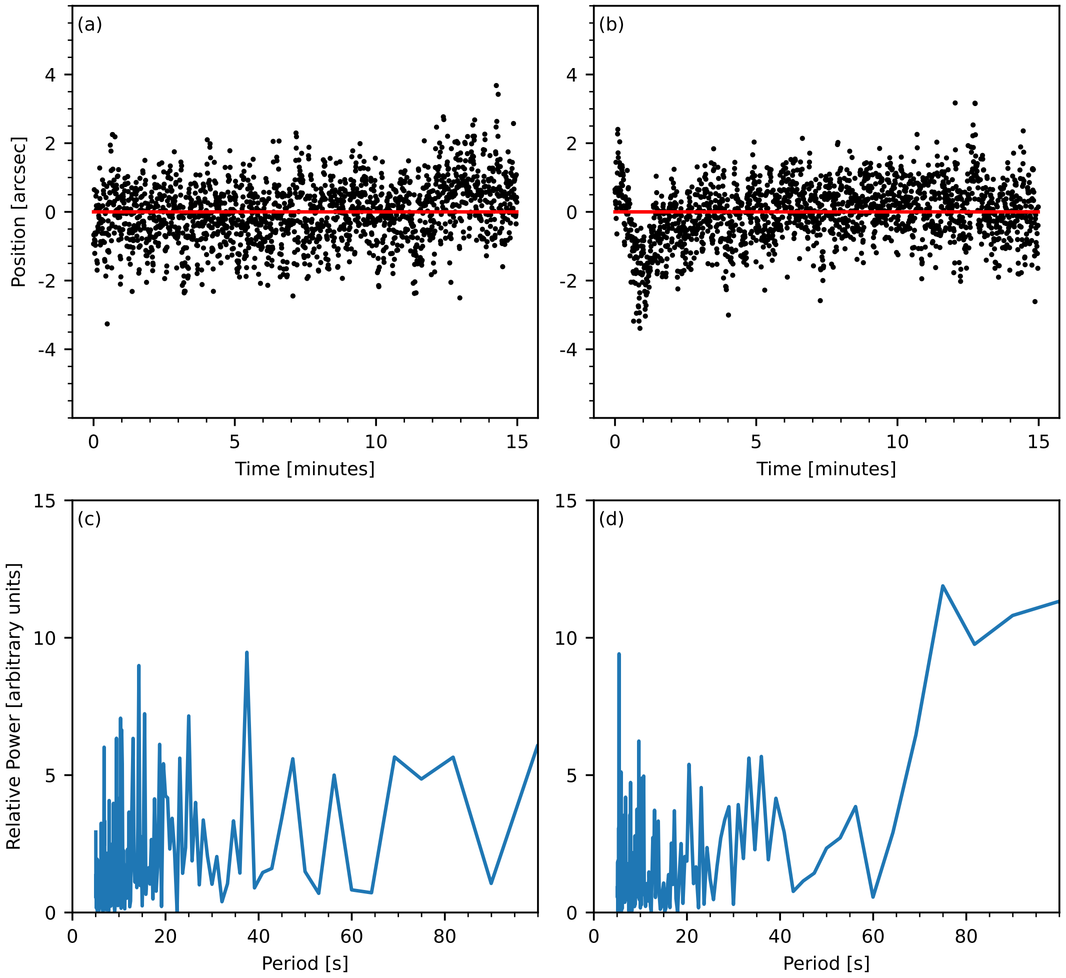

Figure 3.8: Image position with respect to reference for closed loop observation with K_p =1.376, K_i =0, K_d =3.57 (PD, K_u =1.7, T_u =21 s). Panels (a) and (b) show the data for E-W and N-S direction respectively. The Fourier power spectrum of the signals in panels (a) and (b) is shown in panels (c) and (d), respectively.

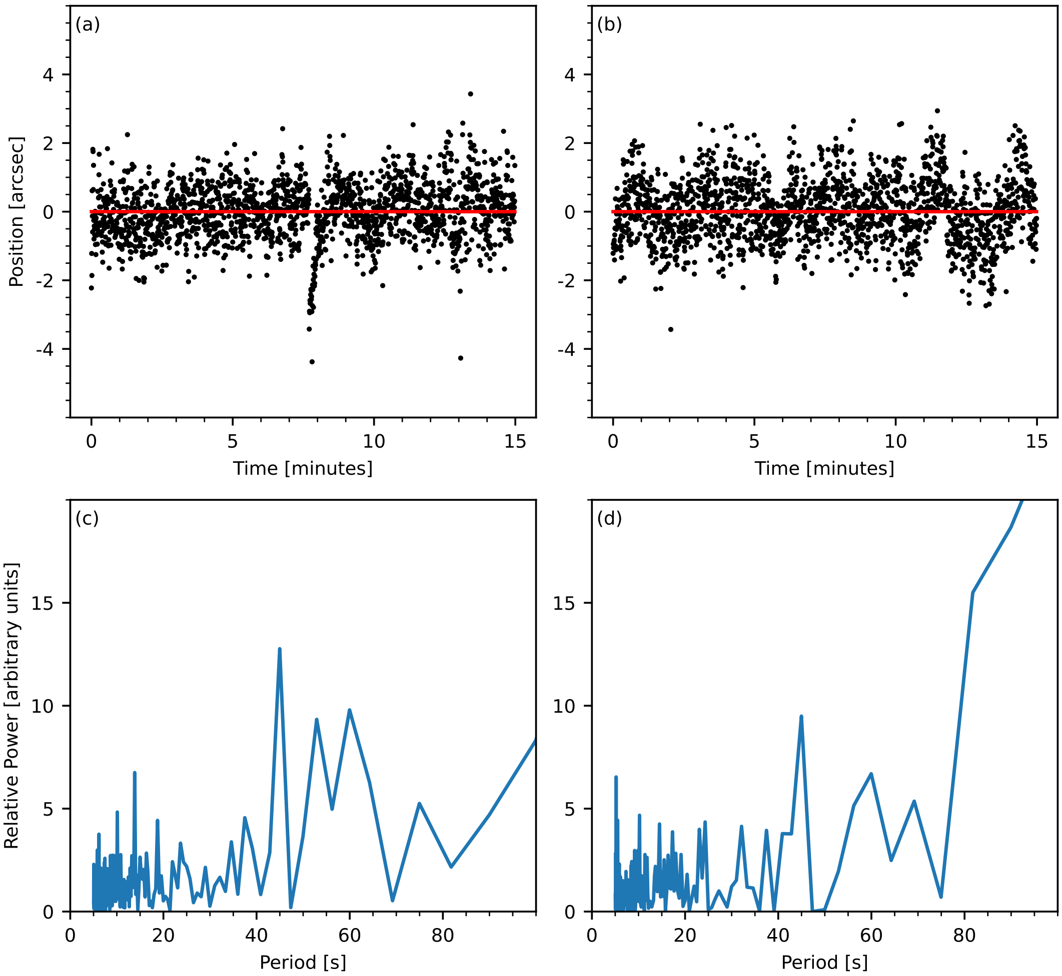

Figure 3.9: Image position with respect to reference for closed loop observation with $K_{\mathrm{p}}=0.34$, $K_{\mathrm{i}}=0.032$, $K_{\mathrm{d}}=2.37$ (no overshoot, $K_{\mathrm{u}}=1.7$, $T_{\mathrm{u}}=21$ s). Panels (a) and (b) show the data for E-W and N-S direction respectively. The Fourier power spectrum of the signals in panels (a) and (b) is shown in panels (c) and (d), respectively.

Chapter 4

Measurements of seeing-induced cross-talk in the tip-tilt corrected solar polarimetry

---

Measurements of seeing-induced cross-talk in the tip-tilt corrected solar polarimetry
Harsh Mathur, K. Nagaraju, Hemanth Pruthvi, and K. Sagaynathan, 2024, **Applied Optics**, 63, 4088-4094 (2024)

In the preceding chapter, we described our efforts in developing, testing, and installing an autoguider system. This system was developed as a precursor for a potential tip-tilt system. In this chapter, we describe our efforts in the integration of a tip-tilt system with the autoguider system. We also describe the simultaneous multiline spectropolarimetric setup that can work in tandem with the tip-tilt and autoguider systems. Consequently, we use the above system to investigate the effect of the tip-tilt system in mitigating the seeing-induced cross-talk observed in polarization measurements and present our findings therein. The complete contents of this chapter are accepted to be published in the Applied Optics journal, Mathur et al. (2024a).

4.1 Introduction

Accurate measurements of the solar magnetic field are crucial for understanding solar activity and its effects on our solar system. To infer solar vector magnetic fields through their imprints on the emergent spectra through the Zeeman and Hanle effects, accurate measurements of the polarization of light are required. Ground-based spectropolarimetric observations offer distinct advantages over measurements from space-based observatories like the Spectropolarimeter at Hinode (Hinode-SP) and Helioseismic and Magnetic Imager / Solar Dynamics Observatory (HMI / SDO). For high-resolution studies of specific solar regions, such as the quiet-Sun, active regions, and plages, large aperture telescopes are essential. These telescopes excel in capturing ample light and delivering superior spatial resolution, enabling the detailed study of intricate solar features. Nonetheless, ground-based measurements face challenges, particularly atmospheric turbulence that leads to random image aberrations that degrade spatial resolution and introduce spurious polarization (Lites, 1987; Judge et al., 2004; Krishnappa and Feller, 2012). Atmospheric seeing causes random image distortions on very short time scales (in the order of a few milliseconds) which randomly spreads the signal from one pixel to the other at a rapid pace. The spurious polarization, also known as seeing-induced cross-talk, is a result of the non-simultaneous nature of the polarization measurement process. As the detectors are not directly sensitive to polarization but only to intensity, the polarization signal is encoded (also known as polarization modulation) in terms of intensity variation, and the input signal is retrieved by decoding (demodulation) this intensity variation (del Toro Iniesta and Collados, 2000). A minimum of four intensity measurements are required to retrieve the input beam's complete polarization (all four Stokes parameters I, Q, U, and V) information. Unless these intensity measurements are completed within a few milliseconds, the measurement process results in a cross-talk among the Stokes parameters. To address these issues, technologies like tip-tilt and Adaptive Optics are employed to enhance image stability and minimize the impact of atmospheric distortions, thus improving the precision of ground-based solar magnetic field measurements (Rimmele and Marino, 2011).

Lites (1987) developed a Fourier transformation-based method to analyze cross-talk arising from atmospheric seeing, initially concentrating on tip-tilt effects linked to image motion. His work revealed that increasing modulation frequency effectively reduces cross-talk. Building upon Lites' work, Judge et al. (2004) further investigated residual image motion following tip-tilt correction through adaptive optics (AO). They explored both rotating-wave plate and discrete modulation approaches using liquid crystal variable retarders, concluding that improved correction of higher-order image aberrations results in reduced seeing-induced cross-talk. Consequently, combining a polarimeter with AO is anticipated to significantly reduce cross-talk in polarization measurements induced by atmospheric seeing. Nagaraju et al. (2011) and Krishnappa and Feller (2012), in their simulations, assessed the impact of higher-order aberrations and observed that the cross-talk among Stokes parameters remains practically unaffected by the extent of image aberration correction achieved by an AO system at high modulation frequencies. However, higher-order AO corrections enhance the signal-to-noise ratio by reducing the blurring caused by atmospheric seeing.

In this study, we assess the impact of the tip-tilt system on the reduction of the seeing-induced cross-talk present among Stokes parameters in both the Hα and Ca II 8662 Å spectra by comparing measurements taken with and without the tip-tilt system. The measurements are obtained with a spectropolarimeter (Pruthvi et al., 2018) at KTT (Bappu, 1967), which has been upgraded to enable simultaneous recording of spectropolarimetric observations in three spectral lines. We also discuss the tip-tilt system's performance and limitations.

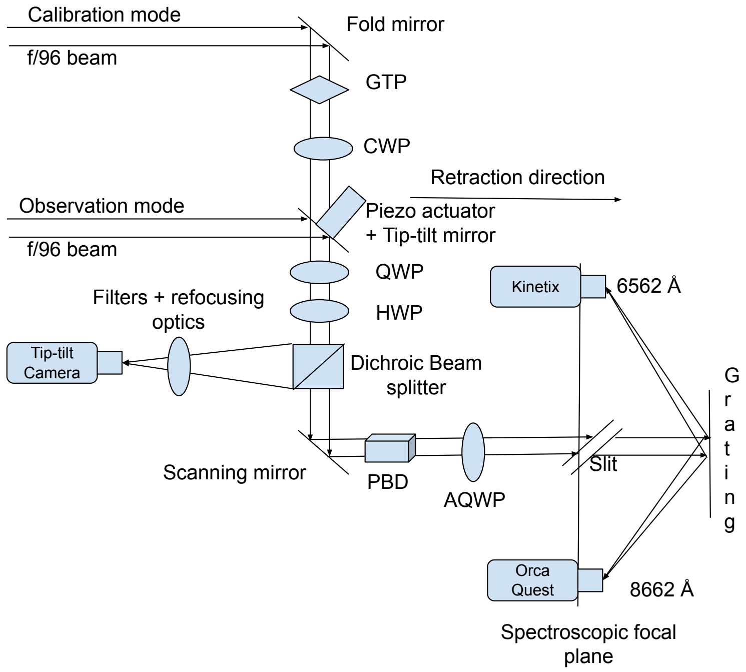

Figure 4.1: Optical layout of the tip-tilt system and the polarimeter setup at KTT. In observation mode, light from the telescope is fed to the modulation unit by a tip-tilt mirror which is glued to the piezo actuator. It passes through quarter wave plate (QWP), half wave plate (HWP), and dichroic beam splitter (DBS) that transmits light of wavelength above 600 nm. It is then reflected by another fold mirror (Scanning mirror), and passes through a polarizing beam displacer (PBD) that splits the beam in to two with orthogonal states of polarization, followed by an achromatic quarter wave plate (AQWP). In calibration mode, light from the telescope is fed to the calibration unit by yet another folding mirror. It then passes through a Glan-Thompson polarizer (GTP) and a quarter wave plate (CWP) producing light with known state of polarization. In this mode the Tip-tilt mirror is retracted and the light is allowed to passes through modulation unit and so on. The blue beam, with a wavelength less than 600 nm, passes through the DBS and proceeds to the tip-tilt camera, C-Blue One from First Light Imaging.

4.2 Observation setup

The data were acquired using the Kodaikanal Tower Tunnel Telescope (Bappu, 1967), which has a 3-mirror Coelostat placed in the tower as a light feeding system. The primary mirror (M1) is responsible for tracking the Sun, while the secondary mirror (M2) redirects the sunlight downwards. The tertiary mirror (M3) makes the beam horizontal and is followed by an achromatic doublet (effective aperture 38 cm, f/96) which focuses the Sun's image at a distance of 36 m with an image scale of $5\overset{\prime\prime}{\cdot}5$ mm^{-1}. M2 is further enhanced with a stepper motor, allowing adjustments in both North-South and East-West directions. This mechanism enables the movement of M2, consequently shifting the Sun's image on the image plane. This arrangement facilitated the development of an autoguider system for the telescope; more details are given in Mathur et al. (2022a). A tip-tilt system, concept demonstrated by Pruthvi (2019), has been incorporated into the autoguider system, called the image stabilization system. In this updated configuration, the C-Blue One camera from First Light Imaging is utilized, substituting the Andor Neo sCMOS camera, to serve as the tip-tilt camera. The details of the integration of the tip-tilt and autoguider system are provided in the appendix C.1, and were not included in this publication.

Using the polarimeter developed by Pruthvi et al. (2018), spectropolarimetric observations in the Ca II 8662 Å and Hα lines were recorded simultaneously, with and without tip-tilt system. Figure 4.1 shows a schematic of the tip-tilt and polarimeter setup at KTT. The light from the telescope (f/96) is directed to the modulation unit via a tip-tilt mirror affixed to a piezo actuator PSH10/2 from Piezosystem Jena. Within the modulation unit, there are a quarter-wave plate and a half-wave plate at 630 nm. Subsequently, the light passes through a dichroic beam displacer, which redirects the blue beam (with a wavelength less than 600 nm) to the tip-tilt camera, C-Blue One from First Light Imaging. The piezo-actuator and tip-tilt camera forms the tip-tilt system. Meanwhile, the science beam is transmitted to another fold mirror, which also functions as the scanning mirror. This mirror reflects the science beam towards a polarizing beam displacer, splitting the light into two orthogonally polarized components. Both polarized components then traverse through an achromatic quarter wave plate and continue to the slit of the Littrow mount grating-based spectrograph. The dispersed light from the grating falls onto the detector(s). The typical exposure time per slit position per modulation state per integration frame is 500 ms. A 4-stage modulation scheme were used with a total of 5 integration frames recorded per modulation state. Consequently, one set of measurements were recorded in 10 s (modulation frequency = 0.1 Hz).

To record the Hα and Ca II 8662 Å spectra, we installed two new cameras: the Kinetix from Teledyne (NUV and visible) and the ORCA-Quest from Hamamatsu (visible and NIR) at the spectrograph focal plane. However, accommodating three cameras at the spectrograph focal plane was not directly supported at KTT. To address this limitation, we have designed, in-house manufactured and installed a camera mount specifically tailored for KTT spectrograph. This new mount can support up to three cameras, and it accommodates both C and F-mount cameras. Moreover, the positions of the cameras are adjustable, allowing observers to record spectra simultaneously in three spectral regions of interest within the limitations of the space availability at the spectral focal plane.

To synchronize the capture and readout of the three cameras, the polarimeter software was updated accordingly. These adaptations enabled us to perform simultaneous spectropolarimetric observations in the desired spectral lines. In our upcoming paper, we will present our work focused on inferring the stratification of the magnetic field inferred using the spectropolarimetric observations recorded in the Ca II 8662 Å line. The magnetic field inferred will be compared from the application of the weak field approximation to the Stokes profiles in the Hα line.

4.3 Tip-tilt system performance and limitations

The top row of Fig. 4.2 presents a comparison of the power spectrum of image motion with and without the tip-tilt system recorded by the tip-tilt camera using a broadband filter with center wavelength at 550 nm and FWHM of 80 nm. The histogram of the image motion is presented in the bottom two rows. The spectrum without tip-tilt is derived from the image motion data recorded when only the image autoguider (Mathur et al., 2022a) system was operational. In contrast, the spectrum with tip-tilt is calculated from data recorded when both the tip-tilt and autoguider systems were operational. Both spectra were computed from data recorded for a duration of 1 hour.

Before implementing the tip-tilt system, only around 40% of the time did the image motion remain within $\pm0\overset{''}{.}11$. However, this percentage significantly improves to about 95% when the tip-tilt system is used, indicating a substantial reduction in image motion. Quantitatively, when we examine the power spectrum on the X-axis, the corrected spectrum (shown in black) begins to converge with the uncorrected spectrum (in blue) at approximately 80 Hz, which is referred to as the cut-off frequency. Beyond this point, the uncorrected power spectrum exhibits notably lower power compared to the corrected one. A similar trend is observed on the Y-axis, with both spectra merging around the same approximate frequency. Nevertheless, beyond this frequency, the corrected spectrum shows only marginal improvement over the uncorrected spectrum. It was also noted that the image movement when giving feedback to second mirror M2 is not smooth. When the second mirror moves, it induces pronounced vibrations, causing oscillations of the image on the image plane. A notable observation was the clear correlation between the moment feedback was provided to mirror M2 and the occurrence of large image shifts (not shown). Thus, there is a possibility of further improvement of the image stabilization system after the vibrations of the mirror M2 are addressed.

In conclusion, the image stabilization system, comprising the tip-tilt system and autoguider system, performs with a cut-off frequency of 80 Hz. There is a potential for improvement by addressing the vibrations of mirror M2 of KTT.

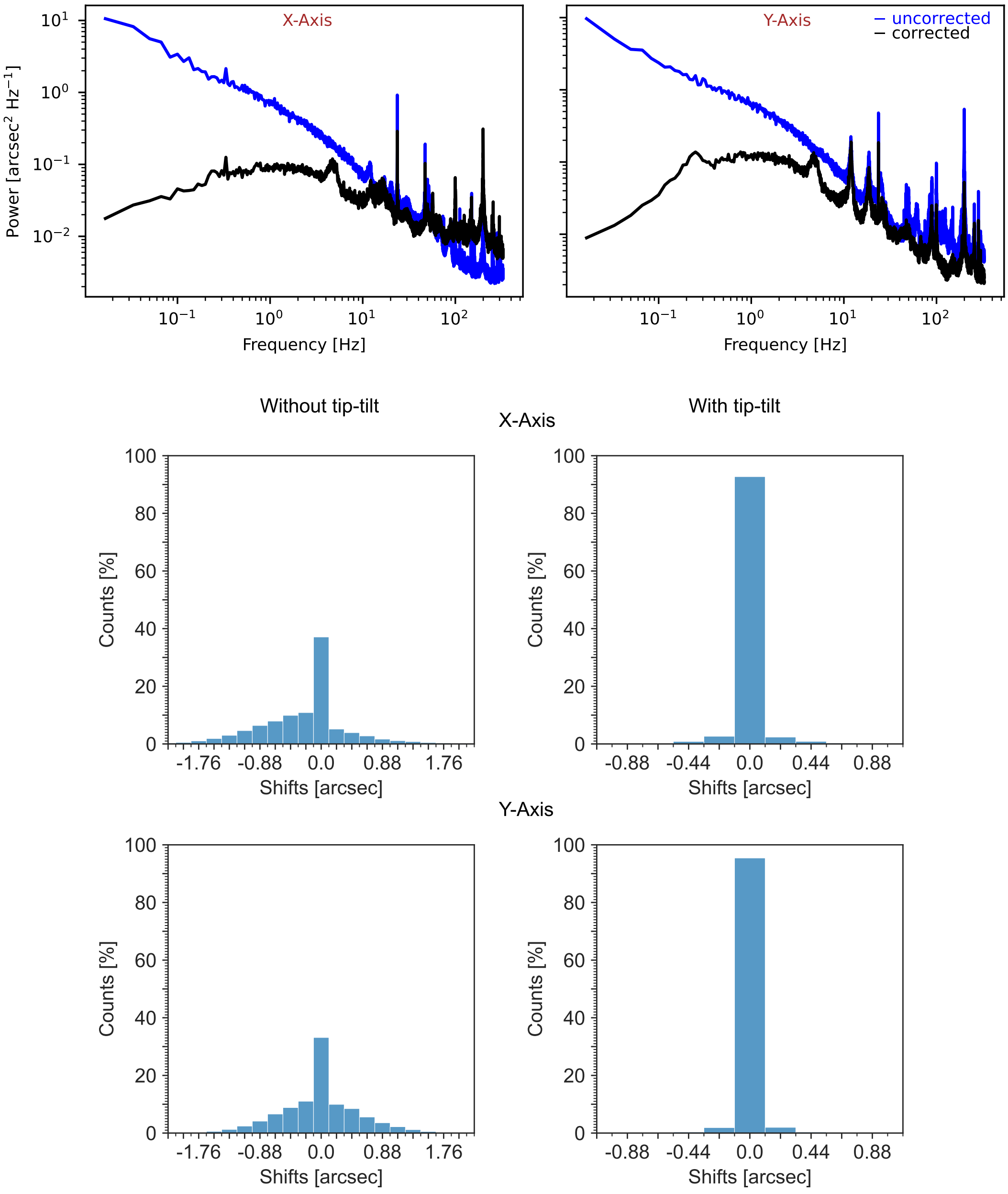

Figure 4.2: Performance of the image stabilization system. The panels in the top row compares the power spectra of the image motion with and without tip-tilt correction (duration 1 hour). The system reaches a point of diminishing returns in reducing image motion above approximately 80 Hz. The panels in the bottom two rows show the histogram of the image motion in the pixel scale before and while tip-tilt system is in use.

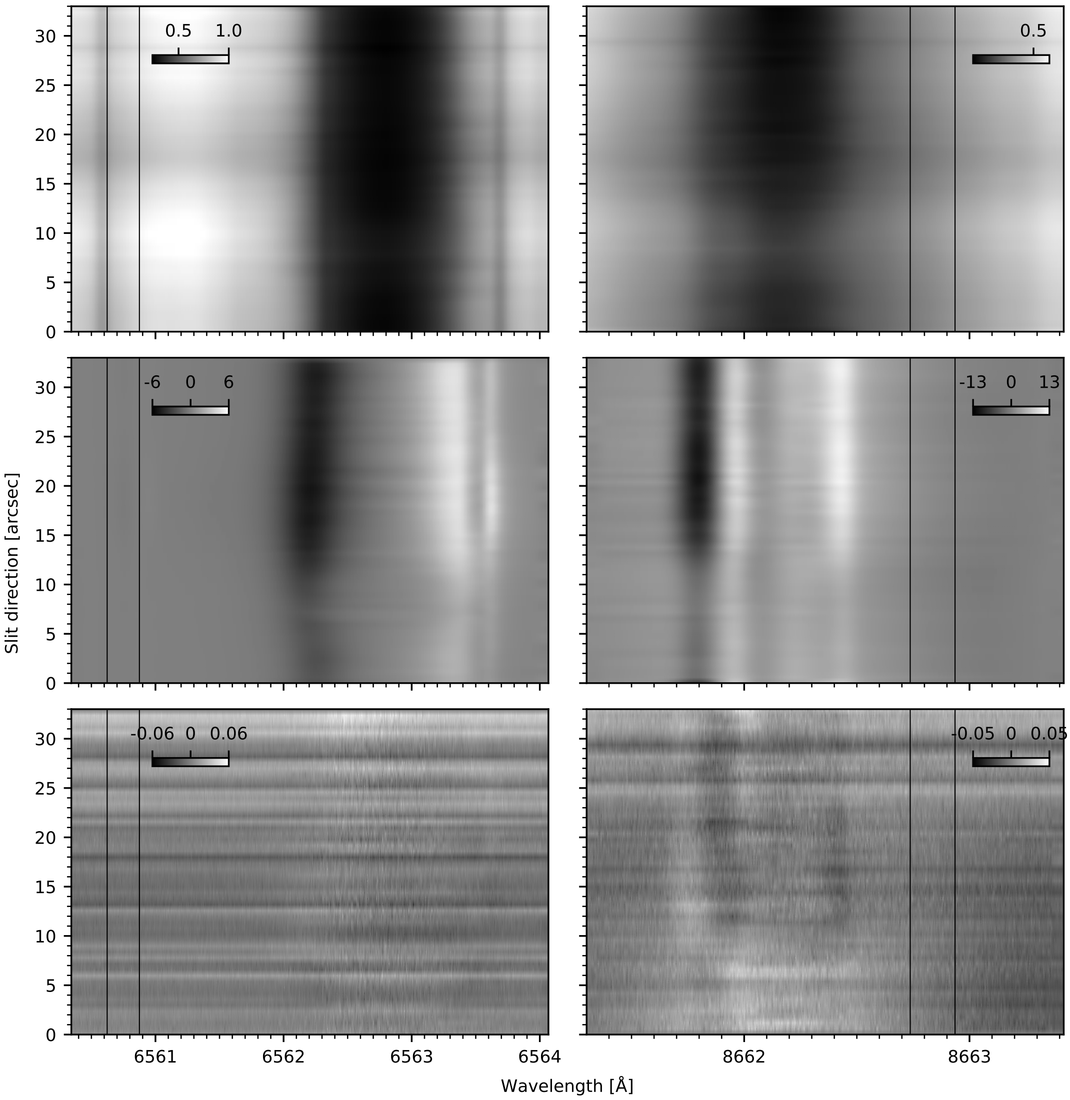

Figure 4.3: An spectral image showing the wavelength regions selected (black vertical lines) for calculating residuals. The left column shows data for Hα line while right column shows data for Ca II 8662 Å line. The top row shows spectral image of Stokes I, while middle row shows spectral image of Stokes V/I [%]. The bottom row shows the residuals for the Hα and Ca II 8662 Å lines, respectively.

Line	Term	Uncorrected mean	Corrected mean	Uncorrected rms	Corrected rms
Hα	$I \rightarrow Q$	0.012	0.004	0.018	0.005
Hα	$I \rightarrow U$	0.013	0.005	0.019	0.007
Hα	$I \rightarrow V$	0.016	0.007	0.023	0.009
Ca II 8662 Å	$I \rightarrow Q$	0.012	0.005	0.017	0.006
Ca II 8662 Å	$I \rightarrow U$	0.007	0.004	0.011	0.005
Ca II 8662 Å	$I \rightarrow V$	0.008	0.005	0.011	0.006

Table 4.1: Comparison of mean and rms cross-talk values of different terms of Hα and Ca II 8662 Å lines.

4.4 Seeing-induced cross-talk in the polarization measurements

The Earth's dynamic atmosphere causes cross-talk in the polarization measurements. Variations over time in the Earth's atmosphere result in wavefront distortions, subsequently causing spatial blurring of images and polarization. To mitigate the blurring of Stokes parameters, image stabilization methods like tip-tilt and adaptive optics systems are used. However, these techniques cannot eliminate the inter-mixing of Stokes parameters, known as seeing-induced cross-talk, which results from the slow modulation process compared to the rapid fluctuations induced by atmospheric conditions, occurring at frequencies around 500 Hz. If the modulation frequency is of the order of 1 kHz, the seeing-induced cross-talk is not of much concern, however, is challenging to achieve (Lites, 1987; Judge et al., 2004; del Toro Iniesta, 2007). Consequently, the Stokes parameter I_A measured at the telescope's entrance aperture following the propagation of light through the atmosphere is as follows,

$$I_A = I_l + < \delta I_l > + \delta I_l \tag{4.1}$$

where $< \delta I_l >$ represents the spatial smearing (time averaged) of true Stokes parameter I_l due to atmospheric conditions, which we neglect assuming the tip-tilt system is operational and δI_l are spurious polarization features induced due to the slow modulation frequency.

Let O be the modulation matrix of the combined system consisting of telescope optics and the polarimeter, then the recorded modulated intensities, $I_{meas,k}$, for the kth modulation state are given by,

$$I_{meas,k} = \sum_{l=1}^{4} O_{kl}(I_l + \delta I_{lk}) \tag{4.2}$$

where δI_{lk} is the spurious polarization feature, δI_l, introduced to the kth modulation state. The Stokes vector (I_{infer}) are extracted from the measured intensities by multiplying the demodulation matrix (D) with modulated intensities (I_{meas}),

$$I_{infer,1} = I_1 + \sum_{k=1}^{4}\sum_{m=1}^{4} D_{1k} O^T_{km} \delta I_{mk}$$

$$I_{infer,l} = I_l + \sum_{k=1}^{4}\sum_{m=1}^{4} D_{lk} O^T_{km} \delta I_{mk} \quad \text{for } l = 2, 3, \text{ and } 4 \tag{4.3}$$

where D can be calculated from the modulation matrix (O) by,

$$D = (O^T O)^{-1} O^T \tag{4.4}$$

The dual-beam polarimetry technique is commonly employed to reduce the impact of seeing-induced cross-talk, specifically $Q, U, V \rightarrow I$ and $I \rightarrow Q, U, V$. In the polarimeter setup, a polarizing beam displacer is employed as the analyzer instead of a single linear polarizer. This allows for the simultaneous recording of intensities from two orthogonally polarized beams. The intensity in each beam is modulated with same sign while the remaining Stokes parameters ($Q/U/V$) are modulated with opposite signs. This is due to the elements in the first column of the modulation matrix being equal to "1", and the remaining elements of the modulation matrix having equal magnitude but opposite signs in the two orthogonally polarized beams. By averaging the Stokes parameters obtained from both beams, crosstalk $Q, U, V \rightarrow I$ as well as $I \rightarrow Q, U, V$ is effectively neutralized. The $I \rightarrow Q, U, V$ crosstalk specifically is determined by halving the difference in Stokes parameters measured from the two oppositely polarized beams(for more details, please refer to chapter 5, page no 68 of del Toro Iniesta (2007)).

4.5 Measurements of seeing-induced cross-talk in the polarization measurements

The polarimeter at KTT is a dual beam system Pruthvi et al. (2018). As explained in the previous section, the Stokes parameters are typically determined independently from each of the two orthogonally polarized beams and then averaged to reduce the spurious signals caused by atmospheric turbulence. In order to compare the seeing-induced cross-talk before and after implementing the tip-tilt system, we analyze the residuals of the Stokes parameters in the wing positions of the Hα and Ca II 8662 Å lines. These residuals are calculated by halving the difference between the Stokes parameters independently derived from each of the two beams. The residuals of the Stokes parameters represent the seeing-induced cross-talk ($I \rightarrow Q, U, V$). Figure 4.3 shows the wavelength regions selected (shown by black vertical lines) for calculating

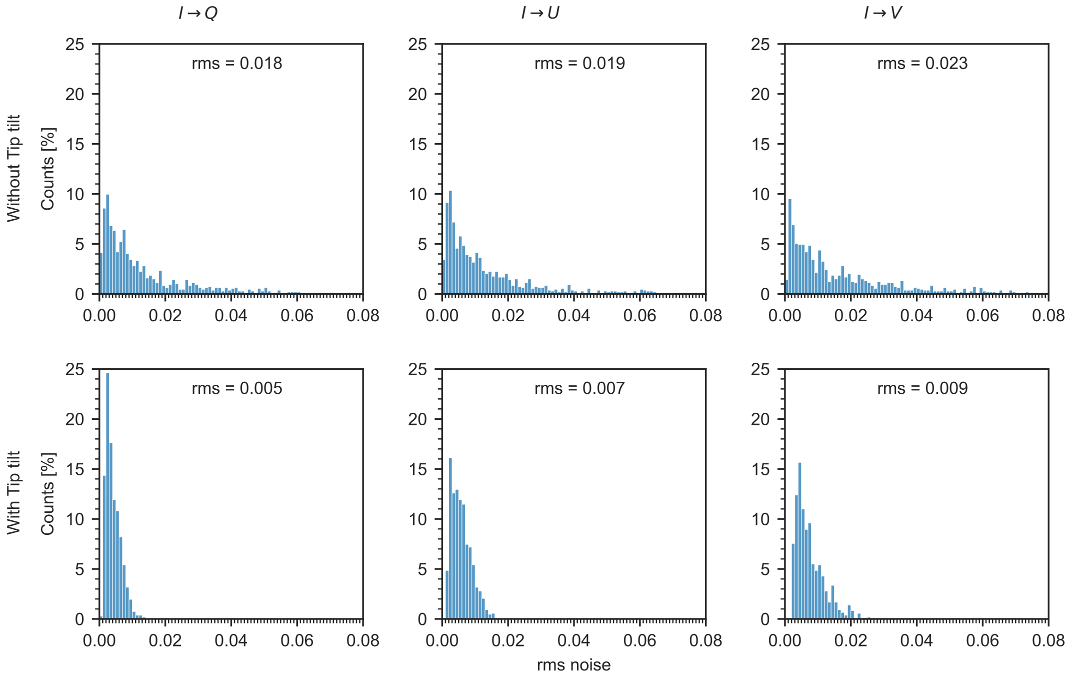

Figure 4.4: An analysis of seeing-induced cross-talk in polarimetric measurements for the Hα line is conducted with and without the implementation of a tip-tilt system. In the top row, we show the histogram of the root mean square of the residuals without the tip-tilt system for Stokes Q/I, U/I and V/I, column-wise, respectively. The bottom row shows the histograms when the tip-tilt system was operational. The rms residual were determined by calculating residuals of the Stokes parameters in the wing of the Hα line. The Stokes parameters were independently determined from each beam and then subtracted and halved to give the residual. The results reveal a significant reduction in rms residual, with Stokes Q/I showing a decrease by a factor of 3.6, Stokes U/I showing a decrease by a factor of 2.7 and Stokes V/I showing a decrease by a factor of 2.5.

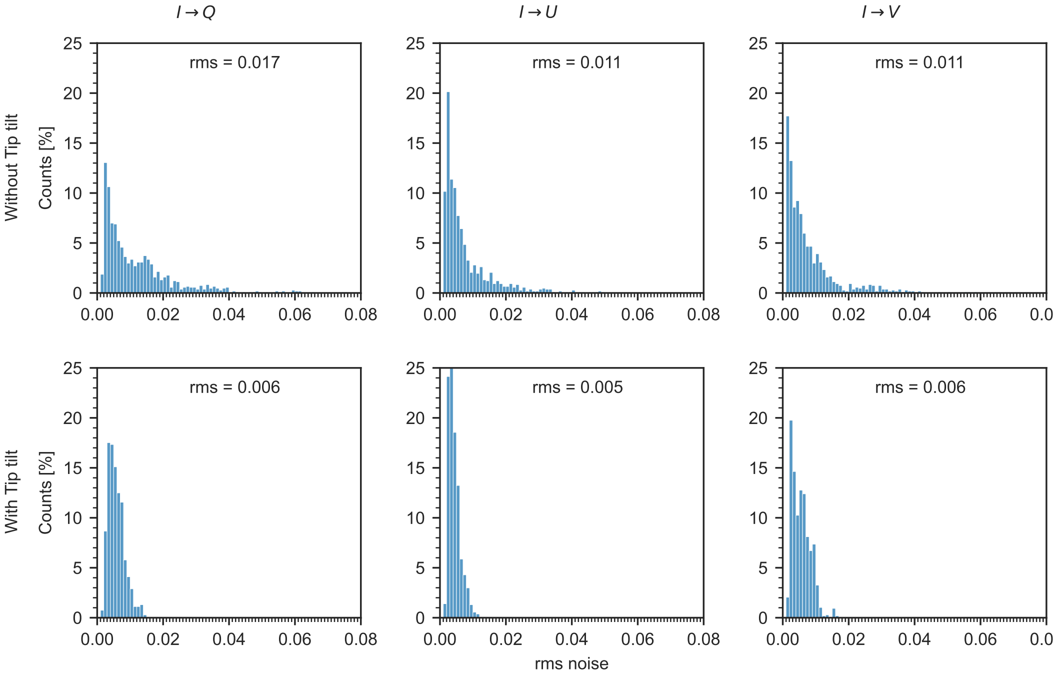

Figure 4.5: Similar to Fig. 4.4, but for the Ca II 8662 Å line. The results reveal a significant reduction in rms residual, with Stokes Q/I showing a decrease by a factor of 2.8, Stokes U/I showing a decrease by a factor of 2.2 and Stokes V/I showing a decrease by a factor of 1.8.

the residuals. The wavelength region selected for Ca II 8662 Å line is comparatively inside the line than that of Hα line because there were considerable fringes present in the raw data which were removed during post-processing. This context image is made from the aligned, fringe-removed merged beam data. The mean and rms values of root mean square (rms) values of cross-talk of different terms in the Hα and Ca II 8662 Å lines are compared in Table 4.1. The histogram of the rms values of the Stokes Q/I, U/I, and V/I residuals of the Hα and Ca II 8662 Å lines are shown in Fig. 4.4 and 4.5, respectively.

The Hα residual spectrum exhibits residual levels as high as 0.06 (6%) for Stokes Q/I, 0.07 (7%) for Stokes U/I, and 0.08 (8%) for Stokes V/I without the tip-tilt system. However, with the tip-tilt system, the maximum residual value significantly reduces to 0.014 (1.4%) for Stokes Q/I and U/I and 0.03 (3%) for Stokes V/I, and the spread of the distribution narrows, with most pixels having residuals around 0.003 (0.3%) for Stokes Q/I and U/I and 0.005 (0.5%) for Stokes V/I. The root mean square value of residual also decreases by a factor of 3.6, 2.7, and 2.5 for Stokes Q/I, U/I, and V/I, respectively. Similarly, in the Ca II 8662 Å spectrum, the value of residuals can reach up to 0.06 (6%) for Stokes Q/I, 0.05 (5%) for Stokes U/I, and 0.04 (4%) for Stokes V/I without the tip-tilt system but decreases to 0.015 (1.5%) for Stokes Q/I, 0.013 (1.3%) for Stokes U/I, and 0.02 (2%) for Stokes V/I when the tip-tilt system is employed. The root mean square value of the residual decreases by a factor of 2.8, 2.2, and 1.8 for Stokes Q/I, U/I, and V/I, respectively. The distribution in the Ca II 8662 Å distribution also narrows, with most pixels having noise around 0.005 (0.5%) for all Stokes parameters. Using image motion power spectra, Judge et al. (2004) reported the $I \rightarrow Q, U, V$ cross-talk of about ∼0.006 for rotating retarders based polarimeters after tip-tilt correction, which is comparable to the rms cross-talk observed in the tip-tilt corrected Hα and Ca II 8662 Å spectrum.

We note here that the cross-talk estimated in the data, does not exist in the reduced science ready data, it is only brought out to show the effect of tip-tilt system in reducing the cross-talk. Despite the widespread use of tip-tilt systems in solar telescopes (Rimmele and Marino, 2011), no such direct measurements of seeing-induced cross-talk have been reported in the literature. A manuscript describing measurements of seeing-induced cross-talk with and without tip-tilt system carried out at the German Vacuum Tower Telescope (VTT; von der Lühe, 1998) using Tenerife Infrared Polarimeter (TIP-II; Collados et al., 2007) instrument is in preparation by Nagaraju et. al (private communication). Our conclusion from this analysis is that the tip-tilt system implemented at KTT noticeably decreases the root mean square (rms) cross-talk by a minimum factor of 2.

4.6 Conclusion

We have presented measurements of the cross-talk in the Stokes parameters induced by the atmospheric seeing with and without the tip-tilt sytsem being in use. This was done to show the effect of tip-tilt system in reducing the seeing induced cross-talk. In that context, we have integrated and installed a tip-tilt system with an autoguider system to arrest the residual image motion. The tip-tilt system is shown to have a cut-off frequency of 80 Hz, keeping image shifts within $\pm 0.11''$, 95% of the time. Two new cameras, Kinetix from Teledyne and Orca Quest from Hammamatsu are installed on the spectroscopic focal plane to record the Hα and Ca II 8662 Å spectrum simultaneously. With the help of the image stabilization system, the seeing-induced cross-talk measured in the Stokes parameters of the Hα and Ca II 8662 Å spectrum is shown to reduce at least by a factor of 2.

Chapter 5

Simultaneous spectropolarimetric observations in the Hα and Ca ii 8662 Å lines of an active region

---

Simultaneous spectropolarimetric observations in the Hα and Ca II *8662 Å lines of an active region*
Harsh Mathur, K. Nagaraju, Rahul Yadav, and Jayant Joshi, 2024, **The Astrophysical Journal**, accepted, June 2024.

In chapters 3 and 4, we described our instrumentation efforts to enable the Kodaikanal Tower Tunnel Telescope to record spectropolarimetric observations in three spectral lines simultaneously. This was done to record spectropolarimetric observations of the Hα line simultaneously with one of the Ca II IR triplet lines towards the goal of investigating whether the Hα line probes the chromospheric magnetic field. Using the observation setup described in preceding two chapters, we have recorded spectropolarimetric observations of an active region, NOAA 13315 on 27th May, 2023, in the Hα and Ca II 8662 Å lines simultaneously. In this chapter, we present an analysis of the observations presenting the comparison of the line-of-sight magnetic field inferred from the non-LTE inversions of the Ca II 8662 Å line with of inferred from WFA over the Hα line. The contents of this chapter in its entirety are accepted to be published in The Astrophysical Journal, Mathur et al. (2024b).

5.1 Introduction

Simultaneous multiline spectropolarimetry is a powerful observational technique that allows the inference of the magnetic field at multiple heights of the solar atmosphere.

In the recent past, many authors have used spectropolarimetric observations of Ca II 8542 Å / He I 10830 Å lines recorded simultaneously with lines of Fe I atom to infer the stratification of the line-of-sight (LOS) magnetic field in various solar features. Just to mention a few recent studies, the 3-D structure of the magnetic field of sunspots from photosphere to middle chromosphere has been studied by Murabito et al. (2019), Joshi et al. (2017), Joshi et al. (2016), and Schad et al. (2015). Magnetic field variation in umbral flashes has been studied by many authors in recent literature (for example Felipe et al., 2023; French et al., 2023; Bose et al., 2019; Joshi and de la Cruz Rodríguez, 2018; Houston et al., 2018). Magnetic topologies of inverse Evershed flow have also been reported in literature (Prasad et al., 2022; Beck and Choudhary, 2019). Changes in the chromospheric field during flares are studied by many authors (Ferrente et al., 2023; Vissers et al., 2021; Yadav et al., 2021; Libbrecht et al., 2019; Kuridze et al., 2018; Kleint, 2017). For a detailed overview of advancements in measurement techniques and analysis methods, we refer the reader to Lagg et al. (2017).

Both He I 10830 Å and Ca II 8542 Å lines present valuable tools for probing the chromospheric magnetic field due to their relatively well-understood line formation and interpretability using non-local thermodynamic equilibrium (non-LTE) inversion codes (e.g. Socas-Navarro, Trujillo Bueno, and Ruiz Cobo, 2000b; Asensio Ramos, Trujillo Bueno, and Landi Degl'Innocenti, 2008; de la Cruz Rodríguez, Leenaarts, and Asensio Ramos, 2016; de la Cruz Rodríguez et al., 2019; Ruiz Cobo et al., 2022). However, it is crucial to acknowledge their inherent limitations. The formation of the He I 10830 Å line occurs within a limited range of heights in the upper chromosphere, and its formation relies on incoming EUV radiation from the coronal and transition region (Andretta and Jones, 1997; Leenaarts et al., 2016). This offers sensitivity to specific atmospheric layers but limits its applicability across diverse solar features. In contrast, the Ca II 8542 Å line forms from the upper photosphere to the mid-chromosphere, providing broader spatial coverage. However, in flaring active regions, the Ca II ion gets ionized to the Ca II ion, potentially causing the Ca II 8542 Å line to sample deeper layers of the solar atmosphere (Kerr et al., 2016; Kuridze et al., 2018; Bjørgen et al., 2019). Thus it is challenging to interpret magnetic field measurements in such dynamic environments using the Ca II 8542 Å line.

The spectropolarimetric observations of the Hα line recorded simultaneously with observations of established spectral lines, such as those of the Ca II atom can serve as an effective means to investigate the chromospheric magnetic field. This is because a previous study by Carlsson and Stein (2002) have demonstrated that the opacity of the Hα line in the upper chromosphere is primarily governed by the ionization degree and radiation field, which remain largely unaffected by local temperature fluctuations but are influenced by mass density (Leenaarts, Carlsson, and Rouppe van der Voort, 2012). Recent work by Bjørgen et al. (2019) further corroborated that the Hα line maintains opacity even within flaring active regions through synthesizing spectra using 3D rMHD simulations. Furthermore, our recent study, Mathur et al.

(2023), revealed that the weak field approximation (WFA) over the Hα line core exhibits a morphology of the LOS magnetic field remarkably similar to inversions of the Ca II 8542 Å line. This finding underscores the potential of Hα spectropolarimetry for probing the chromospheric magnetic field.

Despite the potential of the Hα line as a valuable chromospheric diagnostic tool, its utilization in probing the chromospheric magnetic field remains limited. One contributing factor is that despite the dominance of the Zeeman effect in the Stokes V signal, the line's intensity and polarization profiles are sensitive to the 3D radiation field. Additionally, in scenarios involving weakly magnetized atmospheres, the Stokes Q & U signals are influenced by atomic polarization (Štěpán and Trujillo Bueno, 2010, 2011). Thus, it is challenging to model the Hα line using existing inversion codes that adopt 1.5D plane-parallel geometry.

In this paper, we report the line-of-sight (LOS) magnetic field measurements of an active region inferred from the simultaneous multiline spectropolarimetry in the Ca II 8662 Å and Hα lines using state-of-the-art non-LTE inversions and weak field approximation methods. Recently Mathur et al. (2023) have analyzed the diagnostic potential of the Hα line in probing chromospheric magnetic field. However, their observations were limited to a small pore. Unlike Mathur et al. (2023), in this work, we present a comprehensive analysis of spectropolarimetric observations of a complex active region consisting of 4 umbrae, 1 penumbra, and a region where the Ca II 8662 Å line core is in emission, a signature of localized heating. The Ca II 8662 Å line has **a** similar formation to that of the Ca II 8542 Å line, is magnetically sensitive, and can be used as a chromospheric diagnostic (Pietarila, Socas-Navarro, and Bogdan, 2007b,a).

5.2 Observations

The observations were made using the polarimeter (Pruthvi et al., 2018) at the Kodaikanal Tower Tunnel (KTT) Telescope (Bappu, 1967) at the Kodaikanal Solar Observatory (KoSO) in the Hα and Ca II 8662 Å lines simultaneously. The Fe I 8661.8991 Å line, which appears as a blend in the Ca II 8662 Å spectrum was also recorded. The spectral sampling of the Hα and Ca II 8662 Å lines data were 4.4 mÅ per pixel and 3.6 mÅ per pixel, respectively. The pixel scale in the scan direction and slit-direction were binned to $0\overset{''}{.}6$ per pixel. The observed field of view (FOV) consists of an active region (NOAA 13315) with multiple sunspots and a light bridge with a viewing angle $\cos\theta = \mu = 0.96$. Here, θ is the angle between the line-of-sight (LOS) direction and the local surface normal. In each scan step of the raster scan, with step size $0\overset{''}{.}275$, we recorded spectropolarimetric data using a 4-stage modulation scheme. A total of 5 frames were recorded for each modulation state, with each frame having an exposure time of 500 ms. The spectropolarimetric raster scan was completed over the course of approximately one hour, beginning at 02:14:42 UT

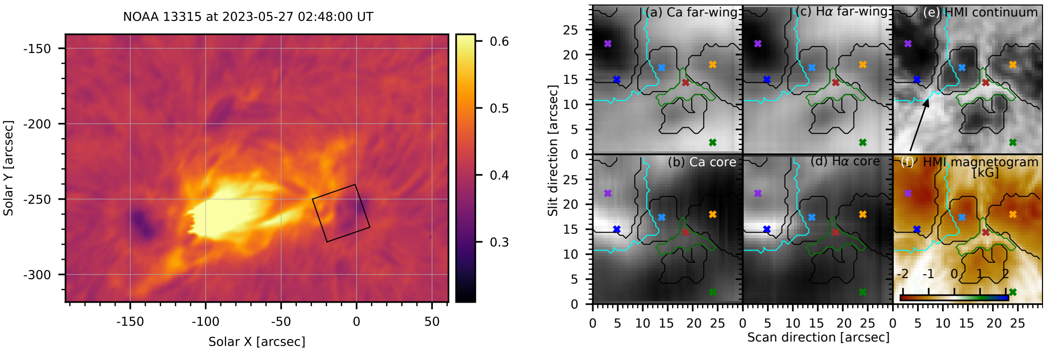

Figure 5.1: On May 27th, 2023, active region data (NOAA 13315), was recorded. The left panel shows an Hα filtergram near the core of the Hα line with FWHM of 0.4 Å recorded using the Hα telescope at the Kodaikanal Solar Observatory. The observed FOV using the spectropolarimeter at the KTT is marked by the black square and is further shown in right panels. Panels (a) and (b) display images of the Ca II 8662 Å line: panel (a) shows a far wing image at an offset of −0.8 Å, from the line core, while panel (b) shows the image at the nominal line center. Similarly, panels (c) and (d) show images of the Hα line: panel (c) presents a far wing image at −1.36 Å, from the line core, and panel (d) shows the image at the nominal line center. Panel (e) is the HMI continuum, and panel (f) is the HMI line-of-sight magnetogram for reference. The arrow shows the direction of the disc center. The black and green color contours represent the umbral and lightbridge regions, respectively. The cyan color contour represents the region showing emission feature in the Hα filtergram and in the Ca II 8662 Å line.

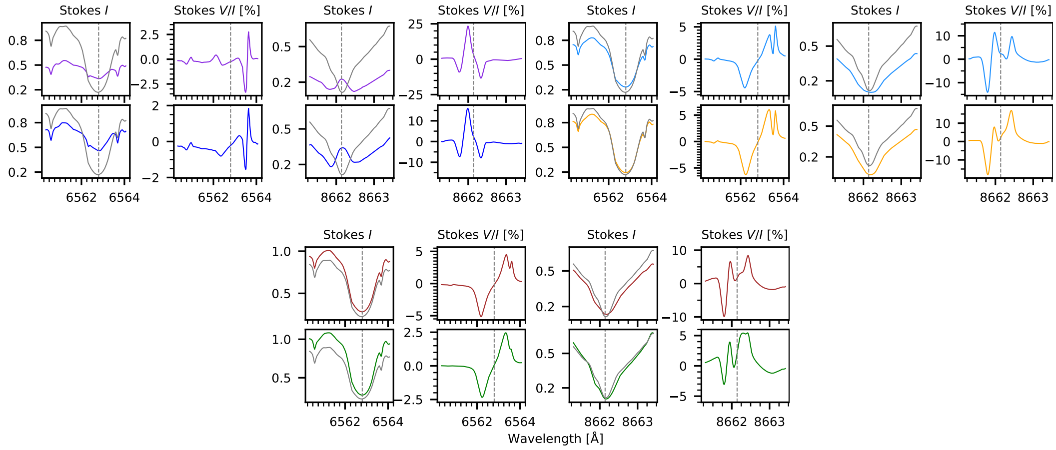

Figure 5.2: Spectral profiles of a few selected pixels, marked with “×” in panels (a)–(f) of Fig. 5.1. The quiet-Sun profile (solid gray) is also shown for comparison. The gray dashed vertical line shows the position of the nominal line center.

and concluding at 03:12:19 UT on May 27th, 2023. A tip-tilt system (Mathur et al., 2024a) was used during observations. The data were corrected for dark- and flat-field variations, instrumental polarization, and polarization fringes. The details are given in the appendix D.1. The Ca II 8662 Å data were aligned with the Hα data by cross-correlating the far wing images of the field-of-view (FOV) at the Ca II 8662 Å and Hα lines. Further, the Hα data were co-aligned with the Helioseismic and Magnetic Imager (HMI) continuum image. We also show an Hα filtergram with FWHM of 0.4 Å recorded using the Hα telescope at the Kodaikanal Solar Observatory as a context image and describe further in the text.

An overview of observations is shown in Figure 5.1. The panel on the left shows an emission feature over the active region NOAA 13315. The observed FOV, marked by a black square in the left-panel and shown in panels on the right, covers the emission region partially and the sunspot with multiple structures. The continuum images for both the Hα and Ca II 8662 Å lines exhibit a resemblance to the HMI continuum image (see panels (a), (c), and (e)). The active region contains multiple structures of sunspot joined by a lightbridge. The images at the core of the Hα and the Ca II 8662 Å lines appear similar (see panels (b) and (d)). The active region contains strong fields of negative polarity with a maximum field strength of up to -1900 G (see panel (f)). In both the Hα and Ca II 8662 Å line core images, a prominent enhanced emission feature, exhibiting its peak emission about scan direction $5''$ and slit position $15''$ within the field of view (FOV), is seen.

The quiet-Sun profiles for both the Hα and Ca II 8662 Å lines were generated through the averaging of profiles obtained from a select number of pixels within a region situated far from the sunspot from the extended FOV not shown in the right panels of Fig. 5.1. The procedure for wavelength calibration, as detailed in appendix D.1, involved comparing the quiet-Sun profile with that of the BASS 2000 atlas. Additionally, corrections for spectral veil were applied to both the Ca II 8662 Å and Hα data.

A few selected spectral profiles corresponding to various dynamics of the FOV, marked in panels (a)-(f) of Fig. 5.1 by "×", are shown in Fig. 5.2 using the same color. Quiet-Sun profile calculated by averaging a few pixels outside the active region is also shown for comparison.

The purple-colored spectral profile belongs to the pixel in the darkest umbral region seen in the far wing images of the Hα and Ca II 8662 Å lines. This pixel exists in the periphery of the emission feature seen in the core of the Hα and Ca II 8662 Å lines. In the Stokes I profile of the Hα line, there is a noticeable decrease in intensity within the line wings, a typical characteristic observed in the dark umbral regions. Moreover, this profile reveals a heightened intensity at its core, in contrast to the quiet-Sun profile, indicating an enhanced emission in the core of the line. The Stokes V/I profile of the Hα line shows an amplitude of 1%, however, the Co I blend has an amplitude of 3%. In contrast to the Hα line, for this pixel the Stokes I profile of the Ca II 8662 Å line core is seen in emission. Although the peak of the emission appears un-shifted with respect to the position of the nominal line core, the two minima on either side of the emission peak have different amplitudes, suggesting line-of-sight velocity gradients. The Stokes V/I profile of the Ca II 8662 Å line is not the typical anti-symmetric two-lobed profile. This variation is due to the presence of the magnetically sensitive Fe I 8661.8991 Å line, which appears as a blend blueward to the core of the Ca II 8662 Å line. In case of nominal absorption of Stokes I of Ca II 8662 Å line, the red lobe of the Stokes V/I of the Fe I 8661.8991 Å line and the blue lobe of the Ca II 8662 Å line merge, making it challenging to distinguish their amplitude distinctly. In the present case of the Stokes I profile in emission, we have observed a distinct three-lobed structure in the Stokes V/I profile, with the amplitudes of the Stokes V/I alternating in sign. The amplitude of the blue and the red lobes are about 10%, whereas the amplitude of the central lobe is observed to be about 25%.

The navy-colored spectral profile is associated with a pixel situated near the peak of the enhanced emission feature observed in the images at the core of the Hα and Ca II 8662 Å lines. This profile, like its purple counterpart, displays a reduction in the intensity of the line wings in both the Hα and Ca II 8662 Å Stokes I profiles, when compared to their corresponding quiet-Sun profiles. However, the decrease in intensity is less pronounced than in the purple-colored profile. This lesser reduction is attributed to the pixel's location being outside the dark umbral area, as seen in the far wing images of the Hα and Ca II 8662 Å lines. The line core of the Hα line's Stokes I profile exhibits increased intensity compared to the quiet-Sun profile, and the Stokes I profile of the Ca II 8662 Å line appears in emission. The core intensity of both the Hα and Ca II 8662 Å lines is higher than in the purple-colored profile. The Stokes V/I profile shapes for both lines are analogous to those of the purple-colored profile, yet the amplitude of the Stokes V/I profile for the Co I blend and the middle lobe of the Ca II 8662 Å line is significantly lower than that of the purple colored profile. This difference in amplitude can be linked to the weaker magnetic field at the navy-colored pixel's location compared to the field strength at the purple-colored pixel's location, as seen in panel (f) of Fig. 5.1. The amplitude of the Stokes V/I profile of the Hα line is about 0.9%. The amplitude of the blue and red lobes of the Ca II 8662 Å line is about 8%, whereas the amplitude of the central lobe is about 15%.

The cyan- and yellow-colored profiles represent typical profiles in a sunspot umbra. The Stokes I profiles of the Hα line show nominal absorption profiles, with reduced intensity in the line wings and slightly elevated line core. The Stokes I profile of the Ca II 8662 Å line also shows a nominal absorption profile with reduced intensity in the line wings. The line core intensity of the cyan-colored profile is similar to the quiet-Sun profile, whereas the line-core intenisty of the yellow-colored profile is lesser than the quiet-Sun profile. The Stokes V/I profile of the Hα line is typical with the amplitude of the Co I blend (3%) lesser than the amplitude of the Hα line (7%). As stated earlier, the Stokes V/I profile of the Ca II 8662 Å line is mixed with the magnetically sensitive Fe I 8661.8991 Å line, which appears as a blend. Consequently, the red lobe of the Fe I 8661.8991 Å overlaps with the blue lobe of the Ca II 8662 Å line. This overlap is particularly evident in the yellow-colored profile. The amplitude of the central lobe, influenced by both the Fe I 8661.8991 Å and Ca II 8662 Å lines, is significantly lower than the blue lobe of the Fe I 8661.8991 Å line. This is anticipated due to the contrasting signs of the Stokes V/I in the red lobe of the Fe I 8661.8991 Å line and the blue lobe of the Ca II 8662 Å line, when both the photosphere and chromosphere exhibit the same magnetic polarity, which in this case is negative. This effect is less noticeable in the cyan profile. The amplitude of the blue lobe of the Stokes V/I profile of the Ca II 8662 Å line is approximately 15% and 17% for the cyan- and yellow-colored profiles, respectively, while the amplitude of the central lobe is about 12% and 8%. The amplitude of the red lobe is about 10% and 16%.

The profiles colored brown and green correspond to pixels in the light bridge and penumbra, respectively. Both the Hα and Hα Stokes I and V/I profiles display typical absorption. The intensity in the far wings of the Hα and Ca II 8662 Å lines is either comparable to or exceeds that of the quiet-Sun profile. In both profiles, the amplitude of the Stokes V/I profile for the Co I blend is smaller than the dark umbral profiles previously discussed. The amplitude of the Stokes V/I profile for the green-colored penumbral profile is lower than all other profiles. For the brown- and green-colored profiles, the amplitude of the Stokes V/I profile of the Hα line is approximately 5% and 2.5%, respectively. The amplitude of the blue lobe of the Stokes V/I profile of the Ca II 8662 Å line is around 10% for the brown profile and 3% for the green profile, while the amplitude of the central lobe is about 7% for the brown profile and 4% for the green profile. The amplitude of the red lobe is about 9% for the brown profile and 6% for the green profile.

5.3 Methods

5.3.1 Weak field approximation

The magnetic field from the Hα spectral line was inferred using the weak field approximation (WFA). Under WFA the Stokes V is linearly related to B_{LOS} and $(\partial I/\partial\lambda)$ through (Landi Degl'Innocenti and Landolfi, 2004)

$$V(\lambda) = -\Delta\lambda_{\mathrm{B}}\, \bar{g} \cos\theta\, \frac{\partial I}{\partial \lambda}, \tag{5.1}$$

and

$$\Delta\lambda_{\mathrm{B}} = 4.67 \times 10^{-13} \lambda_0^2 B, \tag{5.2}$$

where $\Delta\lambda_{\mathrm{B}}$ is expressed in Å, B in Gauss, $\bar{g}$ is effective Landé factor, θ is the inclination of B with respect to the LOS, and λ_0 is the central wavelength of the spectral line (expressed in Å).

The B_{LOS} can be derived from Eq.5.1 using the linear regression formula (e.g., Martínez González and Bellot Rubio, 2009),

$$B_{\mathrm{LOS}} = -\frac{\Sigma_{\lambda} \frac{\partial I_{\smile}}{\partial \lambda} V(\lambda)}{C \Sigma_{\smile} (\frac{\partial I_{\smile}}{\partial \lambda})^2}, \tag{5.3}$$

where $C = 4.66 \times 10^{-13}\ \bar{g}\ \lambda_0^2$.

We have used $\bar{g} = 1.048$ following the investigation done by Casini and Landi Degl'Innocenti (1994). We derived two values of B_{LOS}, one from the line core (Hα ±0.15 Å), and over the line wing of the Hα line ([−1.5 Å, −0.15 Å] and [+0.15 Å, +1.5 Å]). The spectral blends listed in Table 5.1 were excluded while calculating B_{LOS} using the WFA, as have done by Mathur et al. (2023), Jaume Bestard et al. (2022) and Nagaraju, Sankarasubramanian, and Rangarajan (2020b). In this work, we used a spatially-coupled version of WFA developed by Morosin et al. (2020), which imposes spatial coherency in the WFA results.

λ_0 [Å]	$\Delta\lambda_0$ [Å]	Line
6562.44	0.05	V 2
6563.51	0.15	Co 1
6564.15	0.35	Unknown

Table 5.1: The first and second columns define the spectral blends removed before applying the WFA: $\lambda_0 \pm \Delta\lambda$. The third column indicates the element of the transition in case it is known.

5.3.2 Non-LTE inversions

The MPI-parallel STockholm inversion Code (STiC; de la Cruz Rodríguez et al., 2019; de la Cruz Rodríguez, Leenaarts, and Asensio Ramos, 2016), served as the tool for retrieving the stratification of atmospheric parameters. STiC builds upon a modified version of the RH radiative transfer code (Uitenbroek, 2001) and employs cubic Bezier solvers to solve the polarized radiative transfer equation (de la Cruz Rodríguez and Piskunov, 2013). In non-LTE, assuming statistical equilibrium, STiC has the capability to simultaneously fit multiple spectral lines. To address partial re-distribution effects (PRD), it integrates a fast approximation method (for more details Leenaarts, Pereira, and Uitenbroek, 2012). STiC adopts a plane-parallel geometry for intensity fitting in each pixel, commonly referred to as the 1.5D approximation. Furthermore, STiC utilizes an LTE equation-of-state derived from the library functions within the Spectroscopy Made Easy (SME) package code (Piskunov and Valenti, 2017). The atmospheric parameters are stratified using the optical depth scale at 5000 Å (500 nm), denoted as $\log \tau_{500}$.

We have inverted the Stokes I and V profiles of the Ca II 8662 Å and Fe I 8661.8991 Å lines simultaneously to infer the stratification of temperature (T), LOS velocity (V_{LOS}), microturbulence (V_{turb}) and LOS magnetic field (B_{LOS}). We used a 6-level Ca II atom. The Ca II IR lines were synthesized in complete re-distribution (CRD) approximation. The atomic parameters of the Fe I 8661.8991 Å line were obtained from Kurucz's line lists (Kurucz, 2011) and synthesized under LTE approximation. We employed k-means clustering to categorize the Stokes I profiles into distinct clusters based on similarity in shape, ensuring profiles with similar shapes were grouped together. Subsequently, we conducted inversions on the averaged profile within each cluster to infer the stratification of T, V_{LOS}, and V_{turb}. The inferred stratification then served as the initial atmospheric guess for determining the atmospheric parameters across the FOV, following a methodology akin to that employed by Mathur et al. (2023) and Mathur et al. (2022b). We note here that a total of 6 sets of nodes (not provided in tabular form) in T, V_{LOS}, and V_{turb} for a total of 30 clusters were used during the inversions. In the second cycle, we inverted the Stokes parameters using nodes only in the B_{LOS} at $\log \tau_{500} = -1$ and -4.5, respectively. Previous studies have demonstrated that perturbations in the B_{LOS} within the range of $\log \tau_{500} = -4$ to -5 elicit maximum responses in the Stokes V profiles of the Ca II 8662 Å line (Quintero Noda et al., 2016b; Joshi and de la Cruz Rodríguez, 2018; Murabito et al., 2019). In the third cycle, we used nodes in the T, V_{LOS}, V_{turb}, and B_{LOS} simultaneously to infer consistent values of the atmospheric parameters. Further, we have applied a median filter spatially over the atmospheric parameters at each cycle and re-ran the particular cycle, which resulted in not only a better fit of the Stokes parameters but also made the variation of the inferred atmospheric parameters spatially smoother. We have done this two to three times per cycle until we found a satisfactory fit of the Stokes parameters and spatially smooth variation of atmospheric parameters. Furthermore, we have inverted a few pixels that fail to converge separately, using different node positions and different initialization of atmospheric parameters. However, such pixels were fewer compared to the full FOV. The quality of fits of our inversions are described in appendix D.2. We set the average velocity in the darkest (left-most umbral substructure in panel (a) of Fig. 5.1) umbral region in the photosphere ($\log \tau_{500}$ range of $[-1, 0]$) to rest for the absolute velocity calibration.

5.4 Results

5.4.1 Non-LTE inversion results

In this section, we will discuss the results from the multi-line inversions of Stokes I and V profiles of the Ca II 8662 Å and Fe I 8661.8991 Å lines using the STiC inversion

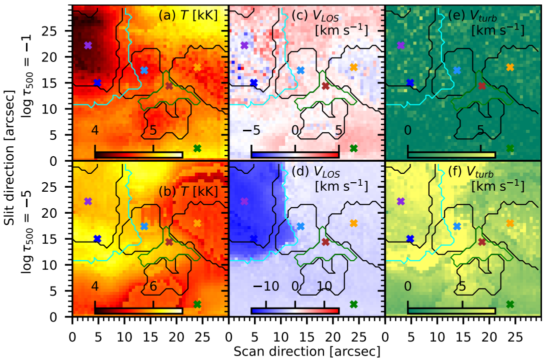

Figure 5.3: Maps of atmospheric parameters inferred from non-LTE simultaneous multi-line inversions. Panels (a) and (b) depict the maps of T at -1 and -5, respectively. Panels (c) and (d) show the maps of V_{LOS} at -1 and -5, respectively. Panels (e) and (f) display the maps of V_{turb} at -1 and -5, respectively. The contour color scheme is the same as that of in Fig. 5.1.

code. In Fig. 5.3, panels(a)–(f) show maps of T, V_{LOS} and V_{turb} at $\log \tau_{500} = -1$ and -5, as indicated in the figure.

The T map at $\log \tau_{500} = -1$ exhibits a morphology akin to the far wing image of the Ca II 8662 Å line. In this map, the darkest umbral areas display temperatures around 4 kK, while the majority of the umbra is characterized by a slightly higher T, approximately 4.5 kK. The light-bridge area presents a marginally increased T, about 4.8 kK, in contrast to the penumbral region, which exhibits T of 5 kK or higher. Conversely, the T map at $\log \tau_{500} = -4.5$ shows a morphology comparable to the line core image of the Ca II 8662 Å line. Notably, the temperature in the right-most umbral region is lower than in other umbral areas, a characteristic also observed in the line core image of the Ca II 8662 Å line, where this region appears the darkest. In the vicinity of the left-most umbral region, where the Ca II 8662 Å line core is in emission, a higher T, compared to the rest of the FOV, is seen, around 6.5 kK, a signature of heating. The lightbridge indicates a T of approximately 6 kK.

In the V_{LOS} map at $\log \tau_{500} = -1$, the umbral region is predominantly static, exhibiting minimal blue or redshifts. The lightbridge area demonstrates very low downflow velocities, approximately +1–2 km s^{-1}. The penumbral region, on the other hand, displays downflows in the range of +2–3 km s^{-1}. In contrast, the V_{LOS} map at $\log \tau_{500} = -4.5$ reveals upflows around -5 km s^{-1}. Notably, in areas where heating is seen. i.e., the Ca II 8662 Å line is in emission, the upflow velocities exceed -10 km s^{-1}.

There is negligible V_{turb} at $\log \tau_{500} = -1$, whereas at $\log \tau_{500} = -4.5$, there is significant V_{turb} of about 5–8 km s^{-1}.

Panels (a) of Fig. 5.4 depicts magnetic field map inferred from non-LTE inversions at $\log \tau_{500} = -1$. Panel (a) of Figure 5.5 shows the scatter plots between the magnetic field inferred at $\log \tau_{500} = -1$ and the HMI magnetogram. The morphological structure of the magnetic field inferred at $\log \tau_{500} = -1$, panel (a), is similar to that of the HMI magnetogram, panel (f) of Fig. 5.1, with comparable magnetic field strength.

The correlation coefficient between B_{LOS} at $\log \tau_{500} = -1$ and B_{LOS} from HMI is of 0.7 and 0.8, for umbral and penumbral regions, respectively, with an overall coefficient of 0.88. The corresponding slopes are 0.98 and 0.7, with an overall slope of about 0.78. Notably, there is no correlation between the field strength in lightbridge regions. It could be because the area of the lightbridge, in terms of the number of pixels, is very small for any meaningful correlation. It also appears that the field strength from inversions is larger than that of HMI in almost all the pixels in the lightbridge region. There is a spatial straylight contamination in the data, which is not corrected. Thus, the stronger fields in the umbral regions near the lightbridge may have some contribution to the fields inferred from the lightbridge region. Overall, the contribution of the spatial straylight and the seeing-induced spatial smearing could explain the scatter in the magnetic field values and why we could not achieve a one-to-one match with the HMI magnetogram. The high correlation values found between the field strengths inferred from the data acquired using the polarimeter at the KTT with the standard space-based instruments like HMI suggests that the data acquisition, reduction procedures, and further inversion methods are correctly applied.

Panel (b) of Fig. 5.4 shows the map of the magnetic field inferred from the inversions at $\log \tau_{500} = -4.5$. The magnetic field strength and morphology in the umbral regions are similar to the photospheric fields, panel (a). This can be further verified by examining the panel (b) of Fig. 5.5. The field strength of the penumbral region at $\log \tau_{500} = -4.5$ is weaker by a factor of 0.39 than that of at $\log \tau_{500} = -1$. Whereas, the field strength of lightbridge region is negatively correlated by a factor of -0.14. The emission region has a slope of 0.6, however, the field strengths in the emission region are higher at $\log \tau_{500} = -4.5$ than that of at $\log \tau_{500} = -1$.

The variation of the mean B_{LOS} inferred from the inversions and the WFA along a slit (2-pixel width) drawn over the lightbridge in Fig. 5.4 is shown in Fig. 5.6. The field strength inferred from inversions at $\log \tau_{500} = -1$ in the lightbridge is smaller by about 400 G compared to the umbral region with a stronger field. Whereas, the field strength inferred from the WFA over Hα ± 1.5 Å is smaller by about 300 G. The field strength at the $\log \tau_{500} = -4.5$ shows no significant behavior of increase or decrease at the lightbridge compared to the surrounding umbral region. Whereas, the field strength inferred from the WFA over Hα ± 0.15 Å shows a decrease of about 300 G.

5.4.2 Comparison of the B_{LOS} inferred from the non-LTE inversions and WFA of the Hα line

Panels (c) and (d) of Fig. 5.4 show the maps of the B_{LOS} inferred from the WFA of the Hα over the line wing, [-1.5 Å, -0.15 Å] and [$+0.15$ Å, $+1.5$ Å] and the line core, ± 0.15 Å, respectively. This has been done because in the earlier study, Mathur et al. (2023), it was found that the WFA over the full Hα line shows photospheric magnetic morphology, whereas the core of the Hα line samples the chromospheric

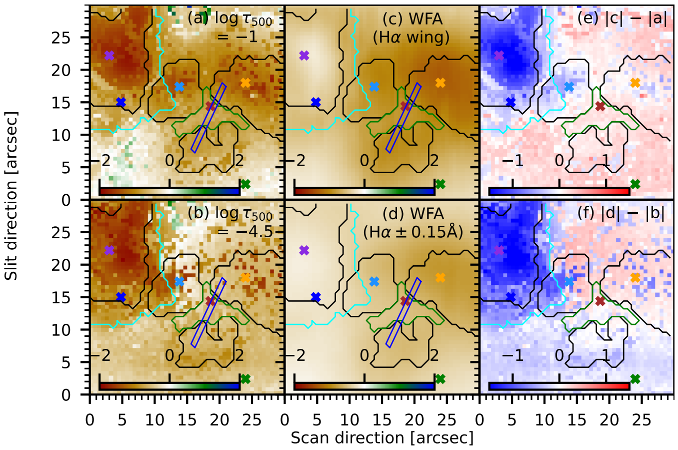

Figure 5.4: Maps of B_{LOS} inferred from the inversions and the WFA. Panels (a) and (b) show the maps of B_{LOS} at $\log\tau_{500} = -1$ and -4.5, respectively. Panels (c) and (d) show the maps of B_{LOS} inferred from the WFA of the Hα line over the line wings, [−1.5 Å , −0.15 Å] and [+0.15 Å , +1.5 Å] and the line core, ±0.15 Å , respectively. Change in the stratification of the $|B_{\mathrm{LOS}}|$ is shown in the rightmost two panels (e) and (f) as indicated on each panel. The unit of B_{LOS} is kG. The contour color scheme is the same as that of in Fig. 5.1. A blue-colored slit (2-pixel width) is drawn over the lightbridge area which is further discussed in the text.

magnetic field. Panels (e) shows the difference in the magnitude between panels (a) and (c) while panel (f) shows the difference in magnitude between panels (b) and (d). Panel (c) and (d) of Fig. 5.5 show the scatter plots between the B_{LOS} inferred from WFA with that of inversions. Panel (e) of Fig. 5.5 shows the comparison between the B_{LOS} inferred from the WFA over the Hα line wing with that inferred from the line core. Panel (f) compares the B_{LOS} inferred from the inversions at $\log\tau_{500} = -1$ with that of inferred from WFA over the Hα line core.

The field strength inferred from the WFA over the line wings of the Hα line is larger than that of inversions at $\log\tau_{500} = -1$ everywhere in the FOV except in the regions where there is an emission feature in the core of the Ca II 8662 Å and the Hα lines and small regions of umbra and penumbra. However, the scatter plots show, panel (c) of Fig. 5.5, that the slope between the WFA and the inversions is less than 1. The reason for the increased field strengths is the offset in the linear fit. The field strength inferred from the WFA over the line wings of the Hα line in the umbral region, which does not have an emission feature, penumbral region, and the lightbridge has a slope of about 0.5 with respect to that inferred from inversions at $\log\tau_{500} = -1$. The field strength from the WFA in the region with emission is negatively correlated (−0.49) with that of inferred at $\log\tau_{500} = -1$. Whereas, the full umbra is negatively correlated by a factor of −0.37.

Similar to $\log\tau_{500} = -1$, the field strength inferred from the WFA over Hα ±0.15 Å is smaller than that of inferred from inversions at $\log\tau_{500} = -4.5$ in the region with the emission feature. Additionally, a large portion of the penumbral region and one of

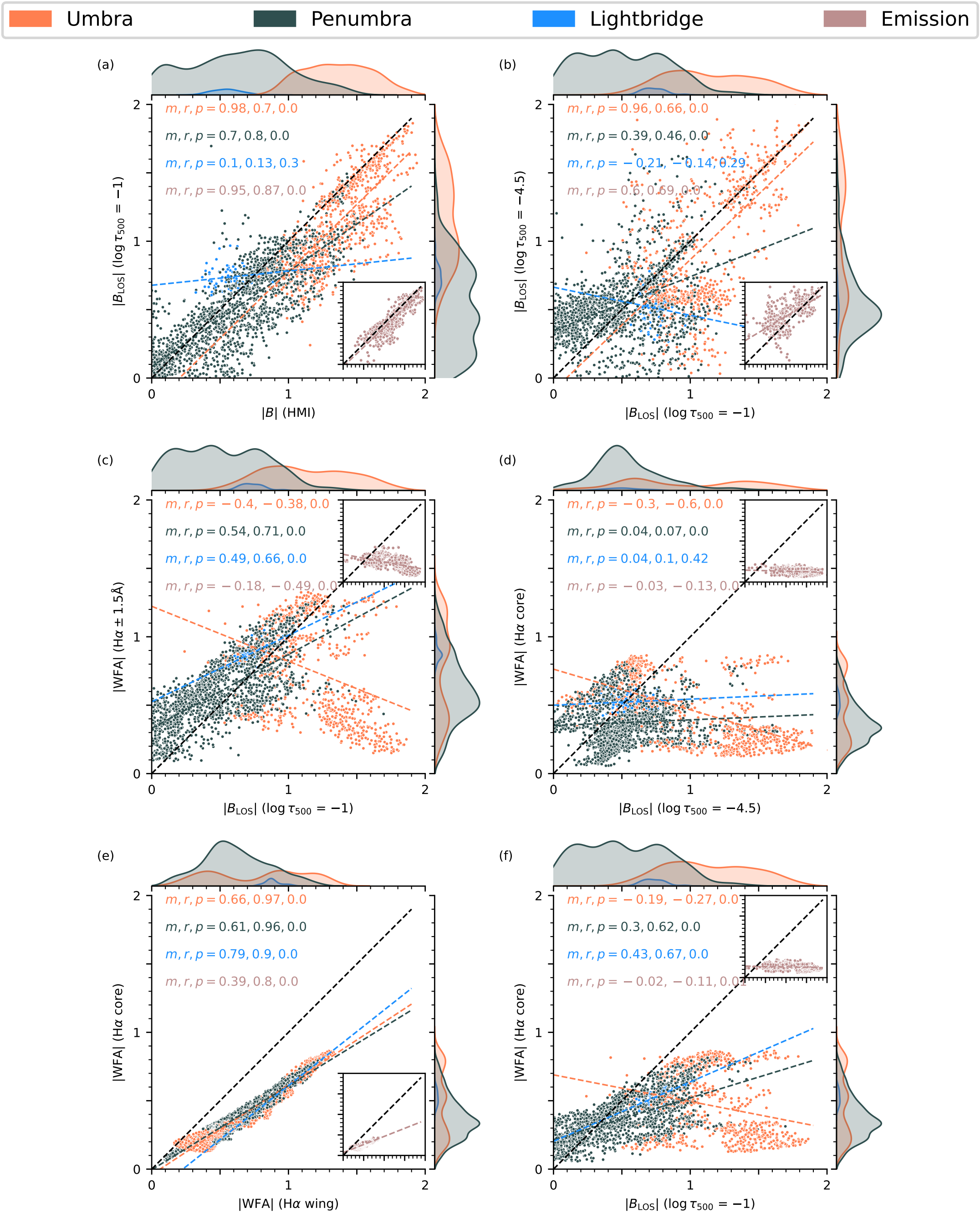

Figure 5.5: Comparison of the magnitude of B_{LOS} inferred from inversions and the WFA. Panel (a) shows the comparison between the B_{LOS} from the HMI magnetogram with that of inferred from inversions at $\log \tau_{500} = -1$. Panel (b) compares between the B_{LOS} inferred from the inversions at $\log \tau_{500} = -1$ with that of at $\log \tau_{500} = -4.5$. Panel (c) shows the comparison between the B_{LOS} inferred from inversions at $\log \tau_{500} = -1$ with that of inferred from WFA of the Hα line over the line wings ([-1.5 Å, -0.15 Å] and [$+0.15$ Å, $+1.5$ Å]). Panel (d) compares between the B_{LOS} inferred from inversions at $\log \tau_{500} = -4.5$ with that of inferred from WFA of the Hα line within the spectral range ± 0.15 Å. Panel (e) compares the B_{LOS} inferred from the WFA over the Hα line wings with that of inferred from the line core. Panel (f) compares the B_{LOS} inferred from inversions at $\log \tau_{500} = -1$ with that inferred from WFA over Hα line core. The unit of the B_{LOS} is kG. Scatter plots for different regions of the FOV are color-coded and detailed in the legend. Since the emission region contains some part of the leftmost umbral and penumbral region, it is shown separately in the inset plots. The slopes, Pearson correlation coefficient and the p-value of the scatter plot(s) are indicated in the plots by m, r, and p, respectively. The magnetic field inferred using the KTT data at $\log \tau_{500} = -1$ is 0.78 times of HMI magnetogram with $r = 0.88$ and $p = 0$.

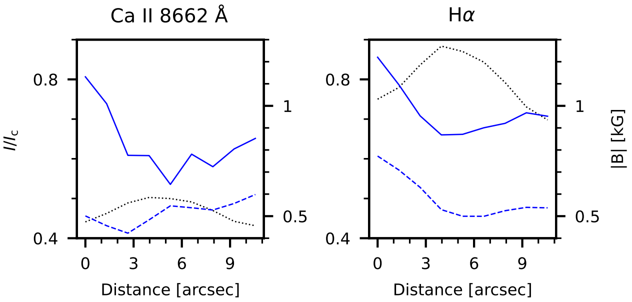

Figure 5.6: Variation of the magnetic field along the slit drawn in Fig. 5.4. The slit width is 2-pixels and all quantities shown are mean within the slit width. The continuum intensity is represented by gray color, and the photospheric and chromospheric magnetic field is represented by solid and dashed curves, respectively.

the umbral substructures also show smaller field strengths. The scatter plot, panel (d) of Fig. 5.5, shows that the field strengths inferred from the WFA over Hα ±0.15 Å and from inversions at $\log \tau_{500} = -4.5$ are uncorrelated. However, the majority of the FOV shows smaller field strengths from the WFA than that of inversions. Interestingly, the morphological structure of the magnetic fields, as inferred from the WFA over the Hα ±0.15 Å range, exhibits similarities with those inferred from the line wings of the Hα line, see panels (c) and (d) of Fig. 5.4. The fields inferred from the Hα line core are lesser, however correlated with that of inferred from the line wings. Notably, the emission region shows a lesser slope (0.39) and correlation coefficient (0.8) compared to the whole umbral and penmbral regions, which have a slope of about 0.6 and correlation coefficient of about 0.96, see panel (e) of Fig. 5.5. The scatter plot of the $|B_{\rm LOS}|$ inferred from the WFA from the Hα line core appears similar with that of inversions at $\log \tau_{500} = -4.5$ and -1, see panels (d) and (f) of Fig. 5.5. In panel (f), with respect to panel (d), the slope and correlation coefficient is lesser in umbral regions, and higher for penumbral and lightbridge regions. Interestingly, the slope and correlation coefficient remained same for the emission regions in both the panels (d) and (f).

5.5 Discussion

In this paper, we present spectropolarimetric observations of an active region recorded simultaneously in the Hα and Ca II 8662 Å lines. The stratification of the $B_{\rm LOS}$ is inferred through multiline inversions of the Ca II 8662 Å-and-Fe I 8661.8991 Å lines and the WFA over the Hα line.

Consistent with Mathur et al. (2023), we find that the field strengths inferred from the Hα line core are smaller than that inferred from inversions at $\log \tau_{500} = -4.5$. Since the opacity of the Hα line is determined by mass density, (Carlsson and Stein, 2002; Leenaarts, Carlsson, and Rouppe van der Voort, 2012), and the reasonable assumption that magnetic field expands with height, it is possible that the Hα line is sampling magnetic field at higher heights than that of the Ca II 8662 Å line. It is also to note that in the region with emission feature, the morphology of the magnetic field at $\log \tau_{500} = -4.5$ is remarkably similar to that of at $\log \tau_{500} = -1$, and the field strength is also slightly higher or comparable to that of at $\log \tau_{500} = -1$. This can be clearly seen in the panel(b) of Fig. 5.4 and 5.5. It has been found in earlier studies that during events when there is a rise in temperature in the chromosphere, the Ca II gets ionized to Ca III, and thus, the Ca II triplet lines may sample deeper layers of the solar atmosphere (Kerr et al., 2016; Kuridze et al., 2018; Bjørgen et al., 2019). In contrast, the field strength inferred in the emission feature from the WFA over the Hα line core is near constant about 300 G, panel (d) of Fig. 5.5. The near-constant field strength and the fact that it is much less than the magnetic field inferred from the inversions shows that the field is diffused and the Hα line is indeed sampling higher heights than the Ca II 8662 Å line in the region with emission feature. This is in agreement with the study done by Bjørgen et al. (2019), that the Hα line retains opacity in active regions with heating activity. There is also a good agreement with the field strengths at $\log \tau_{500} = -1$ with that inferred from WFA over Hα full spectral range, except in the region with emission feature, panel (c) of Fig. 5.5. In addition, the fields inferred in the emission region from the WFA over Hα ±0.15 Å and the line wings of the Hα line are morphologically similar. Thus, it is possible that in the case of heating events, the full Hα line becomes sensitive to the chromospheric magnetic field instead of only the line core. We note here that although the fields inferred from the Hα line wings and the line core seem correlated, as seen in panel (e) of Fig. 5.5, the similarity of the panel (f) with panel (d) of Fig. 5.5, showing near-zero slopes suggest that the Hα line core primarily have contribution from the higher atmospheric layers. Moreover, the emission region is similarly uncorrelated in both the scatterplots.

The WFA over the core of the Hα line has no correlation with that inferred from inversions at $\log \tau_{500} = -4.5$. In our earlier study, Mathur et al. (2023), we found that the fields inferred from the Hα line and the inversions of the Ca II 8542 Å line were correlated. We provide the following reasons for the lack of correlation in this study. The field strengths in the earlier study were small, $\leq$600 G, whereas this study focuses on an active region with field strengths of about 2000 G. It may be possible that the WFA method has a lot of systematic errors in these field ranges. The validity of the WFA of the Hα line is not yet quantified using studies based on realistic rMHD simulations. Additionally, in the earlier study, the spectral profile of pore and surrounding quiet region were simpler compared to this study which has a large sunspot with multiple structures and a large region that shows emission features in the Hα and Ca II 8662 Å data, and thus complex spectral profiles. It may also be possible that there may be systematic errors in the magnetic field inferred in the inversions at $\log \tau_{500} = -4.5$ due to the presence of the Fe I 8661.8991 Å line, which appears as a blend very close to the core of the Ca II 8662 Å line. There could be a degeneracy between atmospheric parameters that fit the blend as an absorption profile of the Fe I 8661.8991 Å line vs an emission feature blueward to the line core of the Ca II 8662 Å line. The gradients in the LOS magnetic field and velocity could contribute to the errors retrieved in the B_{LOS} from the WFA over the Hα line. Using semi-empirical models and realistic rMHD simulations that gradients in the LOS velocity and magnetic field introduce errors in the inferred fields from the WFA of the Ca 2 8498 and 8542 Å lines (Centeno, 2018; Kawabata et al., 2024). However, in this study, we suggest that only the effect of magnetic field gradients be a significant factor in the uncertainties in the fields inferred from the WFA of the Hα line. This is because we have found that velocity gradients in the Hα data, calculated using the bisector method and not discussed in the paper, are less than 1 km s^{-1} and thus not significant. The $|B_{\mathrm{LOS}}|$ inferred from the full spectral range of the Hα line in all FOV except emission region is weaker by a factor of about 0.6 than that of B_{LOS} at $\log \tau_{500} = -1$, which is slightly larger than the previous studies (0.42) (Abdussamatov, 1971; Balasubramaniam, Christopoulou, and Uitenbroek, 2004; Hanaoka, 2005; Nagaraju, Sankarasubramanian, and Rangarajan, 2008; Mathur et al., 2023).

The magnetic field strength within the lightbridge, as inferred from inversions at $\log \tau_{500} = -1$, is observed to be smaller by about 400 G compared to surrounding umbral fields. This finding contrasts with earlier studies indicating that lightbridges typically exhibit magnetic field strengths about 1 kG lower than the surrounding umbral fields (Rimmele, 1997; Berger and Berdyugina, 2003; Jurčák, Martínez Pillet, and Sobotka, 2006; Rimmele, 2008; Sobotka et al., 2013; Lagg et al., 2014; Joshi et al., 2017). The discrepancy in our measurements may be attributed to factors such as spatial straylight, which remains uncorrected in this study, and seeing-induced smearing. Additionally, analysis reveals that the magnetic field in the lightbridge at $\log \tau_{500} = -4.5$ does not exhibit a significant difference from the surrounding umbral region, aligning with findings from Joshi et al. (2017) and Rueedi, Solanki, and Livingston (1995), but contradicting the results of Schad et al. (2015), who reported lower magnetic field values in the chromosphere at lightbridge locations. Notably, magnetic field strength inferred from the Hα line within the lightbridge displays lower values compared to surrounding umbral regions, consistent across both the photosphere (using the full spectral range) and the chromosphere (utilizing the line core).

The heating region displays notable upflows reaching approximately -10 km s^{-1}, potentially indicative of chromospheric evaporation. Prior observational investigations (for eg. Díaz Baso, de la Cruz Rodríguez, and Leenaarts, 2021; Yadav et al., 2021; Libbrecht et al., 2019; Berlicki et al., 2008; Falchi and Mauas, 2002) and studies based on rMHD simulations (Cheung et al., 2019; Kerr et al., 2016) have documented instances of chromospheric evaporation. However, the inferred velocities within the heating region may not be reliable due to the absence of corresponding features in the spectral profiles of the Hα line. No asymmetries or line shifts are discernible in the Stokes I profiles of the Hα line. Thus, it is possible that the inversion code utilized these high velocities to fit the observed asymmetry in the two minima on either side of the emission peak of the Stokes I profiles of the Ca II 8662 Å line.

5.6 Conclusions

This study presents the stratification of the chromospheric magnetic field using spectropolarimetric observations of an active region in the Ca II 8662 Å and Hα lines recorded simultaneously. In agreement with the Mathur et al. (2023), we found that the magnetic field inferred from the Hα line core is consistently smaller than that inferred from inversions of the Ca II 8662 Å line at $\log \tau_{500} = -4.5$. The magnetic field morphology inferred from the core of the Hα line resembles that inferred from the full spectral range of the Hα line in the heating region. The field strength and morphology inferred in the heating region from the inversions at $\log \tau_{500} = -4.5$ is comparable to that of at $\log \tau_{500} = -1$. In the heating region, at $\log \tau_{500} = -4.5$, inversions revealed upflows greater than -10 km s^{-1}, whereas signatures of such high upflows were not evident in the Hα line spectra. In contrast to the earlier study, Mathur et al. (2023), we found no correlation between the fields inferred from the core of the Hα line and from inversions at $\log \tau_{500} = -4.5$. The current study and Mathur et al. (2023) highlights the potential of the spectropolarimetric observations of the Hα line recorded simultaneously with the lines of Ca II to study the stratification chromospheric magnetic field. Further spectropolarimetric observations of the Hα line recorded simultaneously with other chromospheric diagnostics such as Ca II 8542 Å and He I 10830 Å lines utilizing telescopes with superior spatial and spectral resolution like the Daniel K. Inouye Solar Telescope (DKIST; Rimmele et al., 2020) and the forthcoming European Solar Telescope (EST; Collados et al., 2013) and the National Large Solar Telescope (NLST; Hasan, 2010) are necessary for a comprehensive understanding of the stratification of the chromospheric magnetic field.

Chapter 6

Summary and outlook

Simultaneous magnetic field measurements at multiple heights within the solar atmosphere are crucial for unraveling the complex mechanisms driving mass and energy transfer to the corona as well as the generation of the solar wind. This thesis presents the inference of stratification of magnetic fields from the photosphere to the mid to the upper chromosphere using the simultaneous multiline spectropolarimetric technique. This technique is very useful to probe magnetic fields at multiple heights in the solar atmosphere. In this context, we have surveyed current diagnostics such as the Ca II 8542 Å line and He I 10830 Å line to probe the chromospheric magnetic field. We have also identified the limitations of current diagnostics and positioned the Hα line as a good chromospheric diagnostic. Towards this goal, we have compared the magnetic field inferred from the Hα line with that of the widely used chromospheric line, Ca II 8542 Å line, and summarized in section 6.1.1. However, the study was limited to a small pore. To obtain further spectropolarimetric observations of the Hα line, we have enabled the Kodaikanal Tower Tunnel Telescope to record spectropolarimetric observations with a tip-tilt system operational for a minimum duration of 1 hr. An image autoguider system is installed as a precursor to the tip-tilt system, as summarized in section 6.1.2. The tip-tilt system and its impact in reducing the seeing-induced cross-talk in polarization measurements is summarized in section 6.1.3. Further, the said system is used to record simultaneous spectropolarimetric observations in Hα and Ca II 8662 Å lines. We have presented the observations taken on 27th May 2023 of an active region, NOAA 13315, close to the disc center and inferred the stratification of the magnetic field from the photosphere to the chromosphere. The magnetic field is inferred from non-LTE inversions of Ca II 8662 Å line and WFA of Hα line. This study is summarized in section 6.1.4.

6.1 Summary

6.1.1 Chapter 2

The Hα line is one of the most widely used spectral lines to study the solar chromosphere. However, polarimetric studies to infer the magnetic fields are sparse. One of the reasons could be that it has been shown using 1-D radiative transfer calculations that the photospheric magnetic fields have a significant contribution to the Hα Stokes V profiles. Recent works, however, have revealed that 3-D radiative transfer is necessary to model the Hα line core, though the works have only modeled the Stokes I. In this context, we explored the potential of the Hα Stokes V profiles in inferring the chromospheric magnetic field using simultaneous spectropolarimetric observations of the Hα and the Ca II 8542 Å lines obtained from the SPINOR instrument of the DST. We analyzed the topology and the strength of the LOS magnetic field (B_{LOS}) inferred from the weak field approximation (WFA) of the Hα line and compared it with the inversions of the Ca II 8542 Å line. We found that the map of the B_{LOS} inferred from the WFA of the Hα line core (±0.35 Å) shows morphology similar to that of at the chromospheric layers ($\log \tau_{500} = -4.5$). The map of the B_{LOS} from the WFA about the line wings ([−1.5, −0.6] and [+0.6, +1.5] Å) and the full spectral range (±1.5 Å) shows morphology similar to that of at the photospheric layers ($\log \tau_{500} = -1$). At the location of a pore we observed that the field strengths ($|B_{\mathrm{LOS}}|$) inferred from the WFA about the Hα line core are weaker than those obtained at $\log \tau_{500} = -4.5$ through the inversions of the Ca II 8542 Å line. Our results suggest that $|B_{\mathrm{LOS}}|$ retrieved with the WFA applied to the Hα line core is from higher chromospheric layers compared to that retrieved using the inversions of the Ca II 8542 Å line, or, the $|B_{\mathrm{LOS}}|$ retrieved with the WFA over the Hα line core is systematically underestimated.

6.1.2 Chapter 3

The Kodaikanal Tower Tunnel Telescope system has a 3-mirror Coelostat placed in the tower as a light feeding system. The Coelostat is an equatorial mount that must be aligned such that the polar axis has an altitude equal to the latitude of the place and must be parallel to the local longitude. However, a few arcsecond misalignments will cause an image drift in East-West (E-W) and North-South (N-S) axes. The image drifts measured at KTT are variable with time with a maximum recorded value of about ~ 7 arcsec minute^{-1} close to noon. Due to this drift, potential tip-tilt systems can only work for a limited time due to the limit of the stroke of the actuator. An image Auto Guider system has recently been installed at KTT to arrest the image drift based on sensing the image limb. The image's limb position on the image plane is sensed using a two-segment photodiode sensor in North–South, and East–West directions. Feedback is given to the second mirror of Coelostat, which tilts, causing the image to move on the image plane. The Auto Guider system is robust and capable of arresting image drifts up to 55 arcsec minute^{-1} with a precision of ±0.9 arcsec.

6.1.3 Chapter 4

We have conducted measurements of seeing-induced cross-talk using spectropolarimetric observations of sunspots captured simultaneously in the Hα and Ca II 8662 Å lines with the Kodaikanal Tower Tunnel (KTT) telescope. The KTT telescope is equipped with an integrated image stabilization system comprising a tip-tilt and autoguider system. Furthermore, the spectropolarimeter at KTT has been upgraded to enable simultaneous recording of spectropolarimetric observations across three spectral lines. Our analysis reveals that the tip-tilt system, which operates with a cut-off frequency of 80 Hz, effectively reduces seeing-induced cross-talk in the measured Stokes parameters at least by a factor of 2.

6.1.4 Chapter 5

As discussed in chapters 3 and 4, we have upgraded the Kodaikanal Tower Tunnel Telescope to record spectropolarimetric observations simultaneously in three spectral lines with a tip-tilt system operational. This was done with the goal of recording observations of active regions in the Hα and Ca II 8662 Å lines simultaneously. In this chapter, we presented an analysis of one such observation of a sunspot, NOAA 13315, recorded on 27th May 2023, using state-of-the-art non-LTE inversions and weak field approximation methods. The sunspot exhibits multiple structures, viz., 4 umbras, a lightbridge, and a region where Ca II 8662 Å line core is in emission. The Hα line core image also displays brightening in the emission region, a signature of localized heating, with the spectral profiles showing elevated line cores. In agreement with the study presented in chapter 2, we found that the magnetic field inferred from the Hα line core is consistently smaller than that inferred from inversions of the Ca II 8662 Å line at $\log\tau_{500} = -4.5$. The field strength and morphology inferred in the heating region from the inversions at $\log\tau_{500} = -4.5$ is comparable to that of at $\log\tau_{500} = -1$. In the heating region, at $\log\tau_{500} = -4.5$, inversions revealed upflows greater than -10 km s^{-1}, whereas signatures of such high upflows were not evident in the Hα line spectra. In contrast to the earlier study, we found no correlation between the fields inferred from the core of the Hα line and from inversions at $\log\tau_{500} = -4.5$. The magnetic field morphology inferred from the core of the Hα line is also similar to that inferred from the full spectral range of the Hα line in the emission region. The field strength inferred in the lightbridge at $\log\tau_{500} = -1$ is smaller than the surrounding umbral regions and comparable at $\log\tau_{500} = -4.5$. Similarly, the field strength inferred in the lightbridge from the WFA over the Hα line appears lower compared to the surrounding umbral regions.

6.2 Novelty of the thesis

This thesis has the following novel aspects:

- **Instrumentation at the KTT:** Detailed in chapters 3 and 4, the KTT has been upgraded to record spectropolarimetric observations in three spectral lines simultaneously. This upgrade also included equipping the KTT with an image stabilization system consisting of an autoguider and a tip-tilt system. Three new cameras have been installed; Kinetix from Teledyne (red optimized), Orca Quest from Hamamatsu (IR optimized and etaloning de-sensitized) are installed at the spectroscopic focal plane, and C-Blue One from Firstlight Imaging is used as the imaging camera in the tip-tilt system. The polarizing optics in the polarimeter are also upgraded to allow for simultaneous observations in the Hα and Ca II 8662 Å lines. Using this system, simultaneous spectropolarimetric observations in the Hα and Ca II 8662 Å were recorded with and without the tip-tilt system. It is concluded that the tip-tilt system performs with a cut-off frequency of 80 Hz and reduces the seeing-induced cross-talk at least by a factor of 2.

- **Investigating the diagnostic potential of the Hα line to probe the chromospheric magnetic field:** The Hα line is used as a candle to investigate solar chromosphere and its energetic events like filaments, Ellerman bombs, surges, flares and spicules. These events have distinct spectral signatures that get imprinted on the Hα intensity profiles, which are then used for target classification and the study of fine-structure and temporal evolution of the chromosphere. However, the polarimetric studies of the Hα line are rare. The reason could be that it is very difficult to interpret the polarization profiles of the Hα line. For example, in an earlier study, it has been shown using 1-D radiative transfer calculations that the photospheric magnetic fields have a significant contribution to the Hα Stokes V profiles. Recent works, however, have revealed that 3-D radiative transfer is necessary to model the Hα line core, though the works have only modeled the Stokes I. Using simultaneous spectropolarimetric observations of the Hα line with widely used chromospheric lines such as Ca II 8542 Å (and Ca II 8662 Å) line, we have investigated whether the Hα line probes the chromospheric magnetic field. Toward this goal, we have utilized state-of-the-art non-LTE inversions and weak field approximation methods. The studies detailed in chapters 2 and 5 conclude that the Hα line core always probes the chromospheric magnetic field, which is at higher heights than probed by the Ca II IR triplet. In case of heating events, full Hα line becomes sensitive to the chromospheric magnetic field. Thus, for a comprehensive understanding of the stratification of the chromospheric magnetic field, especially when highest spatial and spectral resolution observations from telescopes like Daniel K. Inouye Solar Telescope and the forthcoming European Solar Telescope and the National Large Solar Telescope are imminent, this thesis emphasizes the need of further spectropolarimetric observations of the Hα line simultaneously recorded with other chromospheric diagnostics such as the Ca II 8542 Å line and / or He I 10830 Å line.

6.3 Future work

We discuss the future work in terms of instrumentation and potential observations:

- **Scope in the upgrade of the KTT:** The autoguider system currently installed works by moving the motors of mirror M2 of the 3-mirror coelostat of the KTT. It has been found that whenever the M2 is moved, it introduces pronounced oscillations on the image plane, making it challenging for the tip-tilt system to work efficiently. If these oscillations are arrested, the tip-tilt system can work at a higher cut-off frequency of 110 Hz instead of the current 80 Hz. Further, the image stabilization system can be upgraded with the inclusion of a low-order adaptive optics system. Also, the tip-tilt system is currently integrated as part of the polarimeter system, which sits perpendicular to the f/96 beam coming from the achromatic doublet. Thus, the beam has to be tilted to arrive at openings in the polarimeter. A detailed layout of the polarimeter and tip-tilt system is provided in chapter 4. Because of this requirement of tilting the beam, the achromatic doublet is not fully illuminated, and thus, there is a decrease in the throughput of the telescope as a whole. A new optical design is required where the beam tilting is not required either for the polarimeter or for the selection of a field of view to observe. Further, the polarimeter setup is currently unable to discern the Stokes Q and U signals from the cross-talk arising from the instrumental effects. Thus, a detailed study of instrumental polarization is also required for linear polarization observations. The polarimeter is based on the rotating waveplate design. Thus, even though cameras with fast frame rates are installed, the observer cannot record spectropolarimetric observations with fast modulation frequency. This slow modulation frequency introduces seeing-induced cross-talk in the polarization measurements. Thus, the polarimeter design can be upgraded by replacing the rotating waveplates with liquid crystal variable retarders (LCVRs) or ferroelectric liquid crystals (FLCs) based design. The retardance of the LCVRs and FLCs can be changed much faster and thus can enable spectropolarimetric measurements with fast modulation frequency.

- **Potential observations from the KTT:** The KTT telescope is ready to record spectropolarimetric observations in three spectral lines simultaneously with a tip-tilt system operational. As long as the dispersion between the two lines is less than 46 cm, observations in the two lines can be recorded simultaneously. More studies of active regions using simultaneous observations in the Hα and Ca II 8662 Å lines can be undertaken. The system can also be used to record simultaneous observations in Hβ 4861 Å (4th order of the grating) and the Hα (3rd order of the grating) lines simultaneously, with a dispersion of approximately 41 cm. The polarimetric studies in the Ca II K (3rd order of the grating) can also be undertaken simultaneously with Fe I 5250 Å and Mg I b2 5172 Å (4th order of the grating) lines, with a dispersion of 3 cm and 30 cm, respectively. After the upgrades mentioned in the previous bullet point for the KTT are completed, polarimetric studies with a faster cadence would also be feasible.

Bibliography

Abdussamatov, H.I.: 1971, On the Magnetic Fields and Motions in Sunspots at Different Atmospheric Levels. *SoPh* **16**, 384. DOI. ADS.

Alfvén, H.: 1947, Magneto hydrodynamic waves, and the heating of the solar corona. *Mon. Not. Roy. Astron. Soc.* **107**, 211. DOI. ADS.

Andretta, V., Jones, H.P.: 1997, On the Role of the Solar Corona and Transition Region in the Excitation of the Spectrum of Neutral Helium. *ApJ* **489**, 375. DOI. ADS.

Aschwanden, M.J.: 2005, *Physics of the Solar Corona. An Introduction with Problems and Solutions (2nd edition)*. ADS.

Asensio Ramos, A., Trujillo Bueno, J., Landi Degl'Innocenti, E.: 2008, Advanced Forward Modeling and Inversion of Stokes Profiles Resulting from the Joint Action of the Hanle and Zeeman Effects. *ApJ* **683**, 542. DOI. ADS.

Avrett, E.H.: 1985, Recent thermal models of the chromosphere. In: Lites, B.W. (ed.) *Chromospheric Diagnostics and Modelling*, 67. ADS.

Bagare, S.P.: 1985, Solar flare of 1982 April 14. *Bulletin of the Astronomical Society of India* **13**, 394. ADS.

Bagare, S.P., Gupta, S.S.: 1998, On the relation between magnetic field strength and Wilson depression in sunspots. *Bulletin of the Astronomical Society of India* **26**, 197. ADS.

Balasubramaniam, K.S., Christopoulou, E.B., Uitenbroek, H.: 2004, Promises and Pitfalls of Solar Hα Zeeman Spectropolarimetry. *ApJ* **606**, 1233. DOI. ADS.

Bappu, M.K.V.: 1967, Solar Physics at Kodaikanal. *SoPh* **1**, 151. DOI. ADS.

Beck, C., Choudhary, D.P.: 2019, Magnetic Properties and Flow Angle of the Inverse Evershed Flow at Its Downflow Points. *ApJ* **874**, 6. DOI. ADS.

Beck, C., Schmidt, W., Rezaei, R., Rammacher, W.: 2008, The signature of chromospheric heating in Ca II H spectra. *Astron. Astrophys.* **479**, 213. DOI. ADS.

Beckers, J.M.: 1968, Solar Spicules (Invited Review Paper). *Solar Phys.* **3**, 367. DOI. ADS.

Beckers, J.M.: 1972, Solar Spicules. *Annurev.aa.* **10**, 73. DOI. ADS.

Beckers, J.M., Milkey, R.W.: 1975, The Line Response Function of Stellar Atmospheres and the Effective Depth of Line Formation. *SoPh* **43**, 289. DOI. ADS.

Bellot Rubio, L., Orozco Suárez, D.: 2019, Quiet Sun magnetic fields: an observational view. *Living Reviews in Solar Physics* **16**, 1. DOI. ADS.

Berger, T.E., Berdyugina, S.V.: 2003, The Observation of Sunspot Light-Bridge Structure and Dynamics. *Astrophys. J. Lett.* **589**, L117. DOI. ADS.

Berlicki, A., Heinzel, P., Schmieder, B., Li, H.: 2008, NLTE modelling of the flaring atmosphere above sunspot. *Astron. Astrophys.* **490**, 315. DOI. ADS.

Bjørgen, J.P., Leenaarts, J., Rempel, M., Cheung, M.C.M., Danilovic, S., de la Cruz Rodríguez, J., Sukhorukov, A.V.: 2019, Three-dimensional modeling of chromospheric spectral lines in a simulated active region. *A&A* **631**, A33. DOI. ADS.

Borrero, J.M., Asensio Ramos, A., Collados, M., Schlichenmaier, R., Balthasar, H., Franz, M., Rezaei, R., Kiess, C., Orozco Suárez, D., Pastor Yabar, A., Berkefeld, T., von der Lühe, O., Schmidt, D., Schmidt, W., Sigwarth, M., Soltau, D., Volkmer, R., Waldmann, T., Denker, C., Hofmann, A., Staude, J., Strassmeier, K.G., Feller, A., Lagg, A., Solanki, S.K., Sobotka, M., Nicklas, H.: 2016, Deep probing of the photospheric sunspot penumbra: no evidence of field-free gaps. *Astron. Astrophys.* **596**, A2. DOI. ADS.

Bose, S., Henriques, V.M.J., Rouppe van der Voort, L., Pereira, T.M.D.: 2019, Semi-empirical model atmospheres for the chromosphere of the sunspot penumbra and umbral flashes. *A&A* **627**, A46. DOI. ADS.

Buehler, D., Lagg, A., Solanki, S.K., van Noort, M.: 2015, Properties of solar plage from a spatially coupled inversion of Hinode SP data. *A&A* **576**, A27. DOI. ADS.

Buehler, D., Lagg, A., van Noort, M., Solanki, S.K.: 2019, A comparison between solar plage and network properties. *A&A* **630**, A86. DOI. ADS.

Carlsson, M., Stein, R.F.: 1992, Non-LTE Radiating Acoustic Shocks and CA II K2V Bright Points. *Astrophys. J. Lett.* **397**, L59. DOI. ADS.

Carlsson, M., Stein, R.F.: 1997, Formation of Solar Calcium H and K Bright Grains. *Astrophys. J.* **481**, 500. DOI. ADS.

Carlsson, M., Stein, R.F.: 2002, Dynamic Hydrogen Ionization. *ApJ* **572**, 626. DOI. ADS.

Carlsson, M., De Pontieu, B., Hansteen, V.H.: 2019, New View of the Solar Chromosphere. *Annurev.aa.* **57**, 189. DOI. ADS.

Casini, R., Landi Degl'Innocenti, E.: 1994, Properties of the first-order moments of the polarization profiles of hydrogen lines. *Astron. Astrophys.* **291**, 668. ADS.

Centeno, R.: 2018, On the Weak Field Approximation for Ca 8542 Å. *Astrophys. J.* **866**, 89. DOI. ADS.

Charbonneau, P.: 2020, Dynamo models of the solar cycle. *Living Reviews in Solar Physics* **17**, 4. DOI. ADS.

Cheung, M.C.M., Rempel, M., Chintzoglou, G., Chen, F., Testa, P., Martínez-Sykora, J., Sainz Dalda, A., DeRosa, M.L., Malanushenko, A., Hansteen, V., De Pontieu, B., Carlsson, M., Gudiksen, B., McIntosh, S.W.: 2019, A comprehensive three-dimensional radiative magnetohydrodynamic simulation of a solar flare. *Nature Astronomy* **3**, 160. DOI. ADS.

Cirtain, J.W., Golub, L., Winebarger, A.R., de Pontieu, B., Kobayashi, K., Moore, R.L., Walsh, R.W., Korreck, K.E., Weber, M., McCauley, P., Title, A., Kuzin, S., Deforest, C.E.: 2013, Energy release in the solar corona from spatially resolved magnetic braids. *Nature* **493**, 501. DOI. ADS.

Collados, M., Lagg, A., Díaz Garcí A, J.J., Hernández Suárez, E., López López, R., Páez Mañá, E., Solanki, S.K.: 2007, Tenerife Infrared Polarimeter II. In: Heinzel, P., Dorotovič, I., Rutten, R.J. (eds.) *The Physics of Chromospheric Plasmas*, *Astronomical Society of the Pacific Conference Series* **368**, 611. ADS.

Collados, M., Bettonvil, F., Cavaller, L., Ermolli, I., Gelly, B., Pérez, A., Socas-Navarro, H., Soltau, D., Volkmer, R., EST Team: 2013, The European Solar Telescope. *Mem. Soc. Astron. Italiana* **84**, 379. ADS.

Cranmer, S.R., Winebarger, A.R.: 2019, The Properties of the Solar Corona and Its Connection to the Solar Wind. *Annurev.aa.* **57**, 157. DOI. ADS.

Criscuoli, S., Del Moro, D., Giannattasio, F., Viticchié, B., Giorgi, F., Ermolli, I., Zuccarello, F., Berrilli, F.: 2012, High cadence spectropolarimetry of moving magnetic features observed around a pore. *A&A* **546**, A26. DOI. ADS.

de la Cruz Rodríguez, J.: 2019, A method for global inversion of multi-resolution solar data. *Astron. Astrophys.* **631**, A153. DOI. ADS.

de la Cruz Rodríguez, J., Piskunov, N.: 2013, DELO-Bezier Formal Solutions of the Polarized Radiative Transfer Equation. *Astrophys. J.* **764**, 33. DOI. ADS.

de la Cruz Rodríguez, J., Leenaarts, J., Asensio Ramos, A.: 2016, Non-LTE Inversions of the Mg II h & k and UV Triplet Lines. *ApJL* **830**, L30. DOI. ADS.

de la Cruz Rodríguez, J., Rouppe van der Voort, L., Socas-Navarro, H., van Noort, M.: 2013, Physical properties of a sunspot chromosphere with umbral flashes. *Astron. Astrophys.* **556**, A115. DOI. ADS.

de la Cruz Rodríguez, J., Leenaarts, J., Danilovic, S., Uitenbroek, H.: 2019, STiC: A multiatom non-LTE PRD inversion code for full-Stokes solar observations. *A&A* **623**, A74. DOI. ADS.

De Pontieu, B., Polito, V., Hansteen, V., Testa, P., Reeves, K.K., Antolin, P., Nóbrega-Siverio, D.E., Kowalski, A.F., Martinez-Sykora, J., Carlsson, M., McIntosh, S.W., Liu, W., Daw, A., Kankelborg, C.C.: 2021, A New View of the Solar Interface Region from the Interface Region Imaging Spectrograph (IRIS). *Solar Phys.* **296**, 84. DOI. ADS.

del Toro Iniesta, J.C.: 2007, *Introduction to Spectropolarimetry.* ADS.

del Toro Iniesta, J.C., Collados, M.: 2000, Optimum Modulation and Demodulation Matrices for Solar Polarimetry. *Applied Optics* **39**, 1637. DOI. ADS.

del Toro Iniesta, J.C., Ruiz Cobo, B.: 2016, Inversion of the radiative transfer equation for polarized light. *Living Reviews in Solar Physics* **13**, 4. DOI. ADS.

Denis, S., Coucke, P., Gabriel, E., Delrez, C., Venkatakrishnan, P.: 2008, Optomechanical and thermal design of the Multi-Application Solar Telescope for USO. In: Stepp, L.M., Gilmozzi, R. (eds.) *Ground-based and Airborne Telescopes II* **7012**, SPIE, 1194 . International Society for Optics and Photonics. DOI. URL.

Díaz Baso, C.J., Asensio Ramos, A., de la Cruz Rodríguez, J.: 2022, Bayesian Stokes inversion with normalizing flows. *Astron. Astrophys.* **659**, A165. DOI. ADS.

Díaz Baso, C.J., de la Cruz Rodríguez, J., Leenaarts, J.: 2021, An observationally constrained model of strong magnetic reconnection in the solar chromosphere. Atmospheric stratification and estimates of heating rates. *Astron. Astrophys.* **647**, A188. DOI. ADS.

Dunn, R.B.: 1969, Sacramento Peak's New Solar Telescope. *S&T* **38**, 368. ADS.

Falchi, A., Mauas, P.J.D.: 2002, Chromospheric models of a solar flare including velocity fields. *Astron. Astrophys.* **387**, 678. DOI. ADS.

Felipe, T., González Manrique, S.J., Sangeetha, C.R., Asensio Ramos, A.: 2023, Magnetic field fluctuations in the shocked umbral chromosphere. *Astron. Astrophys.* **676**, A77. DOI. ADS.

Ferrente, F., Zuccarello, F., Guglielmino, S.L., Criscuoli, S., Romano, P.: 2023, Photospheric and Chromospheric Magnetic Field Evolution during the X1.6 Flare in Active Region NOAA 12192. *Astrophys. J.* **954**, 185. DOI. ADS.

Fontenla, J.M., Avrett, E.H., Loeser, R.: 1993, Energy Balance in the Solar Transition Region. III. Helium Emission in Hydrostatic, Constant-Abundance Models with Diffusion. *Astrophys. J.* **406**, 319. DOI. ADS.

French, R.J., Bogdan, T.J., Casini, R., de Wijn, A.G., Judge, P.G.: 2023, First Observation of Chromospheric Waves in a Sunspot by DKIST/ViSP: The Anatomy of an Umbral Flash. *ApJL* **945**, L27. DOI. ADS.

Gabriel, A.H.: 1976, A Magnetic Model of the Solar Transition Region. *Philosophical Transactions of the Royal Society of London Series A* **281**, 339. DOI. ADS.

Hanaoka, Y.: 2005, Hα Stokes V/I Features Observed in a Solar Active Region. *PASJ* **57**, 235. DOI. ADS.

Hanle, W.: 1923, Über den Zeemaneffekt bei der Resonanzfluoreszenz. *Naturwissenschaften* **11**, 690. DOI. ADS.

Hansteen, V., Guerreiro, N., De Pontieu, B., Carlsson, M.: 2015, Numerical Simulations of Coronal Heating through Footpoint Braiding. *Astrophys. J.* **811**, 106. DOI. ADS.

Hasan, S.S.: 2010, The Indian National Large Solar Telescope (NLST). In: Kosovichev, A.G., Andrei, A.H., Rozelot, J.-P. (eds.) *Solar and Stellar Variability: Impact on Earth and Planets* **264**, 499. DOI. ADS.

Houston, S.J., Jess, D.B., Asensio Ramos, A., Grant, S.D.T., Beck, C., Norton, A.A., Krishna Prasad, S.: 2018, The Magnetic Response of the Solar Atmosphere to Umbral Flashes. *ApJ* **860**, 28. DOI. ADS.

Jaeggli, S.A., Schad, T.A., Tarr, L.A., Harrington, D.M.: 2022, A Model-based Technique for Ad Hoc Correction of Instrumental Polarization in Solar Spectropolarimetry. *Astrophys. J.* **930**, 132. DOI. ADS.

Jaume Bestard, J., Trujillo Bueno, J., Bianda, M., Štěpán, J., Ramelli, R.: 2022, Spectropolarimetric observations of the solar atmosphere in the Hα 6563 Å line. *A&A* **659**, A179. DOI. ADS.

Jones, H.P., Giovanelli, R.G.: 1982, Magnetograph Response to Canopy-Type Fields. *Solar Phys.* **79**, 247. DOI. ADS.

Joshi, J., de la Cruz Rodríguez, J.: 2018, Magnetic field variations associated with umbral flashes and penumbral waves. *A&A* **619**, A63. DOI. ADS.

Joshi, J., Lagg, A., Solanki, S.K., Feller, A., Collados, M., Orozco Suárez, D., Schlichenmaier, R., Franz, M., Balthasar, H., Denker, C., Berkefeld, T., Hofmann, A., Kiess, C., Nicklas, H., Pastor Yabar, A., Rezaei, R., Schmidt, D., Schmidt, W., Sobotka, M., Soltau, D., Staude, J., Strassmeier, K.G., Volkmer, R., von der Lühe, O., Waldmann, T.: 2016, Upper chromospheric magnetic field of a sunspot penumbra: observations of fine structure. *Astron. Astrophys.* **596**, A8. DOI. ADS.

Joshi, J., Lagg, A., Hirzberger, J., Solanki, S.K.: 2017, Three-dimensional magnetic structure of a sunspot: Comparison of the photosphere and upper chromosphere. *A&A* **604**, A98. DOI. ADS.

Judge, P.G., Elmore, D.F., Lites, B.W., Keller, C.U., Rimmele, T.: 2004, Evaluation of Seeing-Induced Cross Talk in Tip-Tilt-Corrected Solar Polarimetry. *Applied Optics* **43**, 3817. DOI. ADS.

Jurčák, J., Martínez Pillet, V., Sobotka, M.: 2006, The magnetic canopy above light bridges. *Astron. Astrophys.* **453**, 1079. DOI. ADS.

Jurčák, J., Bello González, N., Schlichenmaier, R., Rezaei, R.: 2015, A distinct magnetic property of the inner penumbral boundary. Formation of a stable umbra-penumbra boundary in a sunspot. *A&A* **580**, L1. DOI. ADS.

Kawabata, Y., Quintero Noda, C., Katsukawa, Y., Kubo, M., Matsumoto, T., Oba, T.: 2024, Multiline Stokes Synthesis of Ellerman Bombs: Obtaining Seamless Information from Photosphere to Chromosphere. *Astrophys. J.* **960**, 26. DOI. ADS.

Keppens, R., Martinez Pillet, V.: 1996, The magnetic structure of pores and sunspots derived from Advanced Stokes Polarimeter data. *A&A* **316**, 229. ADS.

Kerr, G.S., Fletcher, L., Russell, A.J.B., Allred, J.C.: 2016, Simulations of the Mg II k and Ca II 8542 lines from an AlfvÉn Wave-heated Flare Chromosphere. *Astrophys. J.* **827**, 101. DOI. ADS.

Kerr, G.S., Carlsson, M., Allred, J.C., Young, P.R., Daw, A.N.: 2019, SI IV Resonance Line Emission during Solar Flares: Non-LTE, Nonequilibrium, Radiation Transfer Simulations. *Astrophys. J.* **871**, 23. DOI. ADS.

Kleint, L.: 2017, First Detection of Chromospheric Magnetic Field Changes during an X1-Flare. *ApJ* **834**, 26. DOI. ADS.

Kleint, Lucia, Berkefeld, Thomas, Esteves, Miguel, Sonner, Thomas, Volkmer, Reiner, Gerber, Karin, Krämer, Felix, Grassin, Olivier, Berdyugina, Svetlana: 2020, GREGOR: Optics redesign and updates from 2018-2020. *A&A* **641**, A27. DOI. URL.

Krishnappa, N., Feller, A.: 2012, Precision in ground-based solar polarimetry: simulating the role of adaptive optics. *Applied Optics* **51**, 7953. DOI. ADS.

Kuridze, D., Henriques, V.M.J., Mathioudakis, M., Rouppe van der Voort, L., de la Cruz Rodríguez, J., Carlsson, M.: 2018, Spectropolarimetric Inversions of the Ca II 8542 Å Line in an M-class Solar Flare. *ApJ* **860**, 10. DOI. ADS.

Kurucz, R.L.: 2011, Including all the lines. *Canadian Journal of Physics* **89**, 417. DOI. ADS.

Lagg, A., Solanki, S.K., van Noort, M., Danilovic, S.: 2014, Vigorous convection in a sunspot granular light bridge. *Astron. Astrophys.* **568**, A60. DOI. ADS.

Lagg, A., Lites, B., Harvey, J., Gosain, S., Centeno, R.: 2017, Measurements of Photospheric and Chromospheric Magnetic Fields. *SSRv* **210**, 37. DOI. ADS.

Landi Degl'Innocenti, E., Landolfi, M.: 2004, *Polarization in Spectral Lines* **307**. DOI. ADS.

Leenaarts, J., Carlsson, M., Rouppe van der Voort, L.: 2012, The Formation of the Hα Line in the Solar Chromosphere. *ApJ* **749**, 136. DOI. ADS.

Leenaarts, J., Pereira, T., Uitenbroek, H.: 2012, Fast approximation of angle-dependent partial redistribution in moving atmospheres. *Astron. Astrophys.* **543**, A109. DOI. ADS.

Leenaarts, J., Golding, T., Carlsson, M., Libbrecht, T., Joshi, J.: 2016, The cause of spatial structure in solar He I 1083 nm multiplet images. *A&A* **594**, A104. DOI. ADS.

Libbrecht, T., de la Cruz Rodríguez, J., Danilovic, S., Leenaarts, J., Pazira, H.: 2019, Chromospheric condensations and magnetic field in a C3.6-class flare studied via He I D_3 spectropolarimetry. *A&A* **621**, A35. DOI. ADS.

Lites, B.W.: 1987, Rotating waveplates as polarization modulators for Stokes polarimetry of the sun: evaluation of seeing-induced crosstalk errors. *Applied Optics* **26**, 3838. DOI. ADS.

López Ariste, A., Casini, R., Paletou, F., Tomczyk, S., Lites, B.W., Semel, M., Landi Degl'Innocenti, E., Trujillo Bueno, J., Balasubramaniam, K.S.: 2005, Full Stokes Spectropolarimetry of Hα in Prominences. *ApJL* **621**, L145. DOI. ADS.

Martínez González, M.J., Bellot Rubio, L.R.: 2009, Emergence of Small-scale Magnetic Loops Through the Quiet Solar Atmosphere. *Astrophys. J.* **700**, 1391. DOI. ADS.

Martínez González, M.J., del Pino Alemán, T., Yabar, A.P., Noda, C.Q., Ramos, A.A.: 2023, On the Magnetic Nature of Quiet-Sun Chromospheric Grains. *Astrophys. J. Lett.* **955**, L40. DOI. ADS.

Mathur, H., Thulasidharen, K.C., Pruthvi, H., Nagaraju, K., Rajalingam, M.: 2022a, An Image Auto Guider System for Kodaikanal Tower Tunnel Telescope. *Journal of Astronomical Instrumentation* **11**, 2350003. DOI. ADS.

Mathur, H., Joshi, J., Nagaraju, K., van der Voort, L.R., Bose, S.: 2022b, Properties of shock waves in the quiet-Sun chromosphere. *Astron. Astrophys.* **668**, A153. DOI. ADS.

Mathur, H., Nagaraju, K., Joshi, J., de la Cruz Rodríguez, J.: 2023, Do Hα Stokes V Profiles Probe the Chromospheric Magnetic Field? An Observational Perspective. *ApJ* **946**, 38. DOI. ADS.

Mathur, H., Nagaraju, K., Pruthvi, H., Sagaynathan, K.: 2024a, Measurements of seeing-induced crosstalk in tip–tilt corrected solar polarimetry. *Appl. Opt.* **63**, 4088. DOI. URL.

Mathur, H., Nagaraju, K., Yadav, R., Joshi, J.: 2024b, Simultaneous spectropolarimetric observations in the Hα and Ca II 8662 Å lines of an active region.

Milkey, R.W., Mihalas, D.: 1974, Resonance line transfer with partial redistribution: II. The solar Mg II lines. *Astrophys. J.* **192**, 769. DOI. ADS.

Mitalas, R., Sills, K.R.: 1992, On the Photon Diffusion Time Scale for the Sun. *Astrophys. J.* **401**, 759. DOI. ADS.

Morosin, R., de la Cruz Rodríguez, J., Vissers, G.J.M., Yadav, R.: 2020, Stratification of canopy magnetic fields in a plage region. Constraints from a spatially-regularized weak-field approximation method. *Astron. Astrophys.* **642**, A210. DOI. ADS.

Morosin, R., de la Cruz Rodríguez, J., Díaz Baso, C.J., Leenaarts, J.: 2022, Spatio-temporal analysis of chromospheric heating in a plage region. *Astron. Astrophys.* **664**, A8. DOI. ADS.

Murabito, M., Romano, P., Guglielmino, S.L., Zuccarello, F., Solanki, S.K.: 2016, Formation of the Penumbra and Start of the Evershed Flow. *ApJ* **825**, 75. DOI. ADS.

Murabito, M., Ermolli, I., Giorgi, F., Stangalini, M., Guglielmino, S.L., Jafarzadeh, S., Socas-Navarro, H., Romano, P., Zuccarello, F.: 2019, Height Dependence of the Penumbral Fine-scale Structure in the Inner Solar Atmosphere. *ApJ* **873**, 126. DOI. ADS.

Nagaraju, K., Sankarasubramanian, K., Rangarajan, K.E.: 2008, On the Weakening of the Chromospheric Magnetic Field in Active Regions. *ApJ* **678**, 531. DOI. ADS.

Nagaraju, K., Sankarasubramanian, K., Rangarajan, K.E.: 2020a, Diagnosing chromospheric magnetic field through simultaneous spectropolarimetry in Hα and Ca II 854.2 nm. In: Kosovichev, A., Strassmeier, S., Jardine, M. (eds.) *Solar and Stellar Magnetic Fields: Origins and Manifestations* **354**, 46. DOI. ADS.

Nagaraju, K., Sankarasubramanian, K., Rangarajan, K.E.: 2020b, Hα full line spectropolarimetry as diagnostics of chromospheric magnetic field. *Journal of Astrophysics and Astronomy* **41**, 10. DOI. ADS.

Nagaraju, K., Feller, A., Ihle, S., Soltau, H.: 2011, Atmospheric turbulence and high-precision ground-based solar polarimetry. In: Fineschi, S., Fennelly, J. (eds.) *Solar Physics and Space Weather Instrumentation IV*, *Society of Photo-Optical Instrumentation Engineers (SPIE) Conference Series* **8148**, 81480S. DOI. ADS.

Narayan, G., Scharmer, G.B.: 2010, Small-scale convection signatures associated with a strong plage solar magnetic field. *A&A* **524**, A3. DOI. ADS.

Nóbrega-Siverio, D., Guglielmino, S.L., Sainz Dalda, A.: 2021, Solar surges related to UV bursts. Characterization through k-means, inversions, and density diagnostics. *Astron. Astrophys.* **655**, A28. DOI. ADS.

Paletou, F., Lafon, M., Maeght, P., Grimaud, F., Louge, T., Aboudarham, J.: 2009, The Ground-Based Solar Observations Database BASS 2000. In: Berdyugina, S.V., Nagendra, K.N., Ramelli, R. (eds.) *Solar Polarization 5: In Honor of Jan Stenflo*, *Astronomical Society of the Pacific Conference Series* **405**, 397. ADS.

Parker, E.N.: 1972, Topological Dissipation and the Small-Scale Fields in Turbulent Gases. *Astrophys. J.* **174**, 499. DOI. ADS.

Parker, E.N.: 1988, Nanoflares and the Solar X-Ray Corona. *Astrophys. J.* **330**, 474. DOI. ADS.

Parnell, C.E., De Moortel, I.: 2012, A contemporary view of coronal heating. *Philosophical Transactions of the Royal Society of London Series A* **370**, 3217. DOI. ADS.

Pietarila, A., Socas-Navarro, H., Bogdan, T.: 2007a, Spectropolarimetric Inversions of the Ca II 8498 and 8542 Å Lines in the Quiet Sun. *Astrophys. J.* **670**, 885. DOI. ADS.

Pietarila, A., Socas-Navarro, H., Bogdan, T.: 2007b, The Ca II Infrared Triplet Lines as Diagnostics of Chromospheric Magnetism. In: Heinzel, P., Dorotovič, I., Rutten, R.J. (eds.) *The Physics of Chromospheric Plasmas*, *Astronomical Society of the Pacific Conference Series* **368**, 139. ADS.

Piskunov, N., Valenti, J.A.: 2017, Spectroscopy Made Easy: Evolution. *Astron. Astrophys.* **597**, A16. DOI. ADS.

Prasad, A., Ranganathan, M., Beck, C., Choudhary, D.P., Hu, Q.: 2022, The magnetic topology of the inverse Evershed flow. *A&A* **662**, A25. DOI. ADS.

Priest, E.: 2014, *Magnetohydrodynamics of the Sun*. DOI. ADS.

Priest, E.R., Heyvaerts, J.F., Title, A.M.: 2002, A Flux-Tube Tectonics Model for Solar Coronal Heating Driven by the Magnetic Carpet. *Astrophys. J.* **576**, 533. DOI. ADS.

Pruthvi, H.: 2019, Design and development of chromospheric vector magnetograph for sunspot studies. *IIA Ph.D. Thesis.* DOI.

Pruthvi, H., Krishnappa, N., Belur, R., Kadagattor, R.B.: 2018, Solar spectropolarimetry of Ca II 8542 Å line: polarimeter development, calibration, and preliminary observations. *Journal of Astronomical Telescopes, Instruments, and Systems* **4**, 4.8002. DOI. ADS.

Quintero Noda, C., Shimizu, T., Ruiz Cobo, B., Suematsu, Y., Katsukawa, Y., Ichimoto, K.: 2016a, Analysis of a spatially deconvolved solar pore. *MNRAS* **460**, 1476. DOI. ADS.

Quintero Noda, C., Shimizu, T., de la Cruz Rodríguez, J., Katsukawa, Y., Ichimoto, K., Anan, T., Suematsu, Y.: 2016b, Spectropolarimetric capabilities of Ca II 8542 Å line. *Mon. Not. Roy. Astron. Soc.* **459**, 3363. DOI. ADS.

Rachkovsky, D.N.: 1967, The reduction for anomalous dispersion in the theory of absorption line formation in a magnetic field. *Izvestiya Ordena Trudovogo Krasnogo Znameni Krymskoj Astrofizicheskoj Observatorii* **37**, 56. ADS.

Reale, F.: 2014, Coronal Loops: Observations and Modeling of Confined Plasma. *Living Reviews in Solar Physics* **11**, 4. DOI. ADS.

Rimmele, T.R.: 1997, Evidence for Magnetoconvection in a Sunspot Light Bridge. *Astrophys. J.* **490**, 458. DOI. ADS.

Rimmele, T.R.: 2000, Solar adaptive optics. In: Wizinowich, P.L. (ed.) *Adaptive Optical Systems Technology*, *Society of Photo-Optical Instrumentation Engineers (SPIE) Conference Series* **4007**, 218. DOI. ADS.

Rimmele, T.: 2008, On the Relation between Umbral Dots, Dark-cored Filaments, and Light Bridges. *Astrophys. J.* **672**, 684. DOI. ADS.

Rimmele, T.R., Marino, J.: 2011, Solar Adaptive Optics. *Living Reviews in Solar Physics* **8**, 2. DOI. ADS.

Rimmele, T.R., Warner, M., Keil, S.L., Goode, P.R., Knölker, M., Kuhn, J.R., Rosner, R.R., McMullin, J.P., Casini, R., Lin, H., Wöger, F., von der Lühe, O., Tritschler, A., Davey, A., de Wijn, A., Elmore, D.F., Fehlmann, A., Harrington, D.M., Jaeggli, S.A., Rast, M.P., Schad, T.A., Schmidt, W., Mathioudakis, M., Mickey, D.L., Anan, T., Beck, C., Marshall, H.K., Jeffers, P.F., Oschmann, J.M., Beard, A., Berst, D.C., Cowan, B.A., Craig, S.C., Cross, E., Cummings, B.K., Donnelly, C., de Vanssay, J.-B., Eigenbrot, A.D., Ferayorni, A., Foster, C., Galapon, C.A., Gedrites, C., Gonzales, K., Goodrich, B.D., Gregory, B.S., Guzman, S.S., Guzzo, S., Hegwer, S., Hubbard, R.P., Hubbard, J.R., Johansson, E.M., Johnson, L.C., Liang, C., Liang, M., McQuillen, I., Mayer, C., Newman, K., Onodera, B., Phelps, L., Puentes, M.M., Richards, C., Rimmele, L.M., Sekulic, P., Shimko, S.R., Simison, B.E., Smith, B., Starman, E., Sueoka, S.R., Summers, R.T., Szabo, A., Szabo, L., Wampler, S.B., Williams, T.R., White, C.: 2020, The Daniel K. Inouye Solar Telescope - Observatory Overview. *SoPh* **295**, 172. DOI. ADS.

Rueedi, I., Solanki, S.K., Livingston, W.: 1995, Infrared lines as probes of solar magnetic features. XI. Structure of a sunspot umbra with a light bridge. *Astron. Astrophys.* **302**, 543. ADS.

Ruiz Cobo, B., Quintero Noda, C., Gafeira, R., Uitenbroek, H., Orozco Suárez, D., Páez Mañá, E.: 2022, DeSIRe: Departure coefficient aided Stokes Inversion based on Response functions. *A&A* **660**, A37. DOI. ADS.

Rutten, R.J.: 2003, *Radiative Transfer in Stellar Atmospheres.* ADS.

Ryabchikova, T., Piskunov, N., Kurucz, R.L., Stempels, H.C., Heiter, U., Pakhomov, Y., Barklem, P.S.: 2015, A major upgrade of the VALD database. *PhyS* **90**, 054005. DOI. ADS.

Sanchez Almeida, J.: 1997, Chromospheric polarity reversals on sunspots. Are they consistent with weak line emission? *Astron. Astrophys.* **324**, 763. ADS.

Sankarasubramanian, K., Rimmele, T.: 2002, Bisector Analysis of Stokes Profiles: Effects Due to Gradients in the Physical Parameters. *Astrophys. J.* **576**, 1048. DOI. ADS.

Sankarasubramanian, R., Rangarajan, K.E., Ramesh, K.B.: 2002, Measurement of solar vector magnetic fields using Kodaikanal tower telescope. *Bulletin of the Astronomical Society of India* **30**, 473. ADS.

Schad, T.A., Penn, M.J., Lin, H., Tritschler, A.: 2015, He I Vector Magnetic Field Maps of a Sunspot and Its Superpenumbral Fine-Structure. *Solar Phys.* **290**, 1607. DOI. ADS.

Scharmer, G.B., Bjelksjo, K., Korhonen, T.K., Lindberg, B., Petterson, B.: 2003, The 1-m Swedish solar telescope. In: Keil, S.L., Avakyan, S.V. (eds.) *Innovative Telescopes and Instrumentation for Solar Astrophysics* **4853**, SPIE, 341 . International Society for Optics and Photonics. DOI. URL.

Shimizu, T., Ichimoto, K., Suematsu, Y.: 2012, Precursor of Sunspot Penumbral Formation Discovered with Hinode Solar Optical Telescope Observations. *ApJL* **747**, L18. DOI. ADS.

Sivaraman, K.R., Gupta, S.S., Kariyappa, R.: 1993, What is a quiet sun CaII K line profile? *Bulletin of the Astronomical Society of India* **21**, 659. ADS.

Sivaraman, K.R., Gupta, S.S., Kariyappa, R.: 1996, CA II K Line Profile of the Truly Quiet Sun. *Solar Physics* **163**, 93. DOI. ADS.

Sivaraman, K.R., Gupta, S.S., Kariyappa, R., Aleem, P.S.M., Sundararaman, K.: 1993, Solar variability in the Ca II K line during solar cycles 21 and 22. *Bulletin of the Astronomical Society of India* **21**, 655. ADS.

Sobotka, M., Švanda, M., Jurčák, J., Heinzel, P., Del Moro, D., Berrilli, F.: 2013, Dynamics of the solar atmosphere above a pore with a light bridge. *A&A* **560**, A84. DOI. ADS.

Socas-Navarro, H.: 2007, Semiempirical Models of Solar Magnetic Structures. *Astrophys. J.S* **169**, 439. DOI. ADS.

Socas-Navarro, H., Uitenbroek, H.: 2004, On the Diagnostic Potential of Hα for Chromospheric Magnetism. *ApJL* **603**, L129. DOI. ADS.

Socas-Navarro, H., Trujillo Bueno, J., Ruiz Cobo, B.: 2000a, Anomalous Circular Polarization Profiles in Sunspot Chromospheres. *Astrophys. J.* **544**, 1141. DOI. ADS.

Socas-Navarro, H., Trujillo Bueno, J., Ruiz Cobo, B.: 2000b, Non-LTE Inversion of Stokes Profiles Induced by the Zeeman Effect. *ApJ* **530**, 977. DOI. ADS.

Socas-Navarro, H., Elmore, D., Pietarila, A., Darnell, A., Lites, B.W., Tomczyk, S., Hegwer, S.: 2006, Spinor: Visible and Infrared Spectro-Polarimetry at the National Solar Observatory. *SoPh* **235**, 55. DOI. ADS.

Solanki, S.K., Steiner, O.: 1990, How magnetic is the solar chromosphere? *Astron. Astrophys.* **234**, 519. ADS.

Solanki, S.K., Steiner, O., Uitenbroeck, H.: 1991, Two-dimensional models of the solar chromosphere. I - The CA II K line as a diagnostic: 1.5-D radiative transfer. *Astron. Astrophys.* **250**, 220. ADS.

Sowmya, K., Lagg, A., Solanki, S.K., Castellanos Durán, J.S.: 2022, Magnetized supersonic downflows in the chromosphere. *arXiv e-prints*, arXiv:2202.11679. ADS.

Stauffer, J.R., Reardon, K.P., Penn, M.: 2022, Chromospheric Carbon Monoxide Formation around a Solar Pore. *ApJ* **930**, 87. DOI. ADS.

Stenflo, J.O.: 1982, The Hanle Effect and the Diagnostics of Turbulent Magnetic Fields in the Solar Atmosphere. *Solar Phys.* **80**, 209. DOI. ADS.

Sterling, A.C.: 2000, Solar Spicules: A Review of Recent Models and Targets for Future Observations - (Invited Review). *Solar Phys.* **196**, 79. DOI. ADS.

Sundara Raman, K., Aleem, P.S.M., Thiagarajan, R.: 1999, Evershed velocities in bipolar sunspots. *Bulletin of the Astronomical Society of India* **27**, 383. ADS.

Tapia, A.S., Bellot Rubio, L.R.: 2022, The magnetic canopy of pores and quiet Sun features as observed through the Mg I b2 line. In: *44th COSPAR Scientific Assembly. Held 16-24 July* **44**, 2512. ADS.

Trujillo Bueno, J., Landi Degl'Innocenti, E., Collados, M., Merenda, L., Manso Sainz, R.: 2002, Selective absorption processes as the origin of puzzling spectral line polarization from the Sun. *Nature* **415**, 403. DOI. ADS.

Uitenbroek, H.: 1989, Operator perturbation method for multi-level line transfer with partial redistribution. *Astron. Astrophys.* **213**, 360. ADS.

Uitenbroek, H.: 2001, Multilevel Radiative Transfer with Partial Frequency Redistribution. *Astrophys. J.* **557**, 389. DOI. ADS.

Unno, W.: 1956, Line Formation of a Normal Zeeman Triplet. *Pub. Astron. Soc. Japan* **8**, 108. ADS.

Van Doorsselaere, T., Srivastava, A.K., Antolin, P., Magyar, N., Vasheghani Farahani, S., Tian, H., Kolotkov, D., Ofman, L., Guo, M., Arregui, I., De Moortel, I., Pascoe, D.: 2020, Coronal Heating by MHD Waves. *Space Sci. Rev.* **216**, 140. DOI. ADS.

Varsik, J.R., Yang, G.: 2006, Design of a telescope pointing and tracking subsystem for the Big Bear Solar Observatory New Solar Telescope. In: Lewis, H., Bridger, A. (eds.) *Advanced Software and Control for Astronomy* **6274**, SPIE, 542 . International Society for Optics and Photonics. DOI. URL.

Vecchio, A., Cauzzi, G., Reardon, K.P.: 2009, The solar chromosphere at high resolution with IBIS. II. Acoustic shocks in the quiet internetwork and the role of magnetic fields. *Astron. Astrophys.* **494**, 269. DOI. ADS.

Vernazza, J.E., Avrett, E.H., Loeser, R.: 1981, Structure of the solar chromosphere. III. Models of the EUV brightness components of the quiet sun. *Astrophys. J.S* **45**, 635. DOI. ADS.

Vissers, G.J.M., Danilovic, S., de la Cruz Rodríguez, J., Leenaarts, J., Morosin, R., Díaz Baso, C.J., Reid, A., Pomoell, J., Price, D.J., Inoue, S.: 2021, Non-LTE inversions of a confined X2.2 flare. I. The vector magnetic field in the photosphere and chromosphere. *Astron. Astrophys.* **645**, A1. DOI. ADS.

von der Lühe, O.: 1998, High-resolution observations with the German Vacuum Tower Telescope on Tenerife. *New Astronomy Reviews* **42**, 493. DOI. ADS.

Štěpán, J., Trujillo Bueno, J.: 2010, On the sensitivity of the Halpha scattering polarization to chromospheric magnetism. *Mem. Soc. Astron. Italiana* **81**, 810. ADS.

Štěpán, J., Trujillo Bueno, J.: 2011, Scattering Polarization of Hydrogen Lines in Weakly Magnetized Stellar Atmospheres. I. Formulation and Application to Isothermal Models. *Astrophys. J.* **732**, 80. DOI. ADS.

Wedemeyer-Böhm, S., Lagg, A., Nordlund, Å.: 2009, Coupling from the Photosphere to the Chromosphere and the Corona. *Space Sci. Rev.* **144**, 317. DOI. ADS.

Wiegelmann, T., Thalmann, J.K., Solanki, S.K.: 2014, The magnetic field in the solar atmosphere. *Astron. Astrophys. Rev.* **22**, 78. DOI. ADS.

Withbroe, G.L., Noyes, R.W.: 1977, Mass and energy flow in the solar chromosphere and corona. *Annurev.aa.* **15**, 363. DOI. ADS.

Yadav, R., de la Cruz Rodríguez, J., Díaz Baso, C.J., Prasad, A., Libbrecht, T., Robustini, C., Asensio Ramos, A.: 2019, Three-dimensional magnetic field structure of a flux-emerging region in the solar atmosphere. *A&A* **632**, A112. DOI. ADS.

Yadav, R., Díaz Baso, C.J., de la Cruz Rodríguez, J., Calvo, F., Morosin, R.: 2021, Stratification of physical parameters in a C-class solar flare using multiline observations. *A&A* **649**, A106. DOI. ADS.

Ziegler, J.G., Nichols, N.B.: 1993, Optimum Settings for Automatic Controllers. *Journal of Dynamic Systems, Measurement, and Control* **115**, 220. DOI. URL.

Chapter 7
Appendix

A Do Hα Stokes V profiles probe the chromospheric magnetic field? An observational perspective

A.1 Data reduction

The data are reduced with standard procedures of bias and flat fielding. Calibration data with the procedures described in Socas-Navarro et al. (2006) are used to correct for instrumental polarization. No absolute wavelength calibration is done because of the absence of suitable telluric lines. Instead, we average a few spatial pixels in the quiescent region outside the pore (quiet-Sun profile) and fit the quiet-Sun profile over the full Ca II 8542 Å spectral range ($I_{\mathrm{obs}}^{\mathrm{mean}}$) with the BASS 2000 atlas (Paletou et al., 2009).

The procedures of the spectral veil correction, SI intensity calibration, and estimation of spectral Point Spread Function (PSF) for the Ca II 8542 Å and Hα data are described as follows. We followed the spectral veil correction process described in Borrero et al. (2016) with an additional step correcting the tilt in the spectrum continuum. The continuum of the raw data, because of detector flat-field residuals and pre-filter shape, is tilted. These tilts were corrected in the data reduction pipeline by subtracting a linear fit ($y = a + b\lambda$) with the average spectrum. However, the observed spectral range is not symmetric with respect to the core of the Ca II 8542 Å and Hα lines, and there is an inherent tilt present even in the BASS 2000 atlas. Hence we again corrected this over-correction in the tilts by dividing with a normalized linear fit by matching the continuum intensity levels to that of the reference profile (I_{ref}). For the Ca II 8542 Å data, we used spectra synthesized using the RH code (Uitenbroek, 2001) with FAL-C (Avrett, 1985; Fontenla, Avrett, and Loeser, 1993) model atmosphere at $\mu = 0.8$ as I_{ref}. We ensured that there is a good match of synthesized spectra of the Ca II 8542 Å line at $\mu = 1$ with BASS 2000 atlas Spectrum, which gave us confidence in using $\mu = 0.8$ spectra as I_{ref}. After correcting the continua tilt, we estimated the PSF and straylight fraction. PSF is assumed to be Gaussian (σ) for the whole Ca II 8542 Å line spectral range, but straylight fraction (ν) is allowed to vary over the blends of the Si I 8536 Å, the Fe I 8538 Å and about the Ca II 8542 Å line core. To estimate σ and ν, we minimised the χ^2 distance between the $I_{\rm obs}^{\rm mean}$ and $I_{ref}^{degraded}$ with σ and ν.

$$I_{\rm ref}^{\rm degraded}(\lambda) = (1-\nu) I_{\rm ref}(\lambda) * g(\lambda, \sigma) + \nu * I_{\rm ref}^{\rm c}(\lambda) \tag{7.1}$$

where $I_{\rm ref}^{\rm c}$ is the value of intensity at the observed predefined far-wing wavelength point. The absolute SI intensity calibration is done by comparing the intensity of the observed predefined continuum wavelength point with the intensity at degraded $I_{\rm ref}$.

We followed a similar process for estimation of the spectral veil and spectral PSF for the Hα data, but instead of using synthesized spectrum as $I_{\rm ref}$, we inferred $I_{\rm ref}$ using BASS 2000 atlas Hα spectrum (Paletou et al., 2009) and center-to-limb variation calculated from $\mu = 1$ to $\mu = 0.8$ using the RH code with FAL-C model atmosphere. We used a 6-level Hydrogen atom without a fine structure to synthesize the intensity of Hα line with the blend of the Fe I 6569 Å line. The atomic parameters of the Fe I 6569 Å line are retrieved from Kurucz's line lists (Kurucz, 2011) and synthesized in LTE approximation.

A.2 JK Coupling

In J_1-l (JK) coupling scheme, a 'parent' level of orbital angular momentum L_1 and spin S_1 couples its total angular momentum J_1 with the orbital angular momentum l of a further electron, to give an angular momentum K which in turn couples with electron's spin to give total angular momentum J (for more details see page 77 of Landi Degl'Innocenti and Landolfi, 2004).

The Landé factor for level in J_1-l (JK) coupling is

$$g_{J_1-l} = 1 + \gamma(J, 1/2, K) + \gamma(J, K, 1/2)\gamma(K, J_1, l)\gamma(J_1, S_1, L_1) \tag{7.2}$$

where

$$\gamma(A, B, C) = \frac{A(A+1) + B(B+1) - C(C+1)}{2A(A+1)} \tag{7.3}$$

A.3 Quality of fits

In Fig. 7.1 we discuss the match between the observed and synthesized Stokes I and V for the profiles discussed in the paper.

In general, the synthesized Stokes I and V profiles show a good match with the observed profiles. The emission in the blue wing of the Ca II 8542 Å line and reversal in the Stokes V is very well reproduced in the synthesized profiles (see blue-colored

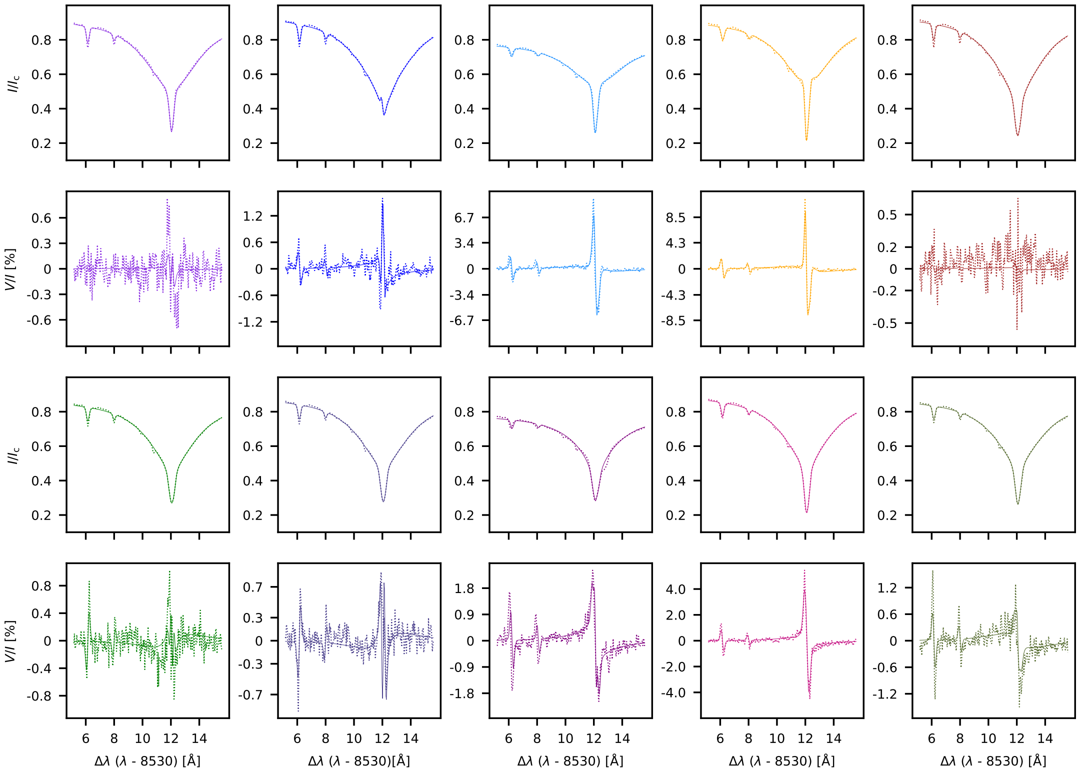

Figure 7.1: Examples of the observed (dotted lines) and synthesized (solid lines) Ca II 8542 Å Stokes I and V profiles for the pixels marked by 'x' in Fig.2.1.

profile). When the Stokes V signal is higher than 1%, a good match is seen in the Si I 8536 Å , Fe I 8538 Å and Ca II 8542 Å Stokes I and V profiles, for example, cyan, maroon, pink and khaki colored profiles. The opposite sign is very well reproduced in the Stokes V signal of the Si I 8536 Å and Fe I 8538 Å lines and reversal in the Ca II 8542 Å line far wing Stokes V signal, for example, green and purple colored profile. When the signal in Stokes V is less than 0.5%, the match of the synthesized Stokes V profile is relatively poor compared to the above cases, for example, purple and brown colored profiles.

B An image autoguider system for the Kodaikanal Tower Tunnel Telescope

B.1 Image Drift Measurements at KTT

We present two sets of drift measurements, using photodiodes and another manual while the first mirror M1 of the Coelostat of the KTT is tracking the Sun at nominal speed (15 degree hour^{-1}). The drift measurements were carried out by marking the limb's position on graph paper using a ruler with 0.5 mm spaced markings every five minutes for fifteen minutes and also with the help of SPOT-2D sensors used in the Auto Guider system in open-loop. The maximum error in manual drift measurements is 0.030 mm minute^{-1} (0.5/15) or 0.180 arcsec minute^{-1} and measurement uncertainty of photodiodes, inferred from reading the voltages without illuminating the sensors, is 14.59 mVolts or 0.296 $''$.

Table 7.1 lists the image drifts measured manually at various times of the day both in East-West (E-W) and North-South (N-S) directions. The image drift measured using photodiodes are presented in Table 7.2 and Fig. 7.2. The maximum drift recorded is 7.15 arcsec minute^{-1} in N-S direction manually and 6.93 arcsec minute^{-1} in E-W direction using photodiodes.

C Measurements of seeing-induced cross-talk in tip-tilt corrected solar polarimetry

C.1 Integration of tip-tilt and autoguider system

A schematic of the tip-tilt instrumental setup is shown in panel (a) of Fig. 4.1. The KTT is installed with C-Blue One sCMOS camera from First Light Imaging, along with a Piezosystem Jena piezo actuator that has been permanently integrated as the tip-tilt system. The software of the autoguider system has been incorporated into the tip-tilt system as a library. However, the SPOT-2D sensors are currently not utilized for a couple of reasons. Firstly, the autoguider's efficiency, in the worst case

Table 7.1: Drift measurements at various times of the day measured manually. We note that the error in drift is 0.180 arcsec minute^{-1}

Time	East-West Drift (arcsec minute^{-1})	North-South Drift(arcsec minute^{-1})
25/11/2016 07:44 AM	1.10	0.36
25/11/2016 08:01 AM	0.92	0.36
25/11/2016 08:17 AM	0.18	0.55
25/11/2016 08:36 AM	1.10	0.00
25/11/2016 08:54 AM	1.10	0.00
25/11/2016 12:19 PM	1.65	4.95
29/11/2016 12:57 PM	2.20	4.76
29/11/2016 01:28 PM	4.40	7.15
29/11/2016 02:54 PM	0.36	4.03

Table 7.2: Drift measurements at various times of the day measured using photodiodes

Time	East-West Drift (arcsec minute^{-1})	North-South Drift(arcsec minute^{-1})
05/02/2021 08:22 AM	0.72 ± 0.018	1.27 ± 0.031
06/02/2021 11:34 AM	1.05 ± 0.025	0.77 ± 0.019
03/02/2021 12:54 PM	6.93 ± 0.170	5.01 ± 0.123
04/02/2021 14:54 PM	0.83 ± 0.020	0.94 ± 0.023

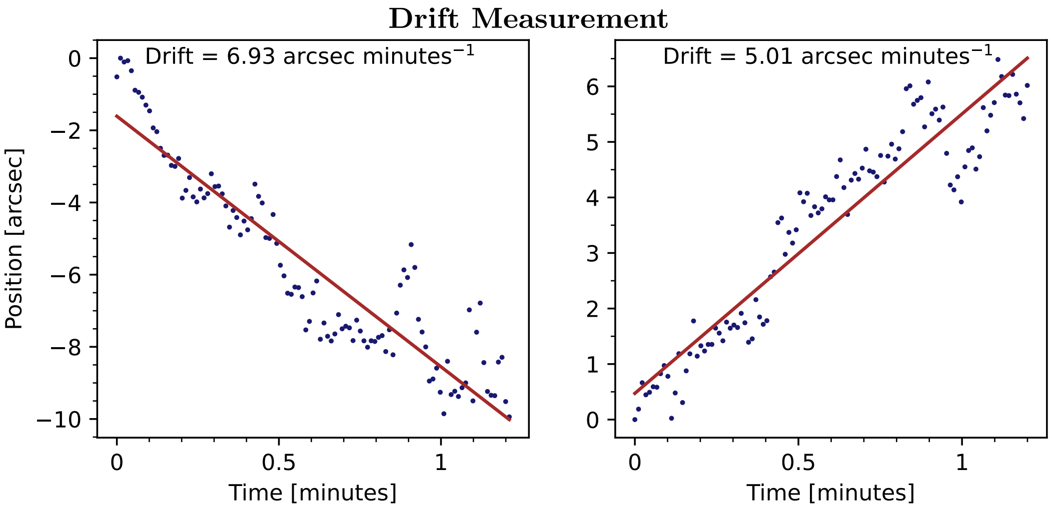

Figure 7.2: Drift Measurement on 03 Feb 2021 12:54 PM in both East-West and North-South direction using photodiodes

scenario, is limited to approximately $\pm 1.9''$, which means that even under favorable seeing conditions ($\sim 1\ ''$), the autoguider introduces image motion of around $1.9\ ''$. Secondly, the SPOT-2D sensors detect the limb, making it challenging for the end user to accurately select the region of interest in the center of the camera frame. This limitation further restricts the extent to which the tip-tilt system can correct for image motion in either direction. Instead, the motors of M2 receive electrical pulses that are calibrated based on the image motion observed by the tip-tilt camera. This calibration is achieved by calibrating electrical pulses given to the motors of M2 against the image motion on the tip-tilt camera, which is, in turn, calibrated against the voltages given to the piezo actuator. The average of the voltages supplied to the piezo is calculated every second. If the difference between this average value and the offset voltage of the piezo actuator exceeds a predefined threshold (typically around 5V), a feedback signal is provided to the motors of M2, triggering appropriate adjustments.

The tip-tilt system's shift computation algorithm is identical to that described in Pruthvi (2019). However, significant changes have been made to the tip-tilt control system. For detailed information on the shift computation method using fast fourier transform (FFT) based cross correlation, please refer to Pruthvi (2019). Here, we will focus on explaining the implementation of the new control system.

Bias and flat-field corrections are performed directly on the camera hardware, so the image received by the tip-tilt control system is ready for use without any additional processing. The C-Blue One camera operates in callback mode, unlike the previous camera, Andor Neo, which operated in polling mode. Consequently, the entire tip-tilt software has been rewritten using an event-driven architecture. This is achieved by using multi-threaded framework, enabling concurrent and parallel execution. The threads dynamically awaken and sleep in response to the events they actively monitor. Figure 7.3 illustrates a schematic representation of the tip-tilt control software.

The following is a description of the control flow for the image stabilization software:

- The main thread initializes various buffers to store images, FFT plans, correlation images, and so on. It also registers a callback method with the camera kernel. Additionally, threads are spawned to handle feedback to actuators and motors, as well as updating the image in the display window.

- Typically, when a new image becomes available, the camera thread invokes the callback function with a clean image that has undergone bias and flat-field correction. The image is then binned to a size of 256×256 (originally 768×768) and the shift, in terms of pixel scale, is computed relative to the reference image. If no reference image is available, the current image becomes the reference, and the thread goes to sleep.

- The computed shifts, in pixels, are then converted to voltages for the actuators

Figure 7.3: The control flow of the tip-tilt system's software is illustrated in the schematic diagram. The software is designed using an event-driven architecture. The primary thread of the program registers a callback function with the camera kernel and initiates the camera thread. It also spawns additional threads responsible for supplying voltages to the actuator, generating electrical pulses for the M2 motor, and updating the displayed image window. Whenever a new image becomes available, the camera thread invokes the registered callback function. This thread is responsible for calculating the necessary feedback for both the actuator and motors. Once the feedback is computed, a signal is transmitted to the actuator and telescope feedback threads, prompting them to awaken and send the feedback to the appropriate hardware interfaces. Additionally, a display counter operates concurrently, and when it reaches its specified interval, it triggers a signal to the display thread. Typically, every 16th frame is transmitted to the display thread, ensuring a smooth display refresh rate of 40 frames per second.

using a proportional derivative control method. A signal is then sent to the actuator thread, which wakes up, applies the voltages to the piezo actuator, and returns to a sleep state.

- Next, the callback function checks if a configurable time interval of 10 seconds has passed since the last update of the reference image. If this condition is met, it verifies if the current image is nearly unshifted ($|\text{Shift}| < 0\overset{\prime\prime}{.}006$ or 0.03 pixels) compared to the current reference. If both conditions are satisfied, the reference image is updated with the current image. This process ensures that only better frames become the reference image and that no significant drift occurs from the first reference image to the last one.
- To ensure the piezo actuator operates within its nominal angles, an average of the voltages applied to the actuator is calculated every second. If the difference between this average and the actuator offset exceeds a threshold (usually 5 V), a signal is sent to the telescope feedback thread. The telescope feedback thread then wakes up, sending electrical pulses to the motors controlling mirror M2, before returning to a sleep state.
- Additionally, a countdown is running (with $n = 16$). When it reaches zero, a signal is sent to the display thread, and the countdown is reset. The camera operates at a nominal frequency of 655 Hz, so every 16th frame corresponds to a smooth display refresh rate of 40 Hz. The display thread wakes up, converts the floating-point image to an 8-bit image suitable for display on a monitor, updates the display window, and then returns to sleep.
- Finally, the camera thread goes to sleep.

D Simultaneous spectropolarimetric observations in the Hα and Ca ii 8662 Å lines of an active region

D.1 Data reduction

The data are reduced with standard procedures of bias and flat-fielding. $I \to V$ cross-talk is removed by the procedure described in Jaeggli et al. (2022). No absolute wavelength calibration is done because of the absence of suitable telluric lines. Instead, we average a few spatial pixels in the quiescent region outside the active region (quiet-Sun profile) and fit the quiet-Sun profile over the full Ca II 8662 Å spectral range with the BASS 2000 atlas (Paletou et al., 2009).

The procedures of the spectral veil correction, SI intensity calibration, and estimation of spectral Point Spread Function (PSF) for the Ca II 8662 Å and Hα data are the same as Mathur et al. (2023), which were inspired by Borrero et al. (2016).

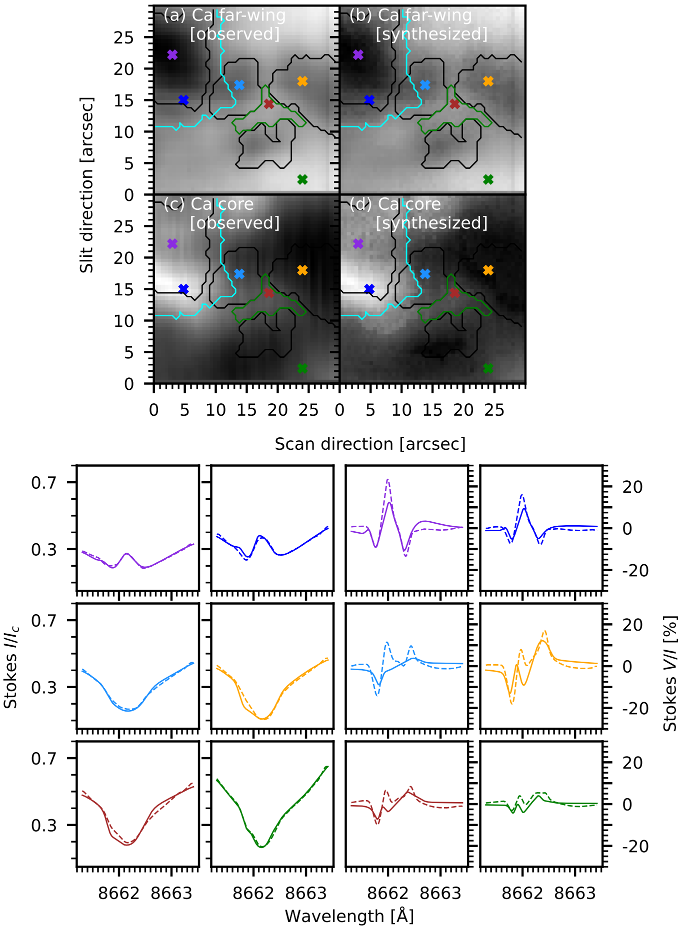

Figure 7.4: The top panel compares the observed and synthesized images of the FOV near the far-wing and line core wavelength positions of the Ca II 8662 Å line. The bottom panel shows the examples of the observed (dotted lines) and synthesized (solid lines) Ca II 8662 Å Stokes I and V profiles for the pixels marked by “×” in Fig. 5.1.

The spectral veil and psf is computed by fitting synthesized profiles using FAL-C (Avrett, 1985; Fontenla, Avrett, and Loeser, 1993) model atmosphere with that of the quiet-Sun profile. The absolute SI intensity calibration is done by comparing the intensity of the observed predefined continuum wavelength point with the intensity value from psf degraded synthetic profile. No spectrum tilt was present in the observed data, thus corrections were not necessary. The full Stokes profiles were filtered using a PCA-based method to improve the signal-to-noise ratio and minimize random fringes in the spectral direction. The spectral fringes were further minimized, and spectral profiles were made smoother using a Python implementation of a relevance vector machine based method*.

D.2 Quality of Fits

Panels (a) and (b) of Fig. 7.4 compare the observed and synthesized narrowband images at the far wing position of the Ca II 8662 Å line, whereas panels (c) and (d) compare the narrowband images at the core of the Ca II 8662 Å line. The comparison between the synthesized and observed Stokes I and V/I profiles of a few selected pixels marked by "×" in panels (a)–(d) are shown in the right panels with the same color. The synthesized narrowband images at the far wing and line core positions of the Ca II 8662 Å line closely resemble those of the observations. The synthesized Stokes I profiles of the marked pixels also match very well with observations. We were able to match the emission feature seen in the purple- and blue-colored profiles as well as a nominal absorption in the remaining profiles. The synthesized Stokes V/I profiles show a good match with the observations in the left-most and the right-most lobes. The amplitude of the central lobe is sometimes lesser than those of the observations. Overall, we deem the fits to be satisfactory for the analysis done in this paper.

---

*https://github.com/aasensio/rvm